Energy and Technology Review

Lawrence Livermore National Laboratory

March 1987

Engineering Technology

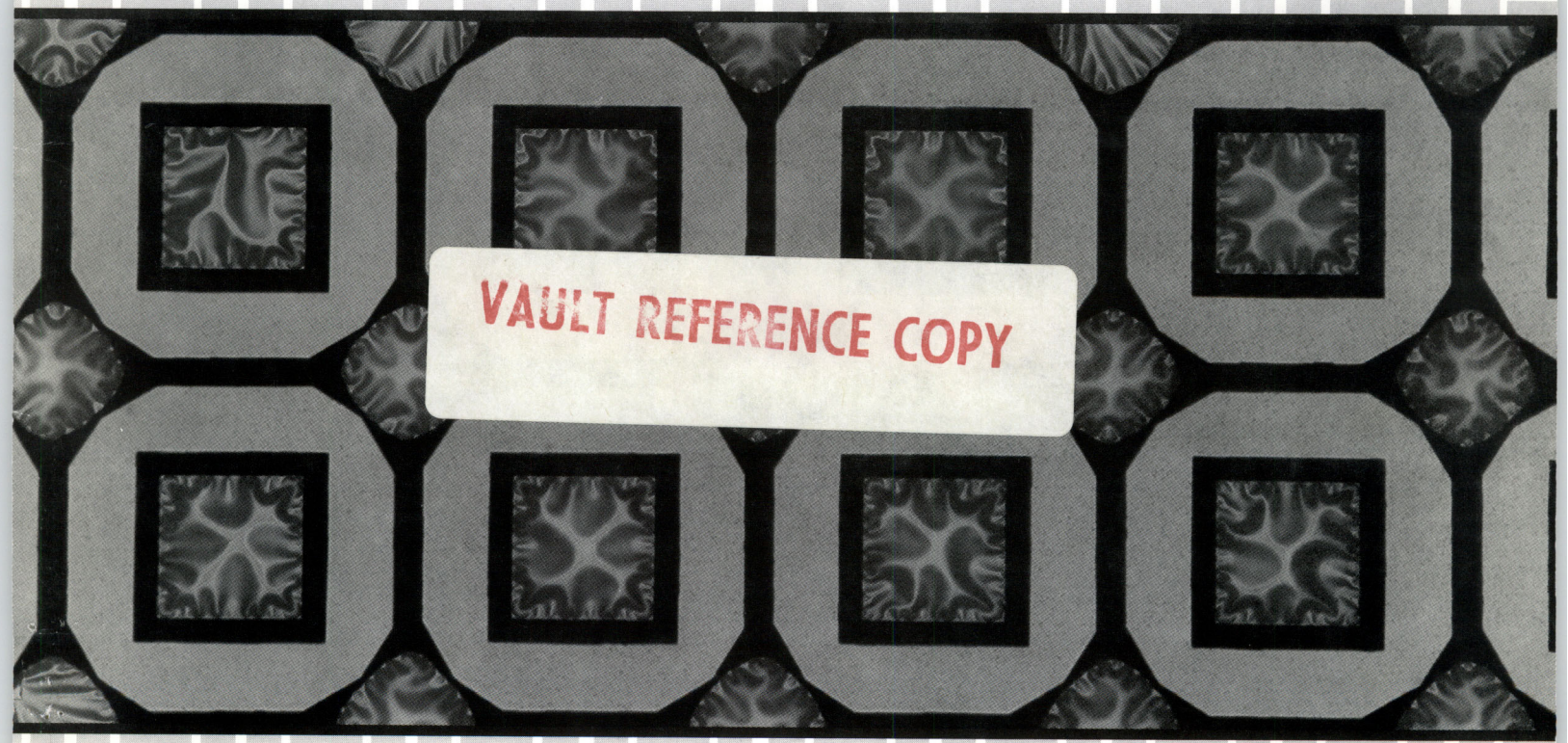

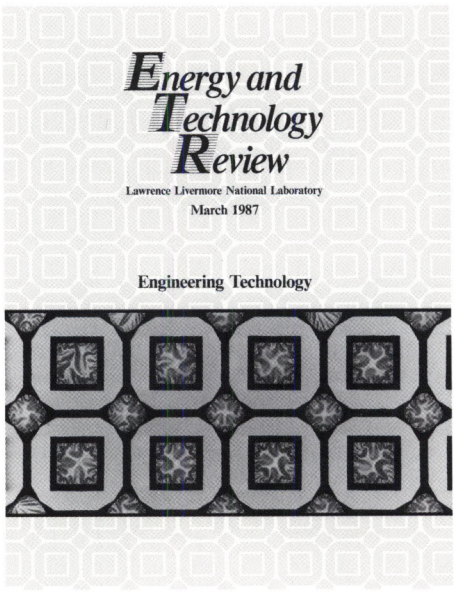

About the Cover

The free-standing silicon-nitride membranes that inspired our cover design were fabricated at LLNL by a combination of chemical-vapor deposition and etching processes. Only 1 mm square and 120 nm thick, these membranes are destined for use as diagnostics in physics experiments. Such microstructures are but one engineering response to the Laboratory's increasingly complex programmatic needs. This issue of *Energy and Technology Review* presents a sampling of the advanced technologies and diverse research in microelectronics being explored by LLNL engineers.

Prepared for **DOE** under contract
No. W-7405-Eng-48

About the Journal

The Lawrence Livermore National Laboratory, operated by the University of California for the United States Department of Energy, was established in 1952 to do research on nuclear weapons and magnetic fusion energy. Since then, we have added other major programs, including laser fusion and laser isotope separation, biomedical and environmental sciences, and applied energy technology. Our most recent major project, for the Strategic Defense Initiative Organization, is research on the free-electron laser. These programs, in turn, require research in basic scientific disciplines, including chemistry and materials science, computer science and technology, engineering, and physics. The Laboratory also carries out a variety of projects for other Federal agencies. *Energy and Technology Review* is published monthly to report on unclassified work in all our programs. A companion journal, *Research Monthly*, reports on weapons research and other classified programs. Titles of recent articles published in *Energy and Technology Review* are listed at the back of the journal. Please address any correspondence concerning *Energy and Technology Review* to Mail Stop L-28, Lawrence Livermore National Laboratory, P.O. Box 808, Livermore, CA 94550.

Printed in the United States of America
Available from
National Technical Information Service
U.S. Department of Commerce
5285 Port Royal Road
Springfield, Virginia 22161
Price codes: printed copy A03, microfiche A01

UCRL-52000-87-3
Distribution Category UC-2
March 1987

Energy and Technology Review

March 1987

Preface

Engineering, in all its various guises, is essential to Laboratory programs. As program needs become increasingly complex, engineers must examine emerging technologies for solutions to problems. Often these technologies are so new or programmatic needs are so out of the ordinary that the products of commercial and academic research are not readily available or applicable. Hence, the Laboratory must conduct its own engineering research if our programs are to benefit fully from new technologies. In this issue of *Energy and Technology Review*, we highlight LLNL research being conducted in six emerging engineering technologies: materials engineering, modal analysis, nondestructive evaluation, microwaves and pulsed power, remote sensing and signal engineering, and diagnostics and microelectronics.

The increasing demand for advanced materials for special applications requires a thorough understanding of materials behavior. For example, strong, lightweight, composite materials offer promise as structural components applicable in work for the Strategic Defense Initiative. Structures made from composite materials can also be designed to be insensitive to changes in temperature. Through the use of advanced instrumentation and computational facilities, we are working to thoroughly characterize the behavior of composites and many other materials.

Modal analysis enables us to study how structures respond as they are subjected to dynamic loads. These techniques have been successfully applied to the supporting structures for the Nova laser as well as to diagnostic canisters, ringer cranes, and other dynamic-load-bearing structures used at the Nevada Test Site.

Nondestructive evaluation techniques allow us to inspect the integrity of materials and components without damaging them. We have enhanced our capabilities for quantitative nondestructive evaluation by developing high-resolution ultrasonic and radiographic inspection systems in conjunction with data-analysis and physical-modeling techniques. Improved ultrasonic imaging methods have helped us to characterize layered structures like welds, diffusion bonds, and composite materials. Our work in radiographic inspection has enabled us to produce quantitative data on the density and homogeneity of sections of a test piece. By combining x-ray tomograms of multiple cross sections, we can construct three-dimensional images of an entire object.

Many systems, including weapons components, high-power lasers, and magnetic fusion facilities, are subjected to high-power microwaves or pulsed-power loads. We are researching ways to improve the ability of the insulators used in these systems to handle such large electrical loads. For our studies of the

effects of proposed electromagnetic weapons on current military systems, we have developed equipment to generate microwaves from pulsed electron beams. Since these large, pulsed loads must be switched rapidly, we have also developed the instrumentation to test and develop new, high-current, high-charge switches.

These advanced electronics and computerized systems produce or respond to electric signals that must be sensed and processed, frequently under less-than-ideal conditions. We are developing a number of remote-sensing and signal-processing techniques, including the application of artificial intelligence to signal processing tools; calculational algorithms to solve deconvolution problems posed when large quantities of data for multiple phenomena must be processed very quickly; and real-time processing techniques on new microprocessor chips.

To produce diagnostic devices for unusual and demanding applications, we have extended some of the microfabrication technologies originally developed for integrated circuits. We are now working on components in microelectronics, integrated optics, and passive microstructures. These include silicon and gallium-arsenide integrated circuits for high-speed digitization of diagnostic data collected from downhole experiments at the Nevada Test Site and for high-voltage switching of electro-optic systems used to shape laser pulses. Laboratory work in integrated optics is leading to faster electro-optic modulators that can switch optical-fiber signals in less than 50 ps.

Engineering technologies are appearing and changing very rapidly. To ensure that our work stays at the forefront of the field, we maintain contacts and collaborate with researchers outside the Laboratory. Once a new technology has been adequately developed at LLNL, we seek opportunities, through the Technology Transfer Initiative Program, to disseminate it to universities and industry and thus integrate it into the broader engineering technology base.

Dennis K. Fisher,
Associate Director for Engineering.

Materials Engineering

Our interdisciplinary research in materials engineering ranges from studies of state-of-the-art materials, such as composite laminates and Hadfield steels with ultrafine grains, to investigations of the aging characteristics of commonly used elastomers. Our goal is to understand quantitatively the physical and mechanical properties of materials that have important engineering applications.

For further information contact
Donald R. Lesuer (415) 422-9633,
Alfred Goldberg (415) 422-7165,
or William W. Feng (415) 422-8701.

In its broadest sense, materials engineering is a technical discipline for studying the wide variety of materials used in engineering applications. This technology ranges from the synthesis and processing of new materials to studies of corrosion and failure. Within this general discipline, we have a special interest in acquiring a quantitative understanding of the physical and mechanical behavior of engineering materials. The expanding technical requirements of Laboratory programs place an increasing demand on such materials; thus, our ability to understand, predict, and optimize material behavior has become essential. Such a quantitative understanding also suggests new materials and wide uses for old ones. Our interdisciplinary efforts involve solid mechanics, thermal sciences, materials testing, measurements engineering, and materials science.

We provide here an overview of our work on advanced materials and on deformation and fracture modeling. As an example of our work on advanced materials, we discuss superplastic behavior in Hadfield manganese steels. Finally, as an example of our work on deformation and fracture modeling, we present our theoretical and experimental study of the elastic, viscoelastic, and aging behavior of elastomers.

Advanced Materials

Our present studies of advanced materials have centered on two completely different types: composite materials and Hadfield steels. Modern composite materials consist of a matrix phase that is reinforced with a high-strength and/or high-modulus phase. The matrix phase (polymer, metal, or ceramic) is typically used to classify the material. The reinforcing phase can consist of long, continuous fibers, chopped fibers, particles, or even filaments that are continuous throughout the structure. Hadfield steels, on the other hand, were patented over 100 years ago. Our success in developing ultrafine, stabilized grains in Hadfield manganese steels has resulted in superplasticity—high elongations of 425% in this material—when deformed at elevated temperatures. The ultrafine grain size also results in high strengths at ambient temperatures. We discuss our research on superplastic behavior later in this article.

Our research interest in composite materials is largely due to their high strength-to-weight ratio and high stiffness-to-weight ratios, and because their strength, stiffness, and thermal expansion can be tailored to specific applications. For example, graphite/epoxy composites, which are polymer-based systems, have useful properties, including a negative coefficient of thermal expansion (CTE) for graphite, a composition of atoms having low atomic number, and excellent corrosion resistance.

In some applications, the CTE of a composite material must be minimized to reduce the dimensional changes of structures caused by thermal excursions. We have developed an analytical method for evaluating the CTE in composite laminates. This work provides the designer with a powerful tool because it allows for evaluation of the CTE from the mechanical and thermal properties of fiber and matrix, ply orientation, stacking sequence, and volume fraction of each phase. Figure 1 shows the results for a graphite/epoxy composite in which we obtained good agreement between theoretical prediction and experimental data and demonstrated the possibility of a zero or near-zero CTE.

Also of interest are residual stresses introduced during fabrication because these stresses can influence part shape and performance. A project was initiated this year to develop a

micromechanical model for evaluating such stresses. This model will help designers determine the cooling path in composites that minimizes residual stresses.

The Laboratory provides extensive facilities for evaluating the mechanical, thermal, and physical responses of materials. Our unique equipment includes a high-rate servo-hydraulic test machine, a state-of-the-art axial-torsion machine, a Hopkinson split-pressure bar that is configured to apply tension, and a high-resolution, thermal-expansion apparatus. In addition, we have advanced capabilities for testing fracture toughness, studying acoustic emission, fabricating composites, and performing engineering measurements.

Deformation and Fracture Modeling

Our experimentally based work on the modeling of material deformation and fracture criteria incorporates the advanced capabilities of finite-element computer codes, such as DYNA2D and NIKE2D (see Ref. 1).

We now have three projects that will increase our capabilities in this area:

- We are studying fracture modeling in elastic-plastic materials of interest to the Laboratory's weapons program. In the experimental portion of this work, we are studying crack growth as a function of stress state, strain rate, and temperature. We will compare our results with a numerical analysis of the tests in which the J integral (an established criterion in fracture mechanics) is used to define a critical damage region at a crack or notch tip in the material.
- Our work on a thermal-plastic material model will provide a general assessment of the model's suitability and limitations, as well as a basis for developing an improved model to represent a wider range of materials. The study involves experimental and analytical evaluations of the thermoplastic response of 304L stainless steel and uranium in simple, well-characterized tests.
- We are evaluating the strength of composite laminates as a function of the state of stress in assessing the suitability of failure criteria.

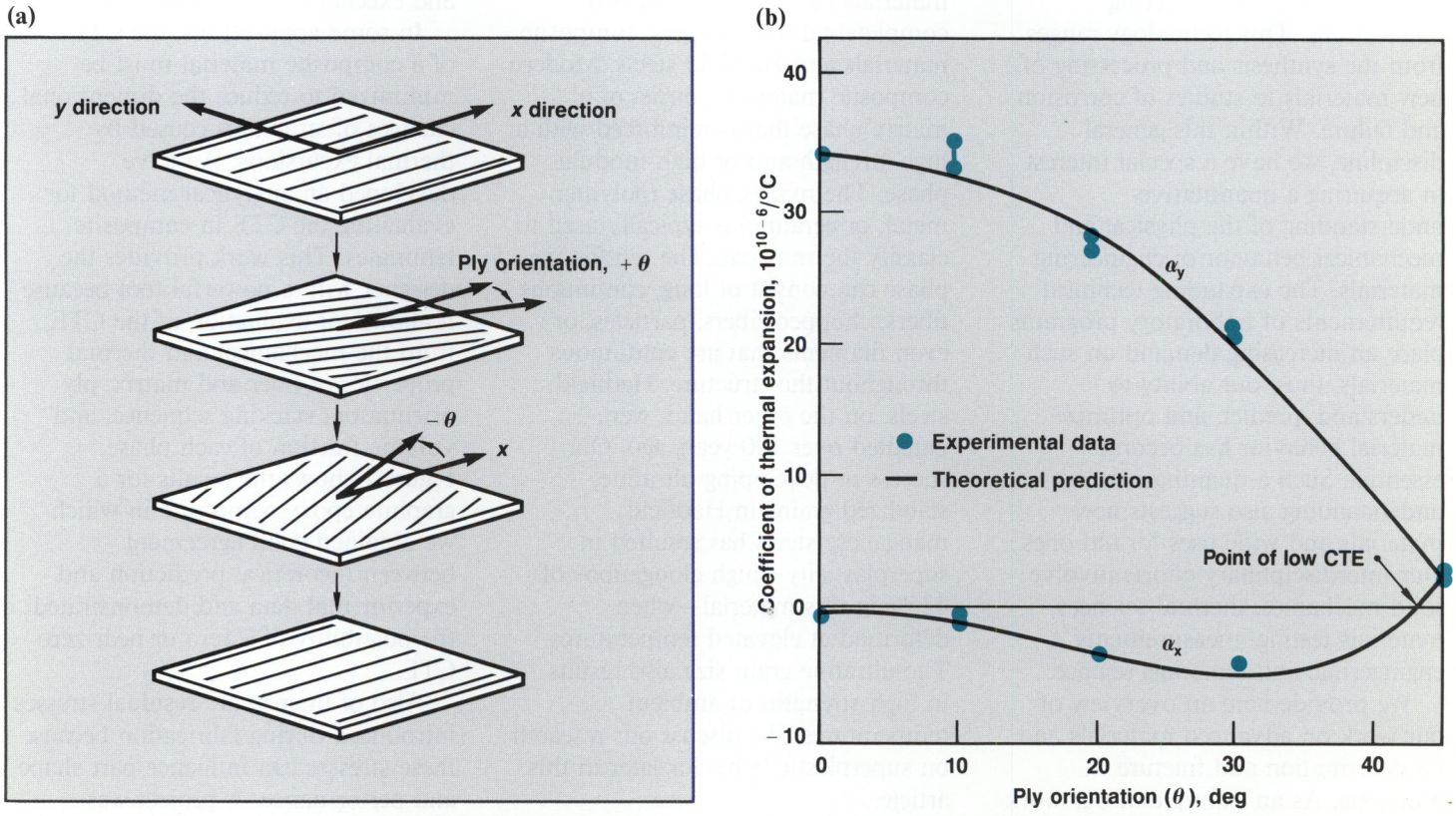

Figure 1. (a) A laminate can be constructed by stacking several layers of a graphite/epoxy composite. Certain orientations of graphite fibers (denoted by hatching) with respect to the x direction shown here will minimize the coefficient of thermal expansion. (b) A computer code enables us to determine the angle that minimizes the CTE for a given sample. The graph shows good agreement between experimental and theoretical results for two laminates (α_y and α_x). A zero or near-zero CTE is obtained in the x direction at a ply orientation of about 43 deg.

Another example of our work in fracture modeling is our multidisciplinary effort on the single-point diamond-cutting process; this effort involves both experimentation and computer modeling.[2] We are treating the modeling of chip formation during machining as a problem in crack growth that can be studied quantitatively with the J integral. Such work will improve our understanding of the diamond-cutting process and allow better prediction and control of dimensional accuracy, surface finish, and other important characteristics.

Superplastic Behavior in Hadfield Manganese Steels

Hadfield manganese steels were patented by Sir Robert Hadfield in 1883. Except for minor alloying additions, their basic composition has not varied since they were introduced. These iron-base alloys typically contain 1.0 to 1.4 wt% carbon and 12 to 14 wt% manganese, have unusually high toughness, and are highly resistant to wear under repeated impact abrasion. When subjected to such impact, the surface rapidly increases in hardness while the underlying material maintains its high toughness and strength.

Hadfield steels are used in wear-impact applications, such as mining, farming, and oil drilling, and in railroads and construction. They have been used for light armor and army helmets and in various moving components involving metal-to-metal wear. However, the material is difficult and costly to machine, usually requiring abrasive cutting tools. Because of the difficulty in forming and fabrication, the steels are used primarily in castings and, to a lesser extent, in simple wrought shapes.

We evaluated the possibility of making Hadfield steels amenable to superplastic forming and thereby of producing components that need no machining. In addition, because of the fine grain size required to achieve superplasticity, we expected to obtain improvements in room-temperature properties.

Superplasticity

The recent development of superfine, stable microstructures in some metal alloys led to extraordinarily high tensile ductility, sometimes in excess of 1000% tensile elongation at temperatures between 0.4 and 0.6 K of their melting point. This remarkable behavior is referred to as superplasticity. Materials capable of superplastic properties have great technological potential for two reasons. First, they can be readily formed into highly complex shapes at elevated temperatures. Second, they remain strong and ductile at low temperatures. There are many commercial applications of superplasticity in titanium, nickel, and aluminum alloys and of developments in iron-based alloys.[3]

One of the main requirements for superplasticity[4] is the presence of an ultrafine, equiaxed microstructure that remains stable while being deformed at the superplastic temperature. Such a grain structure, typically 1 to 5 μm in diameter, can be maintained either through the presence of an intimate mixture of two or more ductile phases or by the presence of a fine dispersion of a second phase. Another requirement is that the strain-rate sensitivity index for the material achieve a value of at least 0.4 (typically 0.4 to 0.7) at the elevated temperature and strain rate for which the grain-size stability is maintained. This index has a value of 1 for a Newtonian fluid and represents ideal superplasticity. It is a measure of the material's ability to minimize the growth rate of localized necking (reduction in cross section) during tensile deformation. Such necking would lead to early failure.

The index can be obtained from the expression $\sigma = k\dot{\varepsilon}^m$, where σ is the flow stress, k is a constant, $\dot{\varepsilon}$ is the strain rate, and m is the strain-rate sensitivity index. To determine m, a sample is tested in tension at a constant elevated temperature over a series of strain rates. Figure 2 shows the logarithm of the stress developed versus the logarithm of the corresponding strain rate. The value of m is the slope of this plot. Superplasticity would be expected for strain rates below that indicated by the dashed line, where $m > 0.4$.

Figure 3 shows a superplastic tensile sample before and after deformation. The material is a carbon steel containing 1.6 wt% carbon with a ferrite grain size of <2 μm and fine dispersions of carbides. Elongation at 650°C and at an initial strain rate of 1%/min was over 1100% prior to fracture.[5] This ultrahigh-carbon steel

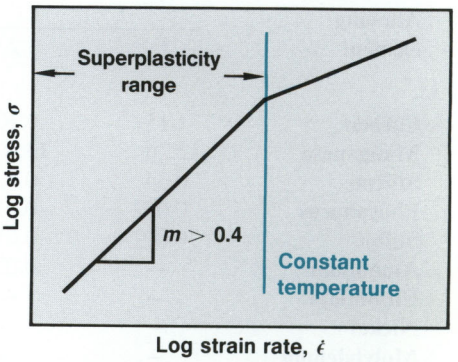

Figure 2. The value of the strain-rate sensitivity index m is obtained from the slope of the logarithm of stress versus the corresponding logarithm of strain rate. The superplasticity range is expected for $m > 0.4$.

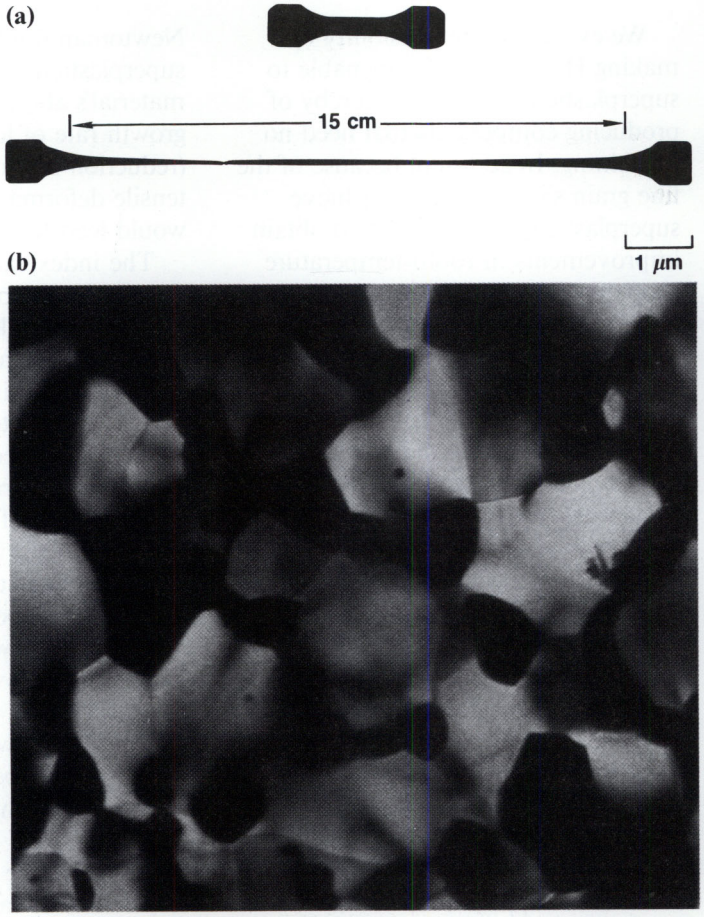

Figure 3. (a) A sample of superplastic 1.6 wt% (ultrahigh) carbon steel is deformed in tension at 650°C to yield an elongation of 1125%. (b) The microstructure of this material reveals ultrafine grain size and carbide particles.

is usually quite brittle; however, with its ultrafine microstructure, elongations of 25% or more and tensile strengths of over 800 MPa are attainable at room temperature.

Thermomechanical Processing of Hadfield Manganese Steels

In commercial use, Hadfield manganese steels consist of a single phase, namely austenite (a face-centered-cubic crystal structure), and grain sizes ranging from 0.5 to 10 mm for castings or 0.05 to 0.5 mm for wrought products. To make these steels superplastic, it is necessary to reduce the grain size by about one order of magnitude (from 0.05 to 0.005 mm). Given the high carbon content of such steels, we attempted to obtain the required ultrafine grains and to limit grain growth at elevated temperatures by developing fine carbide dispersions. We followed the method analogous to that used for ferritic, body-centered-cubic steels that have been made superplastic.[5] Table 1 shows our selection of eight steels,

Table 1 Elements (listed by wt%) used to alloy the iron in eight steels we selected for investigations of superplasticity.

Alloying element	Steel sample							
	1	2	3	4	5	6	7	8
Carbon	1.15	1.70	1.40	1.38	1.10	1.44	1.62	1.10
Manganese	12.26	13.49	13.20	16.30	13.64	13.26	14.07	12.50
Silicon	0.34	0.72	0.05	0.07	0.01	0.01	0.01	0.73
Phosphorus	0.032	0.019	0.010	0.010	0.004	0.003	0.004	<0.030
Sulfur	0.002	0.012	0.006	0.007	0.012	0.010	0.010	<0.005
Aluminum	—	0.02	0.25	0.09	0.004	0.004	0.004	<0.05
Chromium	—	—	0.12	0.04	0.048	0.013	0.013	0.33
Nickel	—	—	0.29	0.19	0.017	0.003	0.007	<0.10
Molybdenum	—	—	—	—	—	—	—	2.01

listing their alloying elements; this selection provided us with a range of carbon for the carbides and of manganese for stabilizing the austenite against transforming at low temperatures.

Using the method developed for ferritic steels together with sections of the iron-carbon-manganese equilibrium phase diagram, we defined several alternative procedures for thermomechanical processing. We selected 800°C, which is in the two-phase austenite-plus-carbide range, as the initial temperature for evaluating the stability of microstructures and testing for superplasticity.

Thermomechanical processing began with a redundant series of forging upsets starting at 1125°C and terminating at 800°C to refine the austenite grain size, break up the coarse carbide structures, and produce a convenient size for further processing. We typically obtained forged bars 50 × 50 mm in cross section and about 50 cm long. The bars were cut into short lengths to be used in evaluating different procedures to obtain the optimal final microstructure for superplasticity. One example of the processing steps that yielded ultrafine grain sizes is as follows:

- Isothermal rolling at 750°C from about 50 to 7.5 mm thick.
- Recrystallization annealing at 800°C.
- Two series of cold-working with an intermediate 800°C annealing.
- One final 2-hr annealing at 800°C.

Grain Sizes Obtained

Figure 4 shows our success in obtaining grain sizes in the range of 3 to 5 μm through thermomechanical processing. The final grains are about one-tenth original size. Figure 5 shows the results of our superplasticity tests to evaluate the rate-sensitivity index *m*, where the shaded area corresponds to the range in which superplasticity may be expected.

We tested several samples at initial, constant strain rates of either 1 or 4%/min at 800°C. The elongations ranged from 225 to 420%; these values are practical for superplastic forming, although higher strain rates would be desirable.

The room-temperature tensile properties for various samples subjected to different processing histories can be compared to those properties reported for commercially developed microstructures. For our ultrafine microstructures, we obtained values of

- 960 to 1050 MPa for ultimate tensile strength.
- 13 to 16% for elongation.
- 450 to 520 MPa for yield strength.

Our values for ultimate tensile strength correspond to the high range reported for commercial alloys. Our elongations are relatively low;

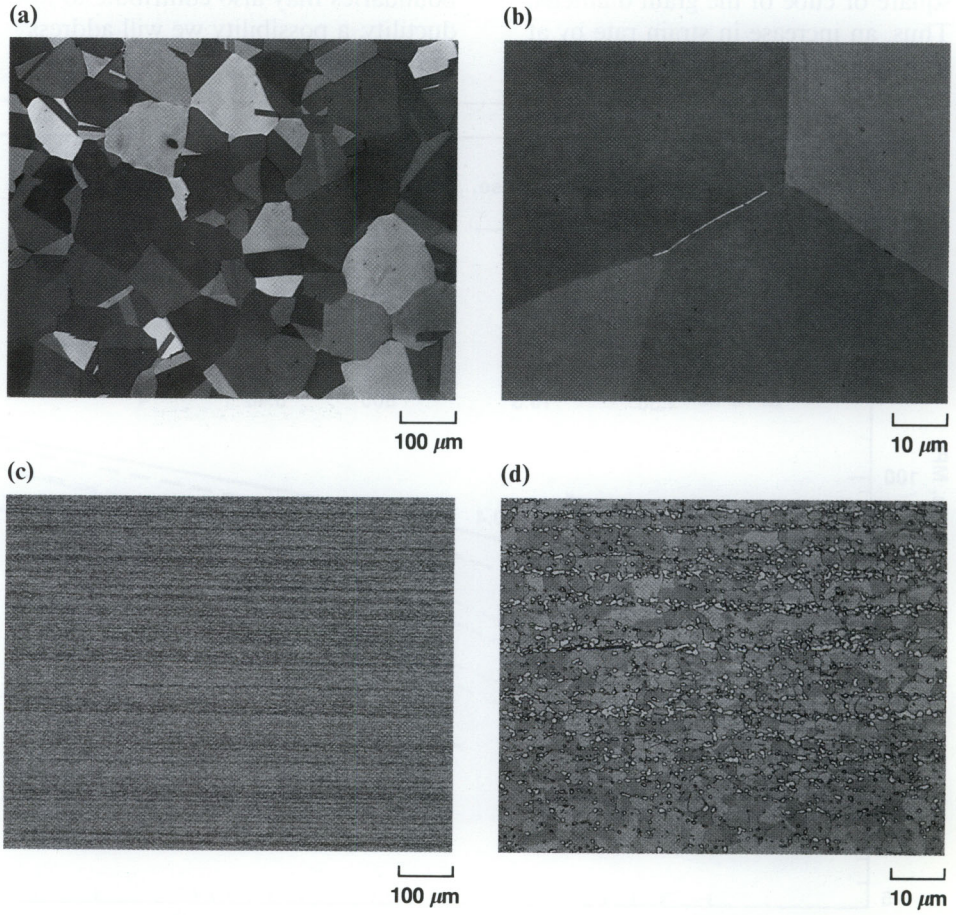

Figure 4. The microstructure of hot-rolled Hadfield manganese steel is shown as the material was received at (a) 100 × and (b) 1000 × magnification. After redundant forging and thermomechanical processing of the steel, we were able to reduce the grain size to about 3 to 5 μm as shown in these photomicrographs taken at (c) 100 × and (d) 1000 × magnification.

however, our superior yield strengths would be important for improving dimensional stability during impact and would provide greater resistance to wear and impact penetration. High yield strengths together with sufficient ductility to withstand adiabatic shear bands would make the material an attractive armor candidate against high-velocity projectiles.

Future Work on Superplasticity

In the superplasticity range, the strain rate varies as the inverse to the square or cube of the grain diameter.[4] Thus, an increase in strain rate by at least one order of magnitude should be obtainable by reducing the grain size to about 1 to 2 μm. We are evaluating the strain-rate sensitivity index for grain sizes of 2 to 3 μm.

The reduction in ductility that we obtained could be associated with the distribution of carbides. We are evaluating a new process whereby fine carbides are first introduced into steel of 100% austenite structure while it is being warm rolled at 430°C. The austenite structure of the steel can be completely retained at room temperature. Impurities in the grain boundaries may also contribute to low ductility, a possibility we will address in the future.

Rheological and Aging Characterization of Elastomers

Elastomeric materials, such as rubber seals and cushions, have been used in structures for many years. The materials are generally studied only in terms of their elastic properties because information on the other mechanical properties of elastomers is incomplete. In fact, elastomers often exhibit rheological (deformation) and aging behavior. The magnitudes of these time-dependent changes are often large enough that they cannot be neglected.

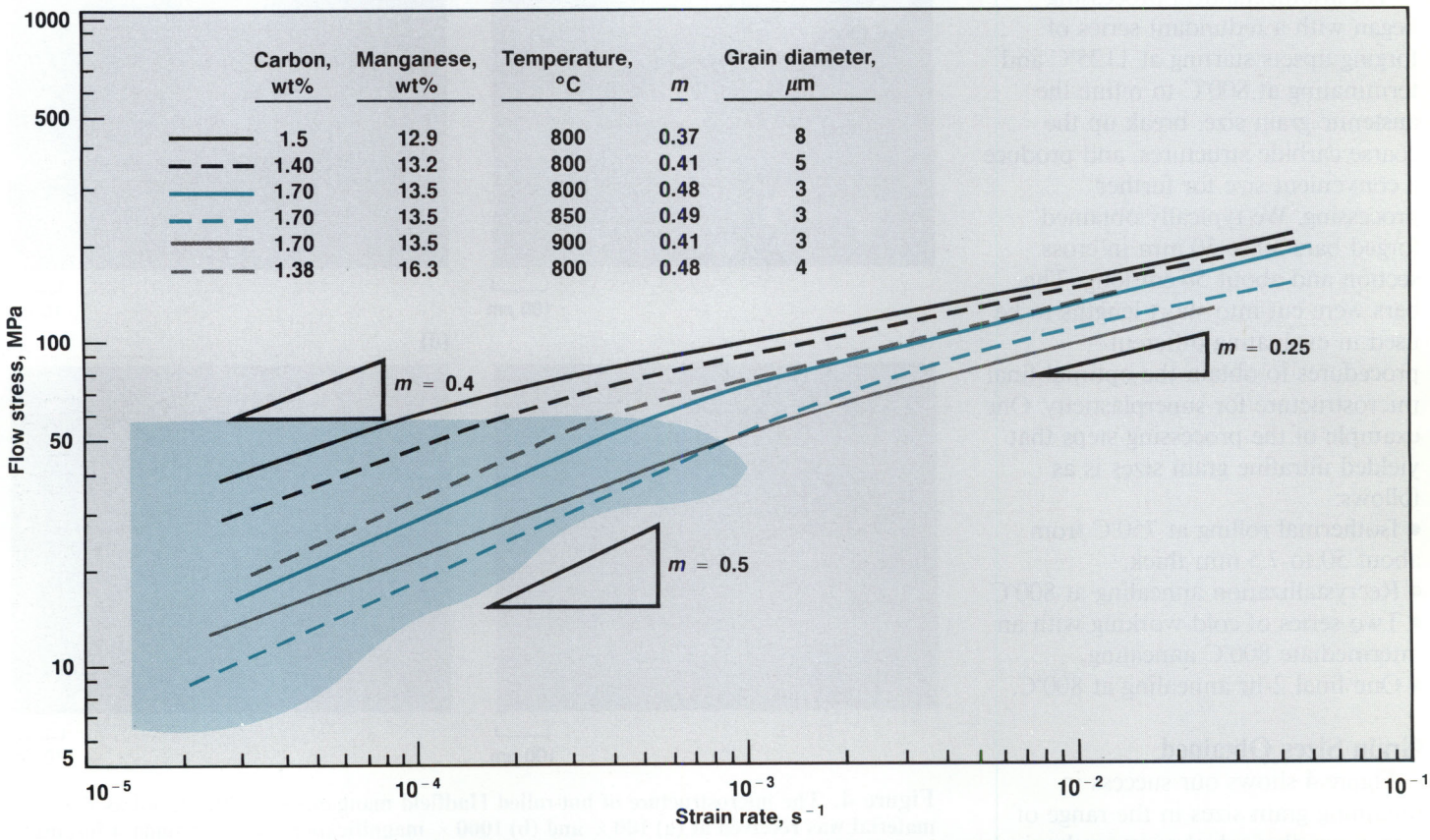

Figure 5. To obtain the strain-rate sensitivity index m for our samples of Hadfield manganese steel, we used the change-in-strain-rate method during tensile testing in a protective argon atmosphere. The superplastic region, where $m > 0.4$, is shown as the shaded area.

In practical applications, our lack of understanding of elastomers often causes severe design deficiencies. Examples include the deteriorating elastic properties of rubber bands and seals, the possibility of a malfunction in mechanical systems due to the aging of elastomeric cushions, and the accident involving the space shuttle Challenger, which was caused by loss of resiliency of rubber o-ring seals.

To date, few analytical and experimental studies on the time-dependent properties of elastomers have been attempted because both geometric and material nonlinearities must be included. The addition of rheological and aging effects makes such work quite difficult. We have developed a constitutive equation for the viscoelastic and aging characteristics of elastomers subjected to large deformations. In addition, we have designed an experiment for quantitative determination of these mechanical properties.[6,7]

Our theoretical formulation is based on determining the deformed configuration of a plane, circular membrane under an inflating pressure. We included both geometric and material nonlinearity in the constitutive equations.[8,9] The theoretical value for strains can be as large as needed; however, for practical applications these values are limited by the fracture strength and are usually less than a few hundred percent. While our treatment is for the effects of temperature aging, the constitutive equations can be readily extended to other types of aging as well.

Our experimental work was designed to show the viscoelastic effect of a deformed elastomeric membrane. Before designing the experimental apparatus, it was necessary to decide whether to perform a relaxation test or a creep test. (A relaxation test measures the decrease in the force needed to keep the dimensions of a piece of stretched material constant; conversely, a creep test measures the change in the deformation of the material if the stretching force is kept constant.) The theoretical study clearly showed an instability point at which the initial rise of the inflating pressure is followed by a fall as deformation increases. Therefore, a creep test would have two or more membrane configurations for each inflating pressure. Furthermore, the relatively flat pressure-deformation curve beyond the instability point would have produced inaccurate results, so we selected a relaxation test.

Figure 6 shows a thin latex rubber membrane inflated by air. An infrared photosensor that was connected to a solenoid valve controlled the maximum height of the deformed membrane by closing an air-intake valve; opening the air-intake valve allowed for decreasing pressure during the relaxation test. A pressure transducer, which was sensitive to within ± 5 Pa, was coupled with a digital voltage converter for data acquisition, and data were automatically recorded by a microcomputer.

Specimens were aged under stress-free conditions in an oven at 50°C for 0 to 109 days. The specimens were cooled at room temperature before relaxation tests began. Figure 7 shows the experimental results for aged disks of latex rubber in terms of the inflation pressure required to maintain a fixed height over time. From such data, we can observe the horizontal and vertical shifts of the relaxation curves with aging and determine the viscoelastic material properties (the long-term elastic material constant and the viscoelastic relaxation function).

Figure 8 shows the values of two aging material properties over time, which can be obtained from the stress-relaxation curves in Figure 7 and from our constitutive equations. The term α is derived from the vertical shift in pressure (stress) from an aging time of 0 days. Similarly, the term β is derived from the horizontal shift over time. In latex rubber, α

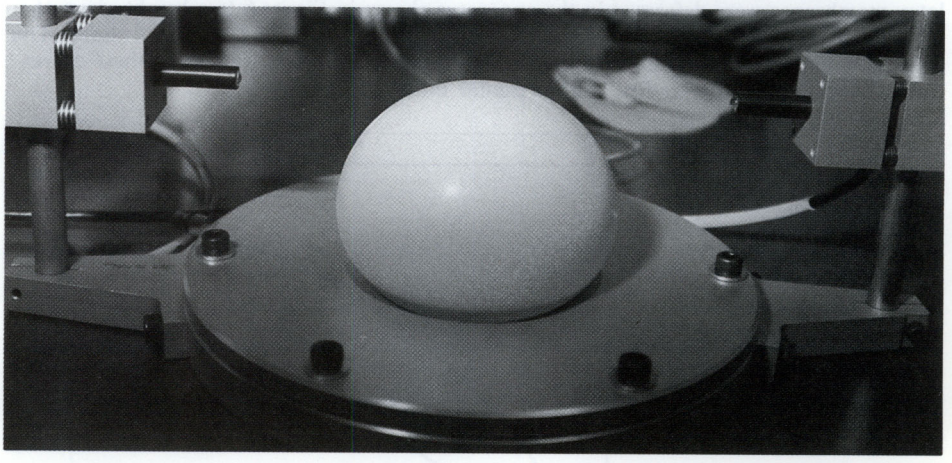

Figure 6. Apparatus for relaxation measurements. Thin membranes were clamped by an annular plate and deformed by air pressure from below. The deformation was fixed at, for example, 6 cm at the pole or apex of the latex. A light beam and photosensor sensed the height of the pole and regulated the air pressure. To prevent the maintenance of deformation in excess of 6 cm by a given mass of air, the inflating system was given a slow leak. This system kept the height of the deformed membrane to within 0.001 cm. The pressure transducer was accurate to within ± 5 Pa.

changes moderately whereas β changes significantly.

While our experimental method shows the effects of temperature aging, the procedure for obtaining material properties can be readily extended to other types of aging. Once the time-dependent properties of elastomers have been determined, it becomes possible to predict the mechanical behaviors of such widely used materials as rubber bands and seals, of mechanical systems containing elastomeric cushions, and of the o-ring seals used in the space shuttle.

So far, our experiments have verified every phenomenon revealed by the theoretical analysis. Our experimental procedure has proved to be versatile and effective. We are encouraged to extend our analysis to understand other factors that affect the material properties of viscoelastomers and to develop theories to understand the macroscopic material properties themselves in terms of molecular structure.

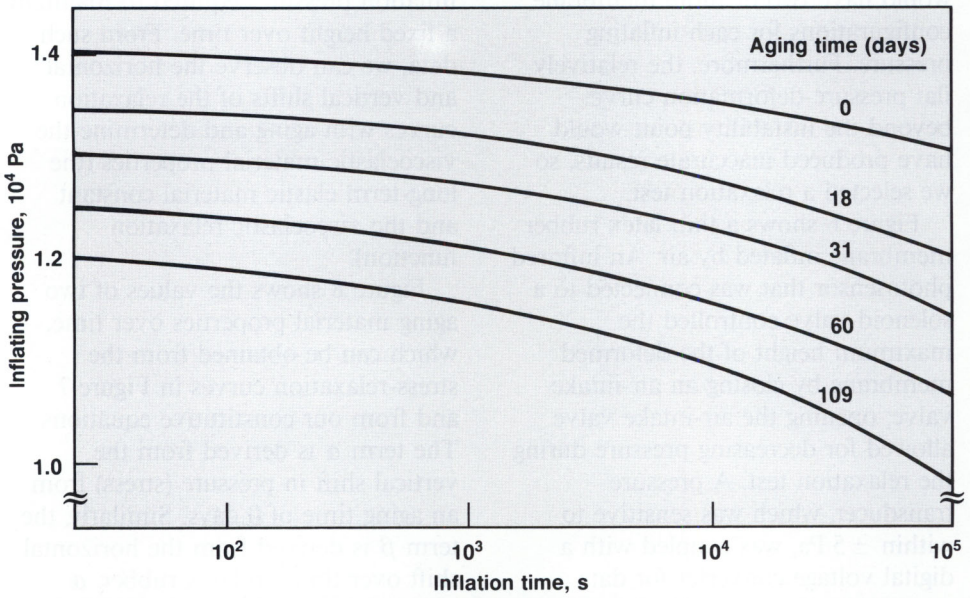

Figure 7. Results of relaxation measurements on temperature-aged latex. Thin (0.076 cm) latex membranes were deformed in the apparatus shown in Figure 6 to a height given at the pole or apex. The latex had been temperature aged at 50°C for the periods shown. Our equations imply that material relaxation is an exponential process; therefore, these curves can be superimposed by vertical and horizontal shifts.

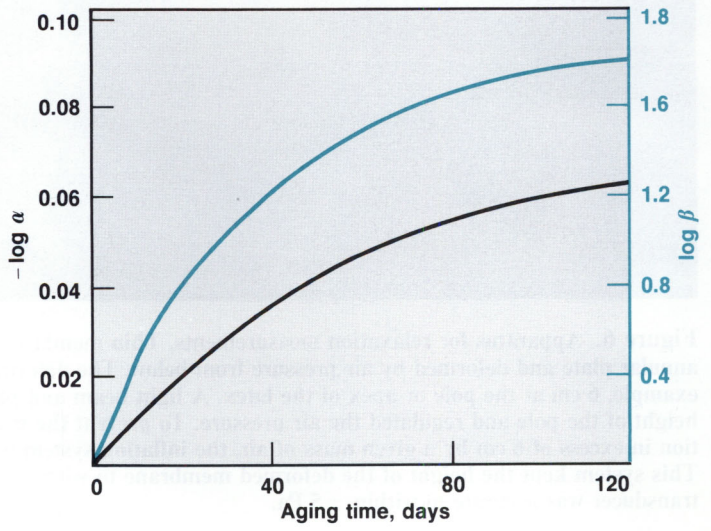

Figure 8. The values of the aging material properties log α and log β, as a function of the duration of temperature aging at 50°C.

Key Words: advanced materials; composite laminate; elastomer—rheological behavior, aging; Hadfield manganese steel—superplasticity; single-point diamond-cutting process; superplastic behavior.

Notes and References

1. These codes are discussed in greater detail in the October 1986 issue of *Energy and Technology Review*, Lawrence Livermore National Laboratory, Livermore, CA, Rept. UCRL-52000-86-10 (1986), p. 18.
2. For more information on our diamond-cutting process, see the January 1986 issue of *Energy and Technology Review*, Lawrence Livermore National Laboratory, Livermore, CA, Rept. UCRL-52000-86-1 (1986), p. 16.
3. *Superplastic Forming of Structural Alloys*, N. E. Paton and C. H. Hamilton, Eds. (Am. Institute Mech. Eng., Warrendale, Pennsylvania, 1982).
4. For additional requirements for superplasticity, see O. D. Sherby and J. Wadsworth, "Overview of Superplasticity and Superplastic Forming Processes," *Mater. Science Technol.* **1**, 925 (1985).
5. O. D. Sherby, T. Oyama, D. W. Kum, B. Walser, and J. Wadsworth, "Ultrahigh Carbon Steels," *J. Metals* **37**, 6 (1985).
6. W. W. Feng, "The Viscoelastic and Aging Characteristics of Polymers," *Polymer Engineering and Science* **27**, 2 (1987).
7. W. W. Feng, *Rheological and Aging Characteristics of Elastomers*, Lawrence Livermore National Laboratory, Livermore, CA, Rept. UCRL-94146 (1987).
8. R. M. Christensen, "A Nonlinear Theory of Viscoelasticity for Application to Elastomers," *J. Appl. Mech.* **47**, 762–769 (1980).
9. W. W. Feng, "A Recurrence Formula for Viscoelastic Constitutive Equations," *Proc. Int. Conf. Comput. Mech.* (Tokyo, Japan, May 25-29, 1986), vol. II, pp. 77–82.

Quantitative Nondestructive Evaluation

By combining new developments in high-resolution inspection systems, data analysis, and acoustics models, we have improved our ability to quantify both the ultrasonic and radiographic inspection processes, thereby allowing us to evaluate more precisely the properties of materials and the integrity of components without damaging them.

For further information contact Ronald D. Streit (415) 422-7045, Gregory A. Clark (415) 423-4268, or James M. Brase (415) 422-6992.

Nondestructive evaluation (NDE) technology enables us to inspect materials, components, and complete assemblies for service worthiness without damaging them. A typical NDE system consists of several essential elements:

- An energy source with which to probe an object.
- A test object that modifies the incoming energy in a well-defined manner.
- A receiver for measuring how the energy is altered by the test object.
- A means of recording and analyzing the data.
- A means of interpreting the data and making a decision based on the results.

There are many examples of nondestructive inspection in everyday life. A familiar example of NDE is tapping on an object to learn something about its internal structure. When we tap on a wall to locate beams, our finger provides the energy to launch sound waves into the wall. The wall modifies the incoming sound waves, depending on the presence or absence of a beam. Our ear receives and measures the changes in sound. Our brain records and interprets the differences in sound. At the Laboratory, we use a variety of methods, including radiation-based inspection (e.g., radiography, gauging, and tomography), ultrasonics, optical techniques, and techniques using magnetic particles and dye penetrants.

Applying NDE methods is a science, but interpreting the data is often more an art. For example, in ultrasonic inspection, the signal modified by the test sample contains a wealth of information about inhomogenous regions within the sample (e.g., voids, cracks, and bond lines) and the material properties of the bulk (e.g., residual stress, surface texture, thickness, and modulus). However, only the peak amplitude of the modified (reflected) sound is generally recorded and interpreted. While the received signal is rich in data about the internal structure, most data are simply discarded, rendered uninterpretable, or manipulated into the background clutter of the signal. Color representations of digital ultrasonic information often resemble abstract art more than scientific data.

The recently developed ultrasonic test bed and the reflection-mode acoustic microscope at LLNL now enable us to accurately transmit, receive, and measure precise and complete ultrasonic data. The ultrasonic test bed, shown in Figure 1, is a 14-axis, two-transducer, ultrasonic inspection system for examining objects as large as 1 × 2 m. This unique facility can accurately scan complex, arbitrary geometries by independently manipulating two transducers and the test sample. The acoustic microscope, shown in Figure 2, is a high-precision, ultrasonic inspection system. Recently we have used it to investigate flat surfaces, layered structures, and thin sheets. Its precise scan system has a positioning resolution of 1 μm and an absolute scan size of 0.75 m.

Another nondestructive technique, standard radiography, compresses three-dimensional information from an object onto a two-dimensional image plane. After viewing the image (generally, this means a visual inspection of film), we can make an empirical judgment about the importance of observed indications. However, the film itself may contain additional data that may not be obvious to the unaided eye. We enhance our interpretation of radiographic data by optimizing the radiographic process for the specific object of the inspection. Optimization is accomplished by tailoring the x-ray spectrum (energy), the film and processing variables, the radiation flight path, and the electronic imaging device. By carefully characterizing each component in the radiographic process, we can begin to develop quantitative information about the density and homogeneity of a given part. However, such techniques provide only averages through the depth of an object.

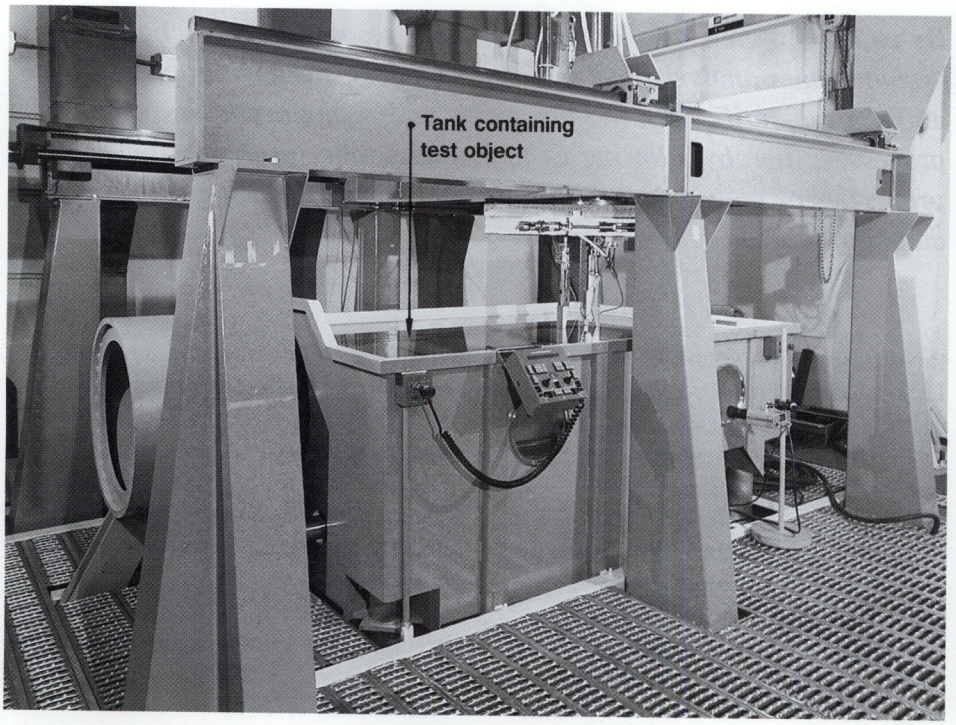

Figure 1. The ultrasonic test bed is an ultrasonic inspection system capable of scanning large (1 × 2-m) objects with complex geometries. We conduct ultrasonic inspections by independently manipulating two transducers attached to the two vertical-scan mechanisms and by rotating the test object around a horizontal or vertical axis. We control fourteen independent axes of motion to complete a specified scan with this system.

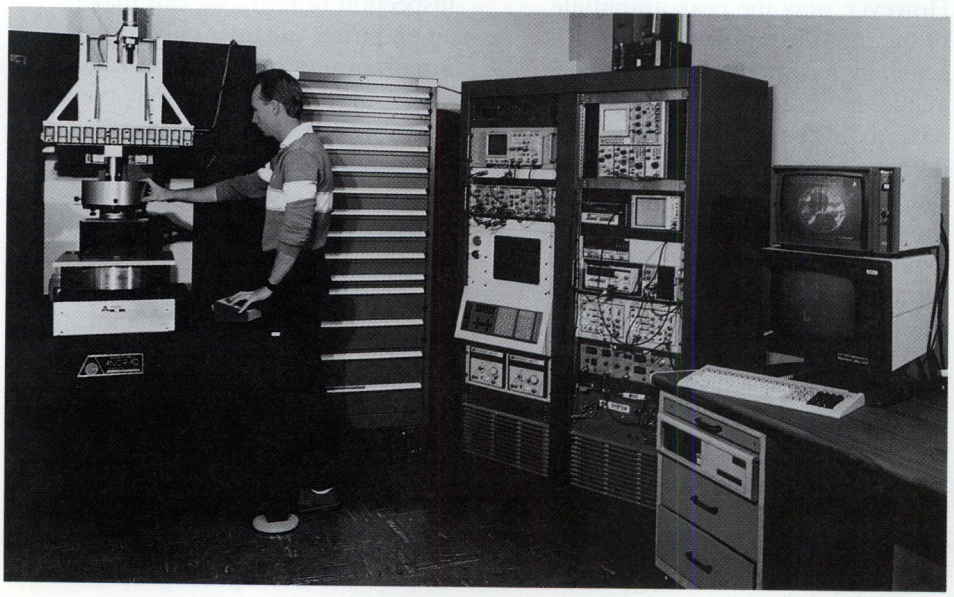

Figure 2. The acoustic microscope is a very-high-precision, single-transducer, ultrasonic inspection system. The scan-position resolution of 1 μm requires a solid base and stiff supporting members. For inspection of flat surfaces, this system has been optimized with frequencies of from 1 to 100 MHz. The electronics and computers used for signal generation and detection, stage manipulation, and data acquisition are also shown.

Because we often need details of the third dimension, we required a fundamental change in the imaging technique. Consequently, we have devised new techniques for three-dimensional inspection of internal structure by combining x-ray tomograms of multiple cross sections within an object.

By developing and combining high-quality inspection systems, data analysis, and reliable physics models, we have greatly extended our ability to obtain quantitative information with ultrasonic and radiographic imaging. In this article, we discuss two important problems in NDE: characterizing layered structures with ultrasound and obtaining quantitative, three-dimensional images with x-ray tomography. As with all our NDE techniques, these procedures do no damage to a potentially valuable test object. We also discuss some of the future directions for our tomography and ultrasonic research.

Ultrasonic Characterization of Layered Structures

In NDE applications, many materials can be viewed as layered structures. Examples include butt welds used to fuse metals in waste containers and in various weapons; pinch welds for closing tubes; electronic solid-state devices composed of layers of silicon and other material; diffusion bonds; and light-weight graphite/epoxy materials used in mechanical structures.

For a typical problem involving a layered structure, our goal is to detect and quantify layer boundaries and bond failures between layers by means of broadband ultrasound pulses in the range of 1 to 25 MHz. An ultrasonic transducer, shown in Figure 3, is mounted on an acoustic microscope

and acts as both transmitter and receiver. By fixing the spatial position of the transducer and measuring the pulse echo response, we obtain a time waveform (an A scan) of the part being studied. The A scan shown in Figure 3 contains information about scattering and material properties in the z direction. If we scan the part along a line in the x direction, we collect a family of A scans that forms a two-dimensional image (a B scan) of the cross section of the part. Such scans are often difficult to interpret because the measured signals are distorted by the transducer, the material's wave-propagation paths (including scattering, losses, dispersions, and multiple reflections), and instrument noise. The signal-processing algorithms we are developing will improve our ability to interpret these measured signals in terms of the physical objects they represent (see the article on signal processing that begins on p. 46).

Models for Layered Structures

In analyzing layered structures, we must solve a fundamental problem known as system identification, deconvolution, or signal restoration.[1-7] We assume that the transfer function of the material is linear, which is usually a good approximation. Then the problem is to find the impulse response of a linear, time-invariant system representing the propagation of waves in the layers. Given a measurement-signal A scan, $y(t)$, and

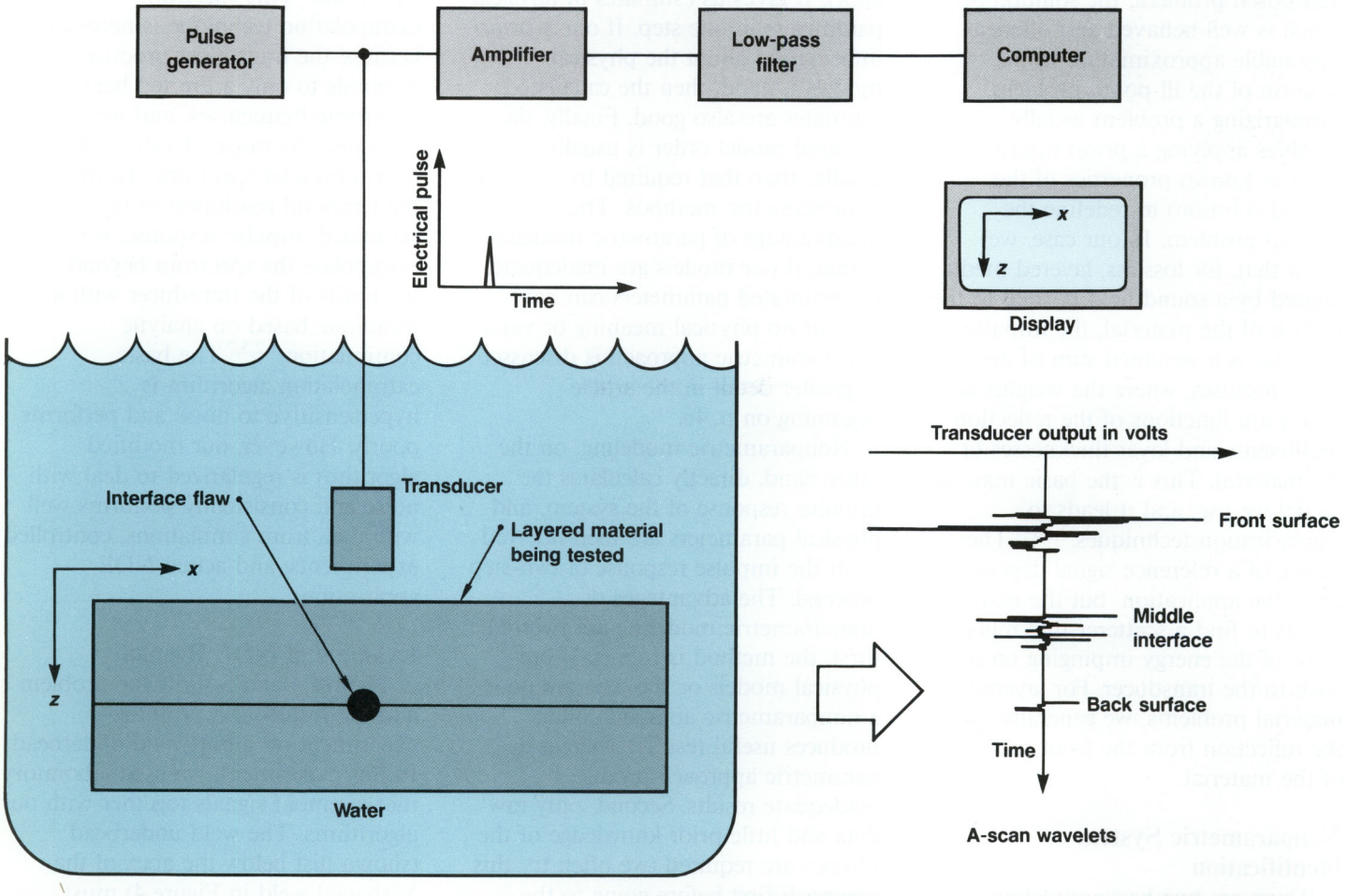

Figure 3. We obtain an ultrasonic A scan by exciting a transducer with a broadband pulse and then recording the sound field reflected from the layered medium. Although an approximately ideal electrical pulse is applied to the transducer from the pulse generator, the sound field produced by the transducer consists of ringing wavelets. The wavelets (A scan) shown here have passed through the material and have been received by the transducer. For a two-layer problem, the three wavelets from top to bottom represent reflections from the front surface, middle interface, and back surface, respectively. The object of this evaluation is to detect any hidden anomalies in the interface.

a reference A scan, $x(t)$, we must find the operator $h(t)$ such that $y(t) = x(t) * h(t)$, where the asterisk denotes convolution. The obvious approach is to find the inverse operator $x^{-1}(t)$ such that $h(t) = x^{-1}(t)\ y(t)$. In practice, the problem is ill posed,[8] and determination and implementation of the inverse operator can be difficult or impossible.

The approach to dealing with ill-posed problems is to regularize them.[5] We do so by defining an associated well-posed problem, the solution of which is well behaved and offers a reasonable approximation to the solution of the ill-posed problem. Regularizing a problem usually involves applying *a priori* information (such as known properties of the desired solution) to redefine the original problem. In our case, we know that, for lossless, layered media excited by a sound field normal to the surface of the material, the impulse response is a weighted sum of delayed ideal impulses, where the weights and delays are functions of the reflection coefficients and layer thicknesses of the material. This is the basic material model we use, and it leads to regularization techniques.[2,3,5–7] The choice of a reference signal depends upon the application, but the major goal is to find a scatterer that reflects most of the energy impinging on it back to the transducer. For layered-material problems, we generally use the reflection from the front surface of the material.

Nonparametric System Identification

There are two basic modeling approaches available to us: parametric and nonparametric methods. Parametric modeling, or model-based estimation, requires that we calculate the values of model parameters that, we hope, represent some physical properties of the system being modeled. This approach implies *a priori* knowledge of the physics, and we use this knowledge to our advantage. Once the model parameters are calculated, the impulse response of the system can be calculated by simulation, if desired. Most often, however, the impulse response need not be calculated because the model parameters contain the desired information.

Parametric modeling has several advantages. It is simple and easy to apply. It gives us estimates of physical parameters in one step. If our *a priori* information about the physical models is good, then the calculated estimates are also good. Finally, the required model order is usually smaller than that required by nonparametric methods. The disadvantage of parametric modeling is that, if our models are inadequate, the estimated parameters can have little or no physical meaning or value. Our parametric approach is discussed in greater detail in the article beginning on p. 46.

Nonparametric modeling, on the other hand, directly calculates the impulse response of the system, and physical parameters are then inferred from the impulse response (a two-step process). The advantages of nonparametric modeling are twofold. First, the method is robust. If our physical models or the data are poor, a nonparametric approach often produces useful results, whereas a parametric approach produces inadequate results. Second, only raw data and little prior knowledge of the physics are required (we often try this approach first before going to the trouble of using model-based approaches). The disadvantage of nonparametric modeling is that a two-step process of impulse-response estimation and then physical parameter estimation is required. If the known physical models are good, then parametric modeling performs better than nonparametric modeling.

In our nonparametric approach, we first estimate the impulse response $h(t)$ of the layered medium and then use $h(t)$ to estimate the reflection coefficients and layer thicknesses. We have obtained the best results by using a two-step procedure. We start with a constrained optimization algorithm for system identification. We then apply a regularized, band-limited-spectrum extrapolation algorithm.[2] This spectrum extrapolation technique is necessary because the transducer produces and responds to only a limited band of ultrasonic frequencies, and we wish to extend the range of valid solutions over a broader spectrum. To improve the temporal resolution of the estimated impulse response, we extrapolate the spectrum beyond the limits of the transducer with a technique based on analytic continuation.[1,2,5,7] The basic extrapolation algorithm is hypersensitive to noise and performs poorly. However, our modified algorithm is regularized to deal with noise and consistently performs well with data from simulations, controlled experiments, and actual NDE applications.

Example of NDE Results

Figures 4 and 5 show the problem and the results of a profiling experiment on a butt-weld underbead. In this experiment, we used laboratory measurement signals together with our algorithms. The weld underbead (shown just below the apex of the V-shaped weld in Figure 4) must penetrate evenly and be large enough to seal the seam effectively; the weld's uniformity and thickness, then, are the primary indicators of its integrity.

In this NDE experiment, we examined these characteristics of the underbead. The pulse resolution of the initial A-scan and B-scan images (see Figure 5) is considerably improved by our signal-processing algorithms. The result (the extrapolated scans) gives a more accurate measurement of weld thickness. The significance of this work lies in its application to actual

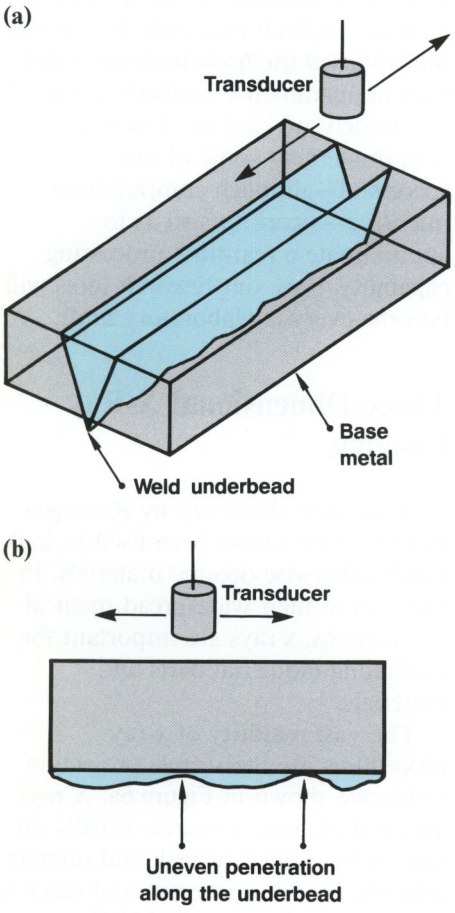

Figure 4. Diagram of an ultrasonic NDE application, showing (a) top view and (b) side view of a wedge-shaped weld (blue) and the bead of weld material that penetrated the seam. For proper welding, the underbead should be of uniform thickness and penetration. Our goal is to detect and measure accurately any places along the seam where the bead did not penetrate sufficiently. By ultrasonic scanning along the butt weld, we obtain a B-scan image of the weld underbead or region of penetration.

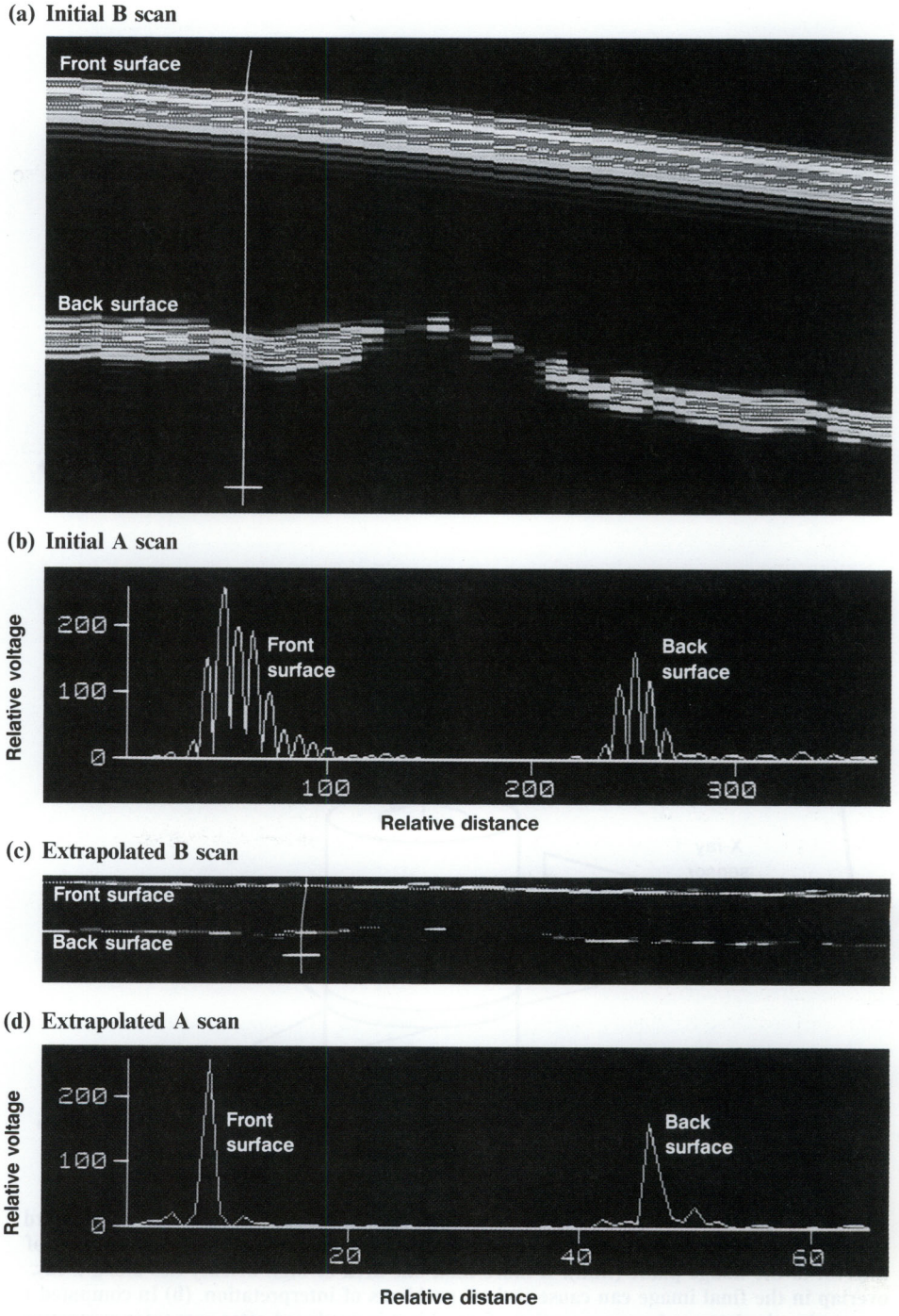

Figure 5. Initial and extrapolated scans of a butt weld such as the one shown in Figure 4. (a) The actual B-scan image of the front and back surfaces of the weld reveals the uneven penetration at the back. However, the image consists of broad lines where we would like to see narrow ones. (b) One rectified A-scan image selected from the B-scan image of this material (at the vertical white line) shows broad, imprecise pulses. (c) We estimated this improved B scan from that in (a) and (b), using our processing technique. (d) Pulses in the A scan are now narrow and more precise. The narrower lines and pulses in the extrapolated scans indicate enhanced temporal resolution; this makes it easier to determine the weld depth.

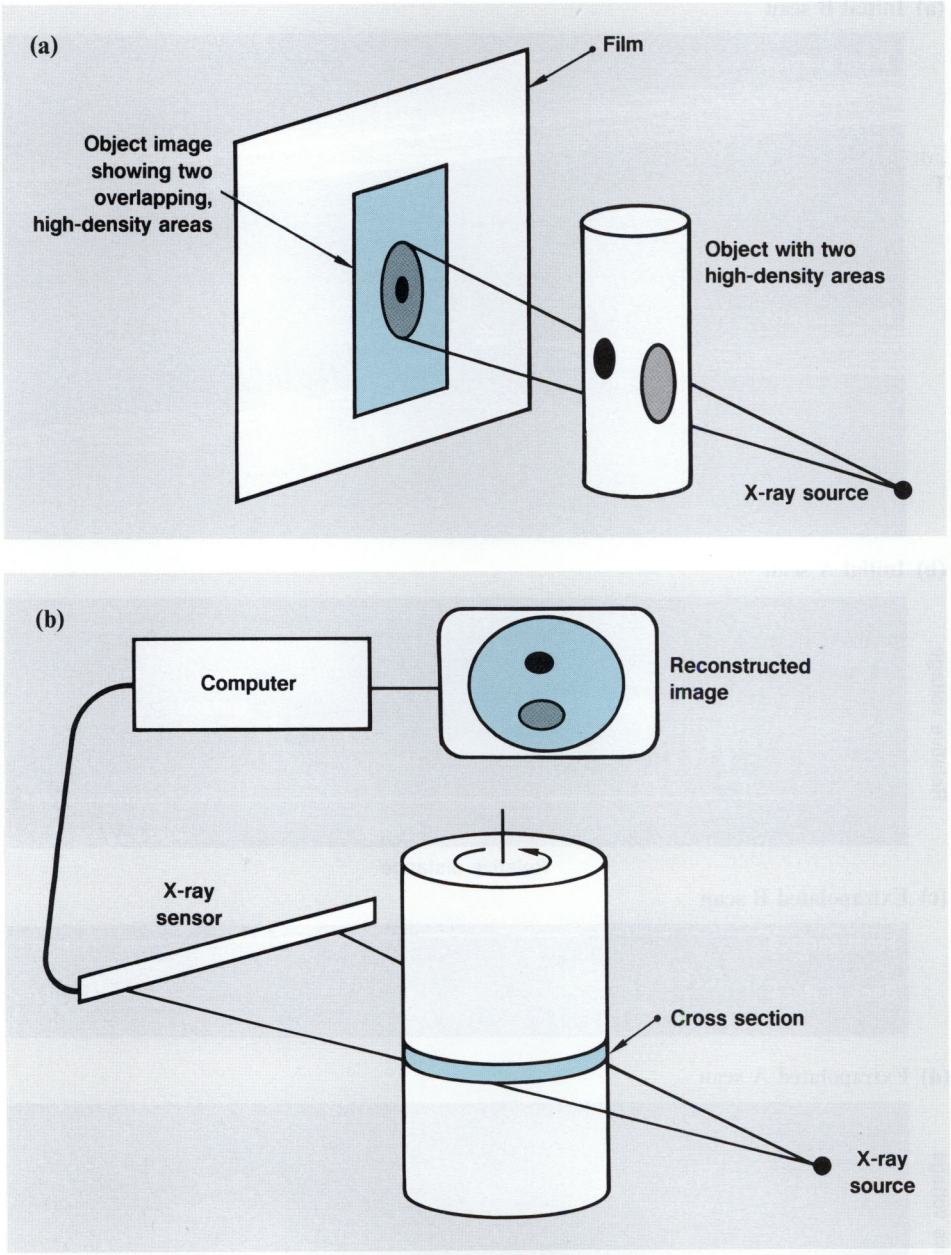

Figure 6. Conventional radiographic and computed tomographic images. (a) In standard radiography, an image is formed by projecting x rays from a source through the object of interest to the image plane (film). If more than one area of high density lies along a ray, overlap in the final image can cause serious problems of interpretation. (b) In computed tomography, the image of a cross section of an object is produced after computer reconstruction of multiple projections (only one is shown in this diagram). Thus, the problems of overlap and ambiguous images are eliminated.

laboratory signals, and in the useful, practical solutions to an ill-posed problem that our regularization techniques make possible.

Future Research

As part of our NDE research, we are pursuing more difficult problems in signal restoration, including the use of parametric modeling methods for lossy media; problems in which the excitation signal strikes the test material at an angle; and experiments on more difficult materials. In general, model-based methods perform better than nonparametric methods when the models are realistic. Our plan is to implement some of our successful—although computationally intensive—algorithms so as to approximate a real-time processing capability; thus, our research tools will become everyday laboratory tools.

Three-Dimensional X-Ray Imaging

Since their discovery by Roentgen in 1887, x rays have been used to look inside otherwise opaque materials. In addition to their widespread medical applications, x rays are important for evaluating industrial parts and materials.

The vast majority of x-ray procedures use the simple projection technique shown in Figure 6a. X rays are emitted from a source, usually an x-ray tube, travel through and interact with the object of interest, and reach a detector (often photographic film), where the intensities are recorded. It is important to understand that the three-dimensional information about the object of interest is compressed or integrated along the ray paths into a two-dimensional image. Therefore, if

two important features overlap along the paths, they will also overlap on the image. Such overlap can obscure important features and make it impossible to diagnose the material characteristics at a specific location.

Computed tomography (CT) was developed as a means of retrieving the three-dimensional information that is lost in standard radiographic imaging. One way of understanding the three-dimensional distribution of an object is to look at it from many angles. The human visual system is very good at building three-dimensional models from a series of views. This technique is fundamental to CT (see Figure 6b). We get a computed tomograph by mathematically combining several radiographic images taken from different angles. This combination, performed by a computer, produces a three-dimensional image of the x-ray-attenuation distribution. This CT technique has revolutionized medical imaging over the last decade and promises to do the same for NDE imaging.

We believe that substantial improvements are possible with CT imaging. To succeed, we must address both the spatial accuracy of imaging and the radiometric accuracy of our measurements. In the past several years, we have done a great deal of work in quantitative film radiography. We have measured the areal densities of objects to accuracies of less than 5% with spatial resolution on the order of 100 μm. To produce accurate three-dimensional images, we need to address several problems, including the statistical nature of x-ray production, the limitations of easily available x-ray sources, and the wide variety of materials and geometries that must be considered in industrial imaging. We believe these problems can be overcome and that we can produce quantitative three-dimensional x-ray images with spatial resolutions on the order of a few microns.

Fundamentals of Computed Tomography

There are four essential elements in a CT system:

- A radiation source.
- A turntable or similar device that positions the test object at various angles.
- A detector that measures the intensity of x rays penetrating the test object.
- A computer that uses the measurements to reconstruct the cross-sectional image.

Reconstructing the data from an entire object can take many hours of computer time; however, we can select single cross sections to form our reconstructions (see Figure 6b) because we are usually interested in relatively small areas. The individual slices can then be stacked to form a three-dimensional image, if one is needed. Here, we discuss scanning and reconstructing single slices.

For the example shown in Figure 7, a projection is defined as the one-dimensional set of data formed by sampling the x-ray intensity at n points P_1, P_2, ..., P_n along line D. The measured intensity at each point is called a ray sum. Projections are acquired at a set of m discrete angles q_1, ..., q_n. We typically record from 300 to 500 points per projection and 90 to 180 projections over 180 degrees.

Figure 8a shows an object with a single area of high attenuation and three projections. Such data are stored in a computer and then are submitted to a reconstruction algorithm. The simplest algorithm describes back projection, basically an inversion of the radiographic imaging process (see Figure 8b). An empty x,y data array representing the area to be reconstructed is set up in the computer. Each projection is then smeared across the array at the recording angle. At each pixel, new values are added to the current total. The areas of high attenuation in the projections overlap in the actual location of the feature that causes them. The resulting values in the output image are much higher in these areas. A reconstruction from simple back projection can never be perfect because we add some values

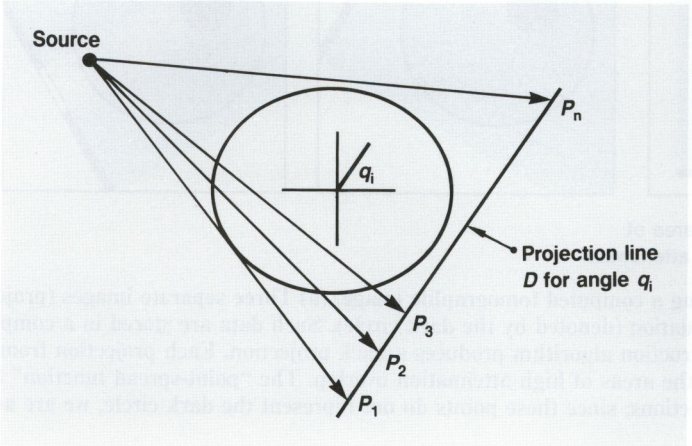

Figure 7. We most commonly use the fan-beam imaging geometry in our computed tomography studies. X rays from a source are projected to line D, where the intensity is measured at points P_1 through P_n. An entire set of data is taken for each angular position q_i.

into areas that should have none. The star-shaped pattern in Figure 8b is known as the point-spread function of the back projection. More complicated reconstruction techniques attempt to minimize the points of the star and to reproduce the original feature more accurately.

Radiation Sources for CT

The three x-ray sources we have used are standard x-ray tubes, radioisotopes, and synchrotron radiation. Each source has advantages and disadvantages, but tubes and isotopes are used most often because they are readily available. Tubes produce a broad spectrum that complicates the quantitative analysis of the projection data, while radioisotope sources have a narrower spectrum but tend to be of low intensity.

Synchrotron radiation is produced by particle storage rings, such as the one at the Stanford Synchrotron Radiation Laboratory at Stanford University. When the paths of high-energy charged particles (electrons in the case of the Stanford facility) are bent by magnetic fields to keep them in the ring, they emit wide-band radiation. The spectrum ranges from visible light to medium-energy x rays of approximately 60 keV. This source is very intense and well-collimated. Indeed, the intensity is high enough that we can separate a very narrow spectral band and still have intensities three orders of magnitude higher than that of most x-ray tubes. Unfortunately, there are few synchrotron sources and their cost is high. We expect this situation to change rapidly as their usefulness for x-ray applications becomes apparent.

X rays interact differently with materials, depending on the energy of the x-ray photon involved. For this reason, we would like to use single-energy or monochromatic radiation, such as that from radioisotopes or synchrotrons, when possible. Monochromatic radiation greatly simplifies image reconstruction and allows us to perform more detailed quantitative analyses of the materials being inspected. With monochromatic sources, we can also do new types of imaging that are impossible with wide-band sources. For example, because various materials absorb x rays differently, we can produce images of selected materials in a mixture (and even of different chemical phases) with a tunable monochromatic source.[9] In a mixture of copper and nickel, we should be able to see the three-dimensional distribution of either material individually. This technique would have important applications in diagnosis and quality control. The ideal source for such work is synchrotron radiation.

CT Detection and Measurements

The oldest and most commonly used radiation detector is photographic film. Film has several drawbacks for CT, the most

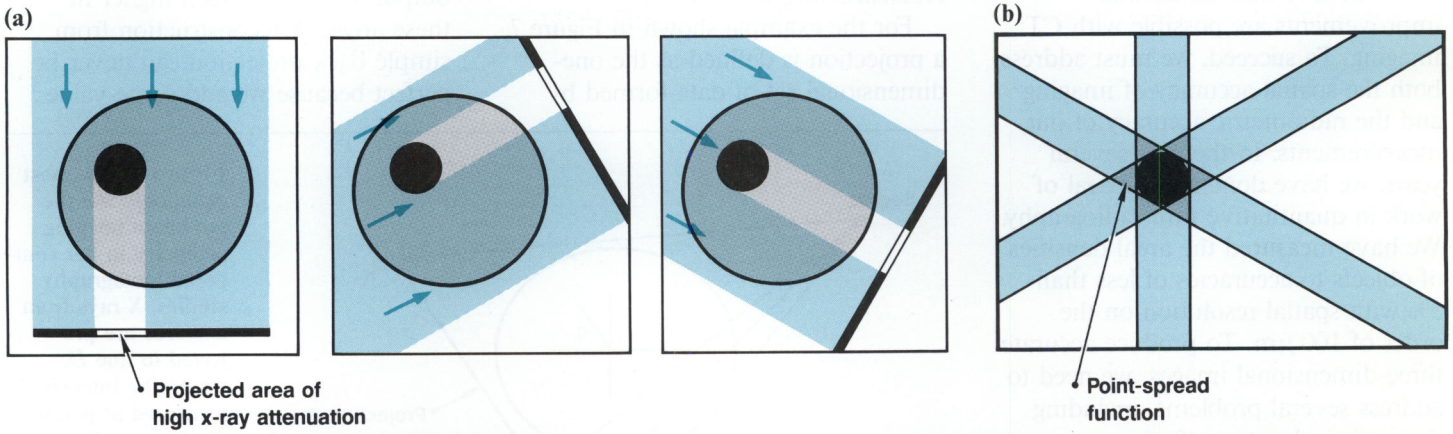

Figure 8. Reconstructing a computed tomographic image. (a) Three separate images (projections) are shown for an object with a single area of high x-ray attenuation (denoted by the dark circle). Such data are stored in a computer for later reconstruction of the image. (b) The simplest reconstruction algorithm produces a back projection. Each projection from (a) is smeared across the array at the original recording angle so that the areas of high attenuation overlap. The "point-spread function" refers to the star-like points created by the overlapping of pairs of projections; since these points do not represent the dark circle, we are attempting to eliminate them.

important one being the difficulty in transferring the information from the film to the computer for reconstruction. In addition, film is a nonlinear detector; the darkness in the film is related exponentially to the radiation intensity, which causes many problems for reconstruction algorithms. Consequently, film is rarely used in CT.

The most common detectors for CT are various scintillating crystals that convert x rays into visible light. In the systems we have built, the crystals are used as a thin screen to convert the x-ray spatial distribution to a visible light distribution. The light then is amplified by an image intensifier and is recorded by a television camera. For a synchrotron source, the image intensifier may be eliminated because the higher x-ray intensity produces an image on the scintillator screen that is bright enough to be directly recorded.

Cameras used to convert the light signal to an electrical signal are based on charge-coupled devices (CCDs). These solid-state components measure the photon intensity on an array of photosensitive sites and produce an output voltage. CCDs work well for tomography because of their wide dynamic range and their linearity. The arrays typically consist of either 390×480 or 780×480 sites. Electrical signals from the CCDs are converted to digital numbers and sent to the computer where they are stored. A one-dimensional projection is extracted by using only a single line of the two-dimensional array of light intensity.

In making a CT, the first step is to measure the distribution of x-ray intensity at each angle with no test object present. The object is then moved into place, and data are recorded again. At each point that is recorded, we obtain two numbers: the calibration measurement I_0 and the actual measurement with the object I. The ray sum is given by $p = ln(I_0/I)$. If we have n points per projection and m projections, we then have a total of mn ray sums, which are submitted to the reconstruction algorithm.

Reconstruction Algorithms

The computer reconstruction of the CT image must take into account the geometric setup of the system, the characteristics of the x-ray source and detector, and any available *a priori* information about the test object. CT reconstruction algorithms fall into two basic groups: transform techniques and algebraic techniques.[10] Transform techniques are based on Radon's theorem, which states that any two-dimensional distribution may be reconstructed from the infinite set of its line integrals. The reconstruction operation is known as the inverse Radon transform, which consists of three parts:

- A partial derivative with respect to the coordinate along the projection line.
- A Hilbert transform.
- Back projection.

The most common reconstruction technique is a transform called filtered back projection. The partial derivative and Hilbert transform are approximated by a single filtering operation on the projection data. When the filtered projections are back projected, a good approximation of the true two-dimensional distribution is formed. The technique is popular because it is easy to implement in either software or hardware and is relatively fast. It produces high-quality images as long as the number of projections is high (that is, close to the number of points per projection).

The second category of reconstruction algorithms is the set of algebraic methods. Here, the reconstruction area is divided into a grid. The initial two-dimensional distribution is guessed at, and the set of projections is calculated from this guess. The calculated projections are compared to the actual, measured projections. The two-dimensional distribution is then changed according to the difference between actual and measured projections. The process is repeated until the error is minimized. Although usually much slower than transform techniques, this algebraic method can do a far better job when the number of projections is small (e.g., when the view is restricted and data can only be acquired at certain angles). Algorithms using algebraic techniques may also be useful if the data-acquisition time is much greater than the reconstruction time. For example, scanning with a weak radioisotope source takes hours. If we wish to do a good reconstruction from only a few projections, algebraic methods become practical.

Microfocus CT System

Standard x-ray tubes have electron beams ranging from 0.5 to 1 mm in diameter (this size determines the spatial resolution of the beam). In contrast, a microfocus tube has a beam size of approximately 10 μm. This small spot size allows us to increase the resolution by enlarging the beam spot geometrically. We believe that we can attain approximately 20-μm resolution with a microfocus CT system, which is two orders of magnitude better than that of most commercial systems.

A diagram of a complete system for CT data acquisition and display

appears in Figure 9. A microfocus x-ray tube is the source, and a 35.5-cm image intensifier produces an image bright enough to be picked up by a standard video camera. The image intensifier and camera system limits the dynamic range of our measurements to 256:1, whereas we require about 10 000:1 to obtain the measurement resolution needed for quantitative analysis. The main limitation is the 0.033-s fixed integration time of the video camera. We are changing to a system with controlled integration time, which will give us the required dynamic range and increase the sensitivity so that the image intensifier will not be needed.

The computer we are now using (a μVAX-2) can acquire data for a single cross-sectional image (180 projections) in about 5 min and reconstruct it in about 10 min. However, the reconstruction time for a three-dimensional image is much longer—85 h for a 512 × 512 × 512-pixel image. Even current medical scanners with hardwired reconstruction algorithms take 4 h to reconstruct such an image. Such times are obviously impractical for routine industrial inspections and represent one of the most challenging areas of our work. We are now looking at new ideas in parallel computer architectures to speed the reconstruction process.

Future Directions

We are trying to obtain better CT images more quickly by exploiting our *a priori* knowledge of a test object so as to decrease the amount of new data required. For example, by combining data taken from two different source-to-object distances, we can estimate and remove the scatter contribution and thus reduce one of the primary causes of error for our uncollimated CT systems. In addition, if we can characterize the effects of the x-ray imaging system, we can use image-processing techniques to improve spatial resolution.

There would be many applications for CT images that distinguished the constituent chemical elements in a test object. We are taking two approaches in an attempt to develop such a CT capability. First, we will continue our series of experiments in synchrotron CT at Stanford; by using the tunability of the synchrotron source to see fine variations in x-ray attenuation, we expect to form three-dimensional images of element and chemical-state distributions. Then, for instance, we could use CT to inspect an object for hidden corrosion. Second, we will use a standard x-ray tube source to produce images of elements. We hope to be able to separate elements by recording several images at different tube voltages and then statistically analyzing the resulting distributions. Success in this endeavor would make it unnecessary to use a synchrotron source for many applications.

Complete three-dimensional imaging of certain objects now requires an unreasonable amount of computer time, a problem that may be remedied by parallel computer architectures. We are developing a algorithm that will run on a 64-processor array. In addition to the

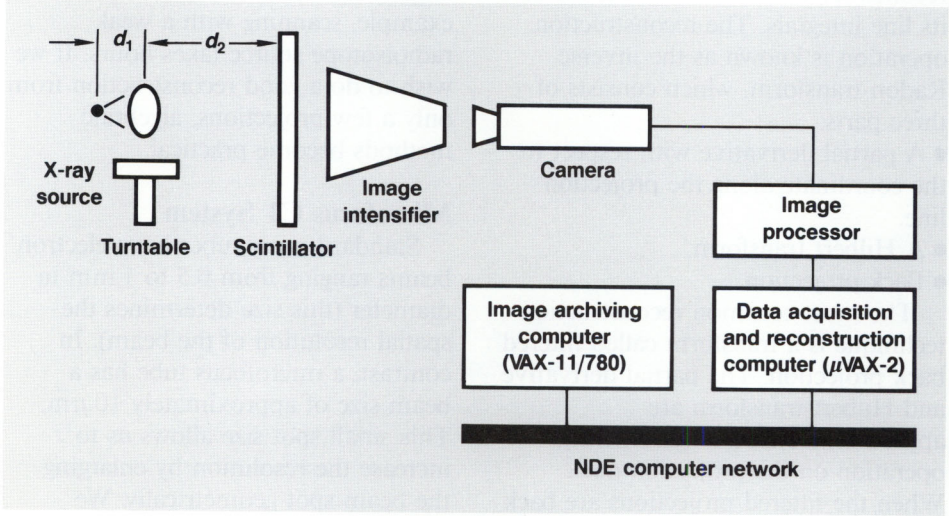

Figure 9. The microfocus computed tomography system uses a source with an effective spot size of only 10 μm compared to sizes of from 0.5 to 1 mm for standard x-ray tubes. We use geometric magnification to increase the spatial resolution of the image, where magnification = $(d_1 + d_2)/d_1$. To date, we have demonstrated a resolution of 100 μm and believe that 20-μm resolution can eventually be attained with this system. We are looking at new ways to obviate the need for an image intensifier and to speed the lengthy reconstruction time for quantitative three-dimensional imaging so that industrial applications can become practical.

problem of speed, there is the problem of interpretation. Inspecting thousands of images for small features is a tedious and error-prone job. Automating this process will require the latest techniques in computer vision and artificial intelligence: such work is just beginning.

Key Words: acoustic microscope; computed tomography; nondestructive evaluation—computed tomography, ultrasonic; signal restoration; ultrasonic test bed; synchrotron radiation; x-ray imaging.

Notes and References

1. J. W. Goodman, *Introduction to Fourier Optics* (McGraw-Hill, New York, 1968).
2. A. Papoulis and C. Chamzas, "Improvement of Range Resolution by Spectral Extrapolation," *Ultrasonic Imaging* **1**, 121–135 (1979).
3. L. Ljung, "Aspects on the System Identification Problem," *Signal Processing* **4**, 445–460 (1982).
4. J. M. Mendel, *Optimal Seismic Deconvolution, An Estimation-Based Approach* (Academic Press, New York, 1983).
5. G. A. Clark, D. M. Tilly, and B. D. Cook, "Ultrasonic Signal/Image Restoration for Quantitative NDE," *NDT International* **19** (3), 169–176 (1986).
6. G. A. Clark and F. L. Barnes, "Model-Based Parameter Estimation for Layer Problems QNDE," paper delivered at the 13th Annual Review of Progress in Quantitative Nondestructive Evaluation, University of California, San Diego, La Jolla, CA, Aug. 3-8, 1986.
7. G. A. Clark, F. L. Barnes, and G. Thomas, "Digital Signal and Image Restoration for Weld Underbead Profiling," paper delivered at the 13th Annual Review of Progress in Quantitative Nondestructive Evaluation, University of California, San Diego, La Jolla, CA, Aug. 3-8, 1986.
8. To be well-posed, the problem must satisfy three conditions. First, the solution h must exist for each element in the range space Y. Second, the solution must be unique. Third, small perturbations in Y must result in small perturbations in the solution h without the need to impose additional constraints. If any of these conditions are not satisfied, then the problem is ill-posed. For example, when noise is present in Y, even small perturbations in Y (noise) can map into large differences in the estimated values of h, and the third condition would be violated. In addition, the distortion operator x can be such that many different values of h produce the same values of Y so that the solution is not unique and does not exist because the first and second conditions are violated. Our case, in which x is the band-limiting operator, is an example of this situation.
9. Q. C. Johnson, J. H. Kinney, U. Bonse, M. C. Nichols, R. Nusshardt, and J. M. Brase, "Micro-tomography Using Synchrotron Radiation," *Proc. Materials Society Symposium* **69**, 203–208 (1986).
10. G. T. Herman, *Image Reconstruction from Projections* (Academic Press, New York, 1980).

Modal Analysis: Understanding the Dynamic Characteristics of Structures

Our investigations of the resonant frequencies and other modal parameters of structures used at the Laboratory to house experimental equipment ensure the stability and integrity of the structures during physics experiments.

For further information contact
H. Joseph Weaver (415) 422-0310.

In recent years, many of our physics experiments at the Laboratory have become highly complex, often requiring that the structures housing the experiments be precisely controlled. The need to predict the stability and integrity of such structures has grown accordingly. For example, some components of the Nova laser system are mounted on space frames that are two stories high and the length of a football field. Certain experiments involving the Nova laser require that the radiation emitted from several beams be precisely focused on a microscopic glass sphere. The target itself is housed in a large vacuum chamber mounted on a seven-story tower. We must thoroughly understand the dynamics of the mounting structures to maintain the critical alignment of this system. Our success in determining the dynamic characteristics of a large variety of structures is made possible by modal analysis to determine the frequencies at which the structure might harmfully resonate.

The consequences of neglecting modal analysis can be spectacular indeed. Failure to consider the resonant frequencies of the bridge constructed in the 1940s over the Tacoma Narrows is one of the more dramatic illustrations of why this discipline has become so essential. The bridge began to vibrate shortly after its completion and collapsed in moderate winds. During the 1960s, the turbo-prop engines used in Electra aircraft were found to resonate at the same fundamental frequency as that of the wings. Design changes were necessary to eliminate this critical problem.

In simple terms, modal analysis (also referred to as dynamic analysis or testing) allows us to ascertain the resonant frequencies of a structure. Every structure has specific, inherent frequencies at which it can be induced to oscillate or vibrate. A small force can cause substantial response motions at these frequencies. The annoying rattle in the dashboard of a car at a particular speed is a common example of a resonant frequency.

The damping and mode shapes associated with each frequency are as important as the resonant frequency itself. Damping is a measure of how rapidly the energy of the excitation force is dissipated by a structure. Mode shape is the unique spatial deformation associated with each resonant frequency. That is, a resonant frequency has its own unique contour or shape.

Imagine that a flexible wire, such as a guitar string, is fixed at both ends (see Figure 1) and then is allowed to vibrate. The first three mode shapes of this simple system correspond to

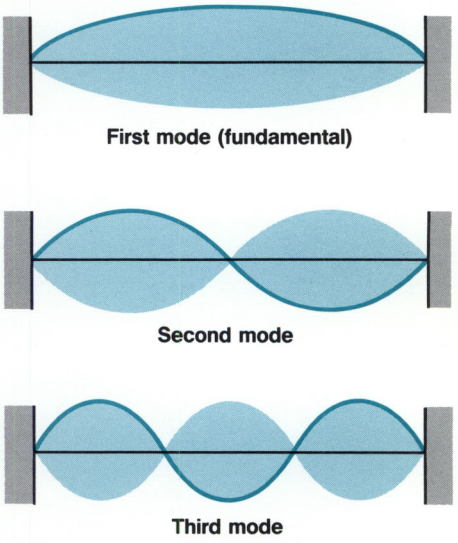

Figure 1. When a flexible wire is fixed at both ends and selectively excited, the resultant mode shapes can be observed. The first mode corresponds to a unique and relatively low natural frequency that is determined by various properties, such as length, tension, and density per unit length of the material. The second and third modes arise from successively higher vibrational frequencies.

the unique temporal frequencies at which the wire naturally vibrates. The second mode shape, for example, can only be assumed when the wire vibrates at its second natural frequency; at this frequency, it can never assume the first or third mode shape. The same phenomenon can be easily observed by removing a telephone from its cradle, pulling the cord taut, and shaking the receiver at different frequencies. The cord will assume its various mode shapes.

Determination of Modal Parameters

The Dynamic Test and Analysis Group at LLNL routinely tests large structures to determine their modal parameters. At the heart of dynamic or modal testing is the identification of load paths (or transfer functions) between various pairs of locations (nodes) on a structure. The load paths are a measure of how a force applied at one location is transferred to a response or vibrational motion at another location on the structure. For testing purposes, the nodes are chosen so that, when they are connected by straight lines, the resulting stick figure typically resembles the actual structure. In practice, the load paths are measured by applying a forcing function at one location and measuring the response motion at another. The forcing function may be a hammer blow or a random shaking motion applied with an electromagnetic vibrator. The response motion is usually measured with accelerometers.

The forcing signal and response signal are captured, recorded, fed into a digital computer, and analyzed by a type of mathematics known as Fourier analysis. The result of such analysis is an ensemble of frequency-domain functions called either frequency-response or transfer functions. Figure 2a shows a typical transfer function with peaks at certain frequencies.

The shape of a transfer function reveals valuable information concerning the dynamic properties (modal parameters) of a given structure. More specifically, the location of the peaks correspond to the resonant frequencies of the structure. The width of each peak is used to determine the damping associated with each natural frequency. Groups of transfer functions can be used to determine the mode shape or spatial characteristics of the structure (see Figure 2b). At the Laboratory, engineers use customized computer codes to analyze the shape of the transfer functions and compile the results into a modal-data parameter file. We use these data to judge the dynamic behavior and integrity of the structure in question.

(a) Typical transfer function

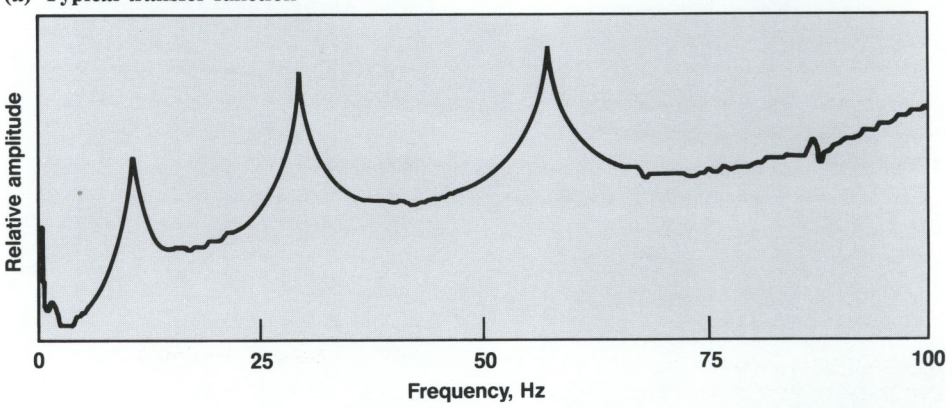

(b) Ensemble of transfer functions to reveal mode shape

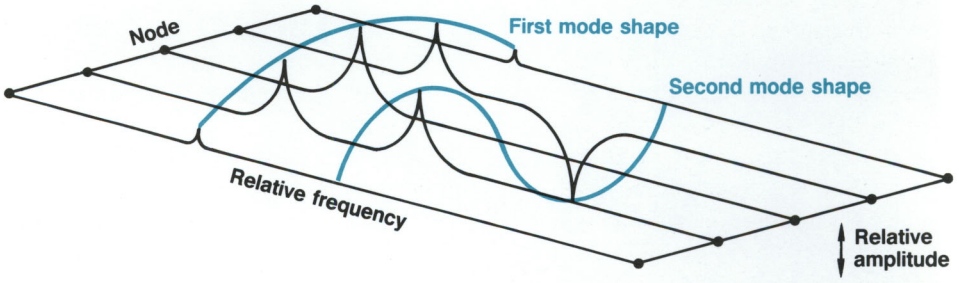

Figure 2. The modal parameters of a structure can be inferred from transfer functions. (a) The peaks of a typical transfer function correspond to the resonant frequencies of a structure. The width of a peak can be mathematically related to the damping of that particular node. (b) A series or ensemble of transfer functions is used to show how the peaks from different nodes form the mode shape of the structure. Thus, the first mode shape is the actual form that the vibration takes at a given frequency.

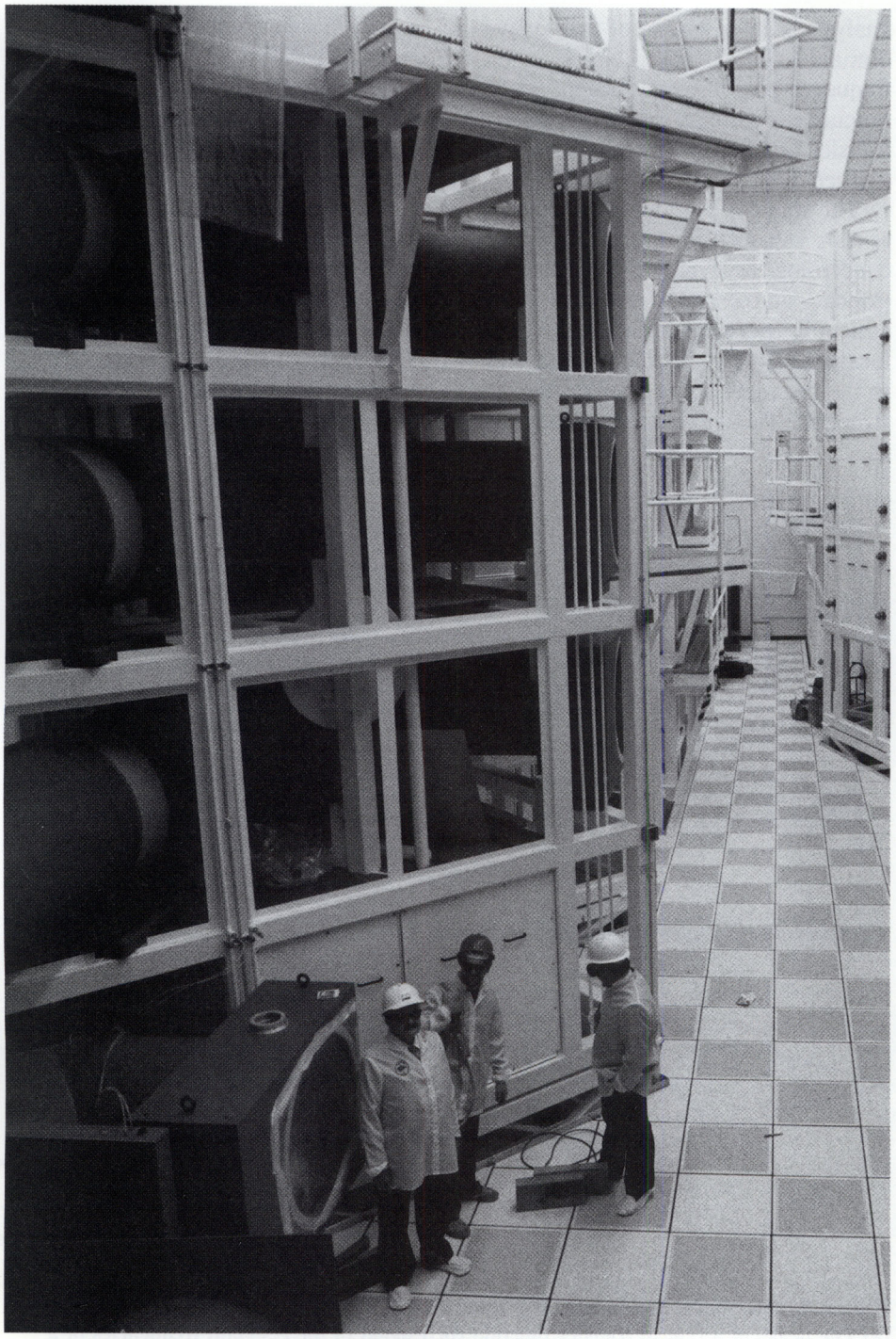

Figure 3. The switchyard tower for the Nova laser is about two stories tall and is used to mount turning mirrors that direct laser light to the target chamber. Our modal tests on the tower during early construction revealed that a slight modification of the mathematical model of the tower was required to account for stiffness arising from the mirror mounts.

Verification of Finite-Element Models

The modal parameters obtained by dynamic testing can be used to calibrate or verify a finite-element analytical model of the structure. A finite-element model is a mathematical formulation usually made from preliminary drawings or blueprints of a structure. The model is used before the structure is actually built to examine how it will behave under expected loads. Results from the finite-element analysis may then be used to make design corrections or improvements. An engineer experienced in analytical structural design can usually model a structure quite accurately. However, to ensure that a mathematical model is valid at a high level of statistical confidence, we must somehow check it against the actual physical structure.

Modal analysis is used to verify the accuracy of finite-element models by comparing the predicted modal parameters to those actually measured by dynamic testing. If agreement is reached, then the finite-element model can be considered accurate.

On the other hand, the modal testing sometimes shows that modifications must be made to the finite-element model to obtain a more accurate representation of the structure. Tests on the Nova optical-switchyard towers, which contain mirrors for the laser system, are an example of outcomes that required such modification. The towers are used to mount large turning mirrors that direct the laser beams from amplifiers to the target chamber. Before construction was completed (see Figure 3), Laser Program engineers used a finite-element model of a typical tower to determine critical stress loads and seismic stability. The model was modified to reflect the

condition of the tower in its early construction phase when we performed a modal test. Results of our modal test verified most of the predictions of the finite-element analysis. However, to obtain agreement between the first mode of the structure calculated by the finite-element method and measured by modal testing (see Figure 4), a modification in the mathematical model was required. The mirror mounts acted as gussets and added significant stiffness to the structure. In addition to mode shapes and frequencies, our modal testing determined the damping values associated with each mode. The latter outcome was important because damping estimates are not normally available from finite-element analyses.

By chance, engineers were checking the optical alignment of the Nova laser's 1.06-μm beam during a recent earthquake (the quake caused an equivalent acceleration of 0.02 *g*). The engineers were able to witness the performance of the system at a time when the towers were subjected to a very real test of structural integrity. After considerable movement of the alignment cross hairs, the beam quickly returned to the target when the earthquake subsided.

Structural Integrity Via Modal Analysis

The performance of the Nova towers makes it clear that we can use modal analysis for purposes other than to verify finite-element analyses. Once a test is made and the modal parameters are determined and recorded, those properties might be expected to remain unchanged. Nevertheless, damage, ground movement, or other time-dependent changes may affect the structure.

As an example of this essential application of modal tests, we recently conducted an experiment at the Nevada Test Site on a developmental system for emplacing diagnostic cables into a deep, underground test hole. Tensioner units control the rate and tension at which cables are lowered downhole. Figure 5 shows a skid containing ten tensioner units. One critical component of this system is a load cell that is mounted on each tensioner. The load cell generates a signal that is processed to control the tension in individual cables.

For proper operation, the structural stiffness of the spring within the load cell must be accurately established and remain reasonably stable. As it turns out, the stiffness is strongly dependent on structural connections of the load cell to the tensioner and to the skid on which tensioners are mounted. These structural connections can be affected by ground motion from adjacent events and by transportation loads that occur when the skids are moved from one location to another.

Our modal tests on several tensioners revealed that any changes in the structural integrity of the load cell could be directly correlated to a specific resonant frequency (a nominal

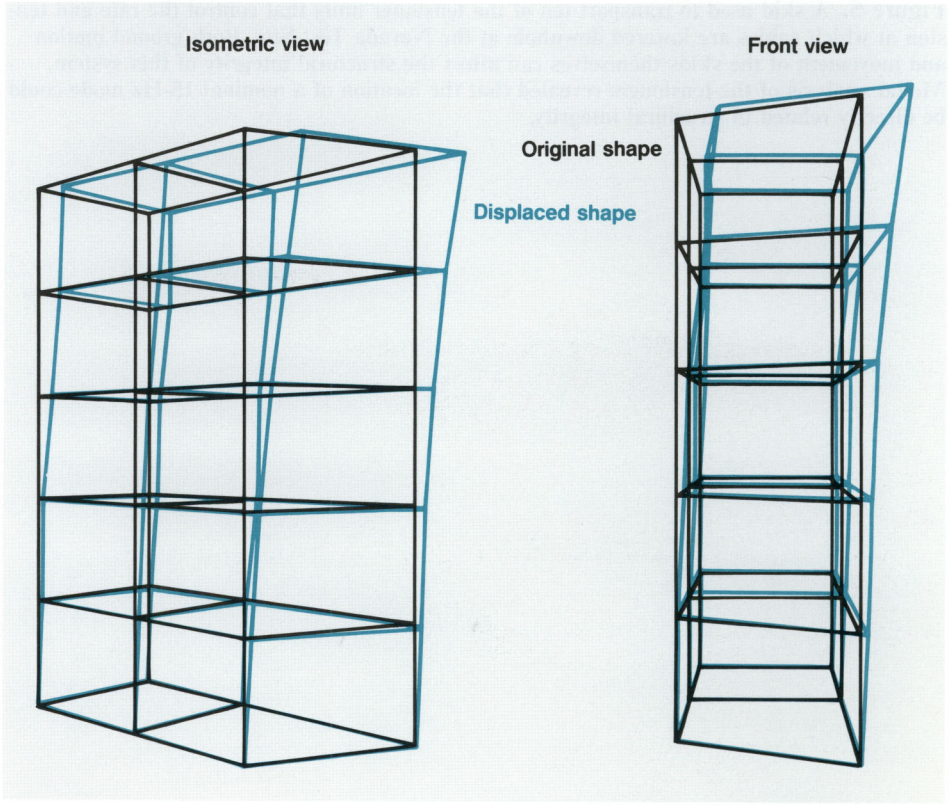

Figure 4. When a structure is excited by a sinusoidal forcing function with a frequency equal to one of its resonant frequencies, it vibrates with a particular spatial shape. One of the results of processing data from modal analysis is animation of the structure's mode shape. The first mode of this Nova tower was at 5.6 Hz, and the tower took on the shapes shown here: original shape (black) and displaced shape (blue).

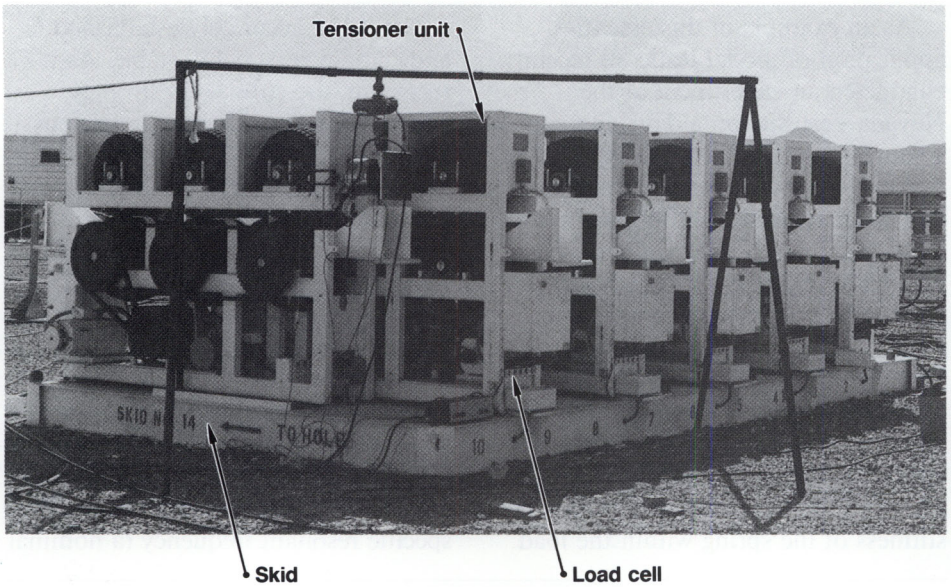

Figure 5. A skid used to transport ten of the tensioner units that control the rate and tension at which cables are lowered downhole at the Nevada Test Site. Both ground motion and movement of the skids themselves can affect the structural integrity of this system. Modal analysis of the tensioners revealed that the location of a nominal 15-Hz mode could be directly related to structural integrity.

15-Hz mode) of the load cell-tensioner-skid structure. Our recommendation was simply to monitor this resonant frequency, an easy task, to ensure the integrity of the critical load cell and its associated system.

Continuing Research

From a structural point of view, the more we know about the dynamic characteristics of a given structure, the more confidence we can place in the integrity and behavior of that structure in its operating mode. Our continuing research involves testing a variety of structures, including microwave towers, cranes, and transportation and shock-mitigation systems. In the future, we plan to update and modify our data-collection methods and processing codes.

Key Words: dynamic testing; finite-element analysis; modal analysis; resonance.

Microtechnology for Research Diagnostics

Microfabrication techniques developed at LLNL extend commercial semiconductor technology to create components, such as free-standing, silicon-nitride membranes, for unique diagnostic systems.

For further information contact Joseph W. Balch (415) 422-8643, Dino R. Ciarlo (415) 422-8872, or Glen M. McWright (415) 423-6768.

Semiconductor technology has had as large an impact on LLNL research as it has on commerce and industry, and we rely increasingly on microtechnology to improve the speed and accuracy of our diagnostic instruments. Building on the technology originated in the commercial semiconductor industry, we conduct state-of-the-art investigations in several areas of semiconductor theory and technology.

This research, known collectively as diagnostics and microelectronics engineering (DME), has diverse applications throughout the Laboratory. However, all DME work relies on the same set of fabrication processes: microphotolithography; chemical and plasma etching of semiconductors; techniques for depositing thin films on metals (aluminum, gold, platinum, and titanium) and dielectrics (silicon nitride and silicon dioxide); and ion implantation to dope materials with electrically active impurity ions.

The goal of DME is to develop new microstructures (i.e., structures with dimensions in the micrometre and submicrometre ranges) that are crucial to present and future Laboratory programs. For this purpose, DME investigates new concepts for diagnostic instruments and components, and develops application-specific, solid-state components of several different types. These components are widely used in research throughout the Laboratory (see Table 1).

The most mature and broadly applied areas of this technology are in microelectronics, where semiconductor research at LLNL began (as it did in industry). These traditional areas of research include

- High-speed switches in the high voltage ranges (1 to 100 kV).
- High-speed integrated circuits.
- Radiation detectors for all energy ranges from low (electromagnetic radiation) to high (gamma rays).

In recent years the technology has grown to include

- Techniques of fabricating thin films for semiconductors and other types of passive microstructures.
- Techniques of combining optical with electronic effects.

The Laboratory deals with all these new areas as needs for improved diagnostic components dictate.

High-Voltage Switches

Fast electrical-switching systems have many applications in diagnostics for high-energy physics; some of the more important of these applications at LLNL are: streak cameras, microchannel plates, electric detonators, Pockels cells (laser beam modulators), and optical pulse-shaping systems. In several of these high-speed, high-current applications, solid-state switches offer advantages over more conventional high-power switches (based on vacuum tube or gaseous-discharge technologies), even though they are limited in maximum breakdown voltage. They tend to be more reliable, they are simpler and more economical, and they have less jitter in applications that require very-high-speed triggering. DME researchers have been investigating a number of electrically and optically triggered solid-state devices, from which two prime candidates for LLNL applications have emerged: electrically triggered high-voltage avalanche transistors and *p-n* diodes; and optically triggered photoconductive switches.

Most of the electrically triggered devices take advantage of fast avalanche-breakdown mechanisms that can occur in reverse-biased *p-n* diodes. The devices have switching times ranging from less than 100 ps to several nanoseconds, depending on their structure and mode of operation. Our DME researchers have developed a variety of electrically triggered devices capable of switching 1000 to 3000 V in approximately 100 ps.

Optically triggered devices rely on the generation of electron-hole pairs initiated by absorption of photons. Such photoconductive devices generally have a simpler structure than do electrically triggered

p-n–junction devices and consequently tend to operate at higher voltages and switching speeds; however, they require a laser of relatively high power to initiate their switching action. A notable application of optically triggered switches developed at LLNL is a 10 000-V, silicon-based switch used in the Nova laser as part of its optical pulse-shaping electro-optic system. In this application, the device turns on in approximately 300 ps.

High-Speed Integrated Circuits

Research and development of very-high-speed integrated circuits for diagnostic measurements is a significant and continuing part of our DME work. At present, DME is supporting two semiconductor technologies for high-speed integrated-circuit development. For applications requiring moderate speed (e.g., 100 MHz), DME uses complementary, metal-oxide-semiconductor (CMOS) gate arrays to develop semi-custom integrated circuits. For higher speed applications (1 to 5 GHz), DME engineers build full custom integrated circuits based on gallium-arsenide semiconductors.

In developing CMOS gate-array integrated circuits, DME specialists work with other LLNL engineers who have specific progammatic applications in mind. DME makes available to other engineers a full set of modern computer tools for aiding in the design of application-specific circuits on a standard gate array. After the circuit design is reviewed by DME engineers, the DME staff fabricates and tests the circuit. Recent uses of this new technology at LLNL include controller circuits for charge-coupled-device diagnostic cameras and digital encoding circuits for diagnostic data transmission. The base for this semi-custom technology is a very large chip with 2700 gates and 124 input/output pads. Built with 1.25-μm gates on a sapphire substrate, it routinely operates with system clocks above 50 MHz and has been operated in selected designs at frequencies greater than 200 MHz. Computer-aided engineering and manufacturing tools available for engineers' use include schematic-capture workstations, logic simulators, and test-program simulators. The DME staff also uses computers in fabricating designs; these computer tools include software that entirely automates the placing and routing of the art work on a custom photomask, and software and hardware for automatic testing of the completed circuits.

For higher speed circuit applications, DME engineers develop small- to medium-scale integrated circuits of gallium arsenide, a newer alternative to silicon as a semiconductor. For high-speed applications at LLNL, this direct-band semiconductor has several advantages over silicon: a higher energy-band gap, which permits operation in higher temperature environments; compatibility with insulating substrates, which greatly reduces parasitic capacitances and thereby leads to higher operating speeds; higher electron mobility and therefore faster operating speeds; and an energy-band structure that allows effective lasing action (optical emissions).

The generation of gallium-arsenide integrated circuits now in development have both analog and digital logic functions with

Table 1 Microfabrication technology finds application throughout the Laboratory. Here are listed several LLNL research areas and the microfabrication products they use.

Research area	High-voltage switches	Very fast microelectronics	Radiation detectors	Passive microstructures	Integrated optics
Nuclear weapons research	■			■	
X-ray laser research	■	■		■	
Laser Program	■	■	■	■	■
Nuclear tests	■	■	■	■	■
Electromagnetic field generation		■		■	
S-1 (supercomputer) research		■			

propagation delays below 100 ps. Various designs of such circuits can function in several ways: as electrically triggered sample-and-hold circuits faster than 2×10^9 samples per second; as pulse amplifiers with bandwidths greater than 1 GHz; as circuits that protect other circuits from the effects of electromagnetic pulses up to 400 V; or as optical detectors and voltage-pulse generators with rise times below 10 ps.

Radiation Detectors

Detectors are widely used around the Laboratory to measure radiation ranging from the low-energy, electromagnetic portion of the spectrum to high-energy gamma rays. In experiments with pulsed power, a magnetic field sensor known as a B-dot probe (after the time-dependent magnetic field vector of Maxwell's equation) is widely used for detecting intense magnetic fields. The probe, with dimensions measured in millimetres, typically consists of magnetic induction loops connected to miniature coaxial cables. Using adaptations of integrated-circuit technology, we have developed a family of miniature B-dot probes with diameters ranging from 100 to 500 μm. These microsensors generally have a bandwidth greater than 1 GHz, and, because their small physical size does not disturb the magnetic field being measured, they respond faster than conventional models do.

For use in the Laboratory's nuclear tests and laser research, DME is developing photoconductive detectors of x rays and gamma rays. Based on gallium arsenide and other semiconductors from classes III through V of the atomic table, these detectors have shown promising results with picosecond response speeds and virtually equal sensitivity to x rays over broad energy levels.

Passive Microstructures

Passive microstructures are miniature devices having dimensions of a few micrometres or less. They are passive in that they are not used to process electrical signals. The key material-processing technologies we use to make passive microstructures are photolithography, chemical-vapor deposition, anisotropic-chemical etching, and reactive-ion etching. These processes are adapted from ones used in the integrated-circuit industry. DME has also investigated the etching properties of 110-oriented silicon.[1] These investigations with silicon have led to the development of various components, including multilayered x-ray-diffraction gratings for use in x-ray spectrometers, and targets used in physics experiments with x-ray lasers.

Free-standing Membranes

Recent Laboratory applications of LLNL-developed microstructures include thin membranes of free-standing silicon nitride for use as x-ray windows in low-energy x-ray experiments, as x-ray filters, as substrates for synthetic multilayers used to reflect x rays, and also as targets for high-energy electron experiments in which x rays are generated. Each of these applications requires a large (1 cm^2), flat membrane that readily transmits x rays in the range of interest, typically 100 to 1000 eV. The membrane must also be free standing (except for the frame that supports it) and have sufficient tensile stress so that it is taut but not ruptured.

Several of the materials used to fabricate integrated circuits can be used for such membranes. Three of the most common are single-crystal silicon, silicon nitride, and boron nitride. They can be deposited on a silicon wafer by either plasma-enhanced or low-pressure chemical-vapor deposition (CVD); these materials remain as a membrane when the substrate is etched away.

Another material commonly used in fabricating integrated circuits is thermally grown silicon dioxide. However, it cannot be used as a free-standing membrane because it is grown with compressive rather than tensile stress, and therefore it fractures very easily.

Young's modulus—the ratio of stress to strain tension—is an important parameter in selecting the material to be used for the membrane. A low value of Young's modulus is preferred so that, for a given strain on the membrane, the resulting stress will not be excessive. By this criterion, boron nitride is the preferred material.

To meet the requirement of high x-ray transmissivity, the material must have a low absorption coefficient to the energies of interest. For x-ray energies below 400 eV, boron nitride is preferred because it has a lower absorption coefficient than either silicon or silicon nitride. Silicon has a slight advantage over boron nitride for x-ray energies greater than 400 eV and less than 2 keV.

Most free-standing membranes are produced by the following method: first, both sides of a silicon wafer are coated with the chosen membrane material, then on one surface the shape of the desired membrane is printed lithographically. The membrane material inside the printed shape is then removed by plasma etching to reveal the corresponding area of the silicon substrate. This area of the substrate is next removed with a wet chemical etchant, such as potassium hydroxide. The etchant has a near-zero etch rate for membrane materials and therefore leaves the remaining membrane free standing, its perimeter supported by a frame of the remaining substrate.

Membranes of single-crystal silicon are fabricated by a different method, which relies on the facts that boron can be thermally diffused into silicon and that silicon thus treated is highly resistant to chemical etchants. If the silicon is "doped" with boron to the extent that about 1% of the silicon atoms are replaced with boron atoms, chemical etching of the silicon wafer is slowed to near zero. Therefore, controlling the depth of the boron infusion into the surface of the silicon wafer also controls the thickness of the silicon membrane that is left after chemical etching. Figure 1 shows part of a silicon wafer containing several membranes of boron-doped silicon. Each membrane is 2.5 μm thick and has a width and length of 3 × 4 mm. This technique can be used to create single-crystal membranes ranging in thickness probably from 50 nm to 10 μm.

Figure 2 is a photograph of two boron-nitride membranes, each 180 nm thick and supported on a 200-μm-thick silicon frame. These membranes were designed for use in a stacked array in a vacuum chamber. Such stacks of membranes are used in transition radiation experiments; a stack of membranes is bombarded from one side with high energy electrons, causing x rays to emerge from the other side. Boron nitride is a stable material with a low absorption coefficient for x rays. It is vapor deposited at low-pressure by reacting diborane (B_2H_6) and ammonia (NH_3) at a temperature of 400°C and pressure of 400 mPa. Thin membranes of boron nitride are also used in photomasks for x-ray lithography equipment.

Recently, DME has been developing a process that allows control of the tensile stress in thin membranes of silicon nitride. This process involves adjusting the flow-rate ratio between two gases, dichlorosilane (SiH_2Cl_2) and ammonia (NH_3), in a low-pressure CVD reactor. By varying this flow-rate ratio between 1:3 and 7:1 and by varying the deposition temperature from 800°C to 930°C, the membrane stress can be changed from a high tensile value of 1 × 10^5 N/cm^2 to the opposite extreme, compression. Figure 3 shows contrasting photographs of free-standing silicon-nitride membranes in tension and in compression. This freedom to vary the membrane stress has proven to be very useful in a number of experiments.

These developments illustrate the accuracy with which we can fabricate microstructures of various types. This degree of accuracy (and more) is required to meet the Laboratory's specialized and diverse requirements for diagnostic devices.

Optoelectronics

Optoelectronics, DME's newest area of research, combines the capabilities of microelectronics and micro-optics to produce a technology capable of acquiring and processing

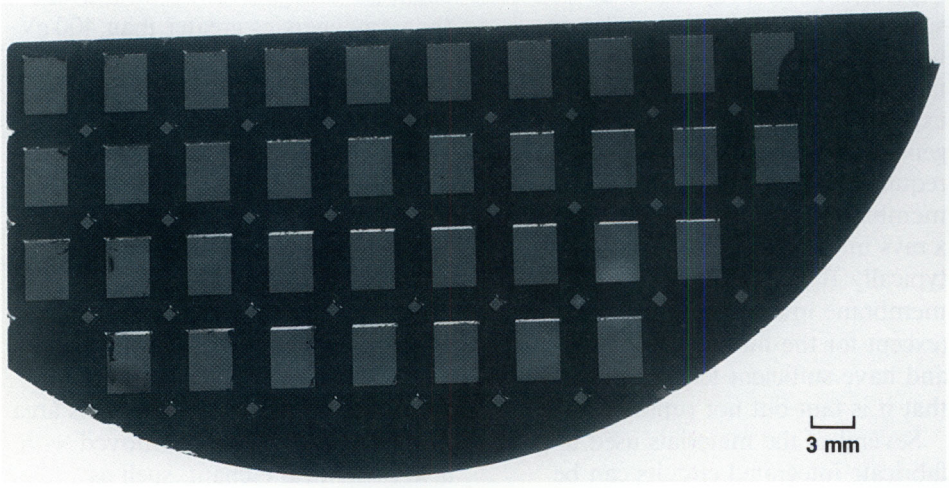

Figure 1. Part of a silicon wafer containing several membranes, each 3 × 4 mm and 2.5 μm thick. The membranes were fabricated in the silicon substrate itself by "doping" chosen areas of the substrate with an infusion of boron on one side of the wafer and then removing the silicon from the other side.

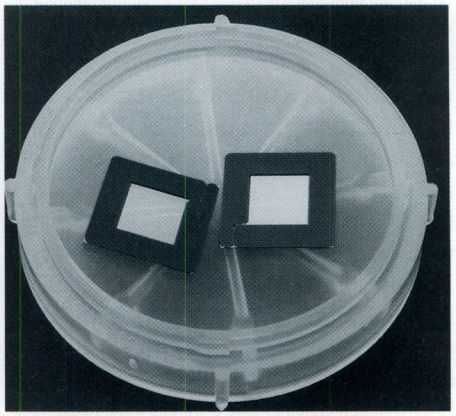

Figure 2. Two boron-nitride membranes, 7 × 7 mm and 180 nm thick, each supported on a 200-μm-thick silicon frame. Boron nitride is deposited by reacting diborane and ammonia gases in a low-pressure chemical-vapor deposition system at 400°C. These frames have a corner aperture to allow evacuation because they are to be stacked for use in a vacuum chamber.

data at extremely high speeds. Our main efforts now are to develop integrated optics and solid state injection lasers.

Integrated Optical Devices

Integrated optical devices, which use light beams for the efficient transfer of information, are the heart of optical communication networks. In these networks, conventional wire and radio links are replaced by thin, light-guiding optical fibers, and the light signal is manipulated and controlled by integrated optical devices—the optical equivalent of integrated electrical circuits. Recent advances in integrated optics have made it possible for almost all optical signal-processing functions to be performed on a single chip. Such an optical system offers exciting advantages over more conventional technologies: wide bandwidth, small size and weight, and immunity from the electromagnetic interference that can damage transmissions by conventional means.

Although the integrated optical devices we use are similar to those used in the telecommunications industry, our applications and requirements are unique. One of our applications, for example, requires the transmission of a single analog signal from a remote sensor. Electrical-cable-based diagnostic systems, being lossy and dispersive, are limited to bandwidths less than 1 GHz. To circumvent this limitation, we have used the high bandwidth capabilities of a "photonics" diagnostic system: we can, for example, directly drive (or modulate) a laser diode with an electrical pulse, send the information over an optical fiber, and record the light on a streak camera. However, even this simple photonics system is satisfactory only for bandwidths less than 3 GHz. For higher bandwidth applications (up to 10 GHz), the solution is to modulate a laser diode externally with an integrated optical device.

Most of the research in optical-fiber telecommunications has focused on devices that operate at a wavelength of 1300 nm because the transmitted light in optical fibers attenuates least at this wavelength. Unfortunately, this wavelength is outside the sensitivity range of the streak cameras used at LLNL to record transient events. Furthermore, research on these devices has emphasized high data-transmission rates (as required by the telecommunications industry) rather than single-event analog modulation. We set out to develop an electro-optic modulator operating at 810 nm (a wavelength more suitable for streak camera operation) and to construct a device capable of high-speed, single-event analog modulation.

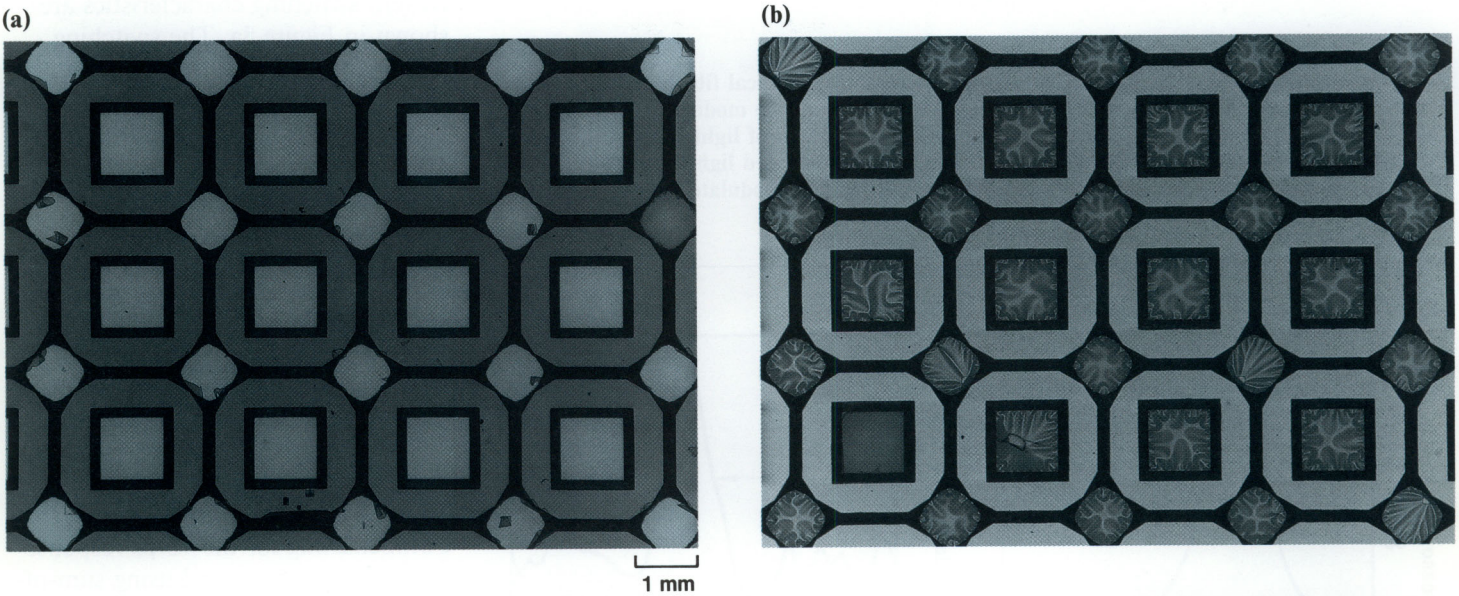

Figure 3. Free-standing silicon-nitride membranes, each approximately 1 × 1 mm and 120 nm thick, deposited by reacting dichlorosilane and ammonia gases in a low-pressure chemical-vapor deposition reactor at about 800°C. The membranes in photo (a) are under tension while those in (b) are compressed. The differences were produced by varying the temperature and the ratios between the gas-flow rates during fabrication.

We designed a traveling-wave, directional-coupler modulator and fabricated it in lithium niobate. As Figure 4 shows, the design brings two waveguides, formed by the diffusion of titanium into a lithium-niobate substrate, into close proximity. Because the evanescent field tails in the waveguides overlap, light couples between the waveguide channels with an efficiency that depends on various waveguide parameters. For an appropriate design, all of the light entering one of channels couples to the other channel. By applying an electrical signal to the lithium niobate, we electro-optically induce a refractive-index difference between the two waveguides, alter the crossover efficiency, and thus modulate the light.

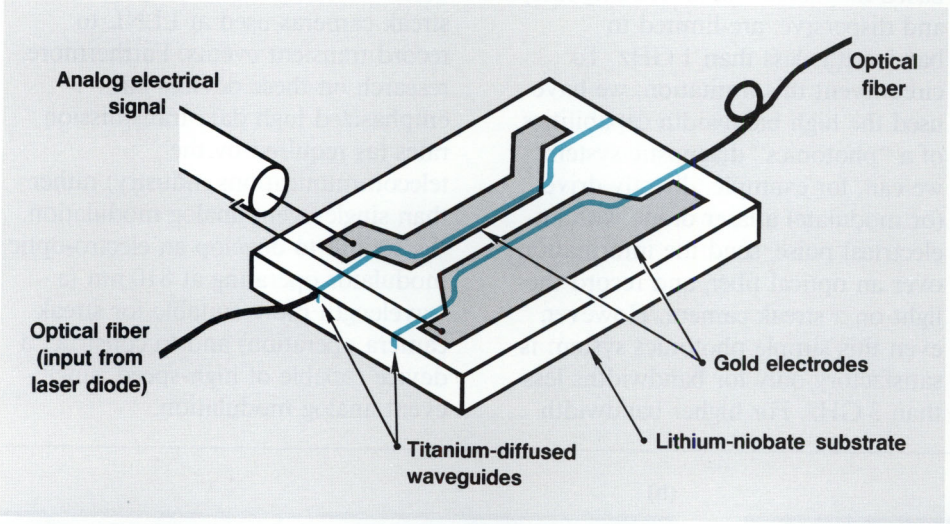

Figure 4. Directional-coupler, traveling-wave modulator with optical fibers attached. An unmodulated light beam is applied to one optical waveguide of the modulator via the input optical fiber. The applied electrical signal modulates the amount of light coupled to the second optical waveguide of the directional coupler. This modulated light beam is removed from the modulator via an output optical fiber. This device can modulate optical signals in 35 ps.

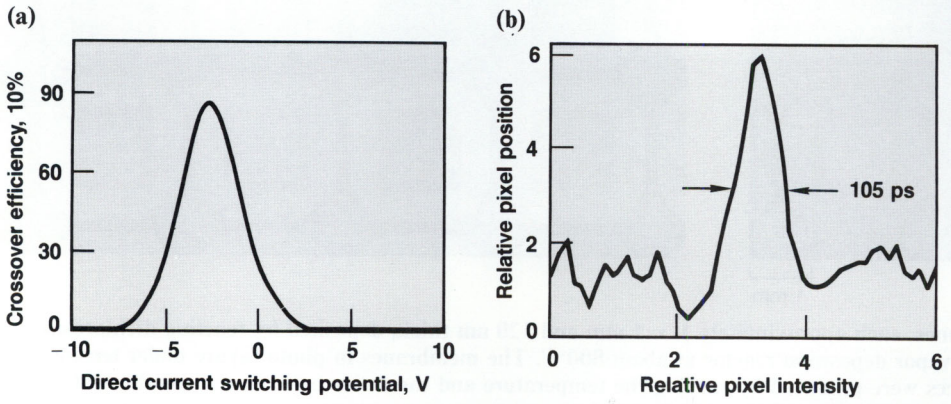

Figure 5. Measured characteristics of the directional-coupler modulator illustrated in Figure 4. (a) Direct-current switching characteristics, and (b) temporal characteristics, measured by a streak camera.

When designing the device, we used a computer to evaluate critical parameters, including waveguide geometry, electrode design, and the optical-fiber coupling. We validated these parameters experimentally as well. Several directional coupler-modulators have now been successfully fabricated, and our preliminary electro-optic measurements indicate that the fastest has a switching potential of only 5 V at a speed of 35 ps. This switching speed translates into a bandwidth of 14 GHz, better than the 10 GHz we had anticipated.

We fabricated the device by first diffusing strips of titanium into lithium niobate at 1025°C for 5 hr to form optical waveguides. Gold electrodes were then electroplated to a height of 3 μm, and the device was carefully packaged to ensure good high-frequency characteristics. The modulator was evaluated with a laser operating at 810 nm; the direct-current switching characteristics are shown in Figure 5a. The switching potential is 5 V, and the extinction ratio (ratio of maximum to minimum light transmission) is better than 15 dB.

The temporal characteristics were measured by driving the modulator with a single electric pulse. The drive pulse has a peak amplitude of 4.5 V and a width at half maximum of 70 ps. The modulator was first dc-biased to null the "straight-through" state, then driven with the single 4.5-V, 70-ps pulse. The resulting streak camera trace is shown in Figure 5b; its width is 105 ps. Compensating for the 70-ps response time of the camera and using sum-of-the-squares broadening, we calculate a modulator impulse response of 35 ps. These preliminary results imply a very fast device. The modulator

should perform well in the remote measurement of high-speed, transient signals.

Our future plans in the area of optoelectronics include integration of the optical modulator with the laser diode source on a substrate of gallium arsenide (which is capable of laser light generation) and the fabrication of large modulator arrays. Such an array constitutes an entire diagnostic system on a single chip—a considerable improvement in speed, cost, and size over present technologies.

Facilities

Our research on semiconductor technology is done in several on-site facilities. The largest is the Microfabrication Facility, a laboratory well equipped for producing micron-sized structures. In this laboratory, we can do thermal diffusion and oxidation, ion implantation, reactive ion etching, and chemical-vapor deposition of various types of thin film.

For producing microstructures, the key technology is photolithography. The Microfabrication Facility has three photolithography rooms. The newest, shown in Figure 6, is a carefully controlled environment; it includes a special air-filtering system for removing fine particulate contaminants. It houses, among other things, two machines capable of submicron lithography: a direct-step-on-wafer mask aligner and a modern contact mask aligner.

The Microfabrication Facility will soon have a molecular-beam epitaxy machine for growing epitaxial layers of class III through V elements and other semiconductor thin films. With this machine, it will be possible to grow *p-n* heterojunctions and multiquantum-well superlattices. These structures are needed for faster microelectronics, injection lasers, and other optoelectronic devices; and for microstructures used in x-ray optics.

Besides microfabrication laboratories, the facility includes extensive electronic and optical testing laboratories. In recent years we have acquired such advanced equipment as a picosecond laser for research into fast photoconductive effects in semiconductors and a tunable dye laser (in which the dye solution is the lasing medium and is tunable to different wavelengths of light) for research on lithium-niobate integrated optics. In addition, we are now acquiring optical diagnostic equipment for characterizing injection lasers.

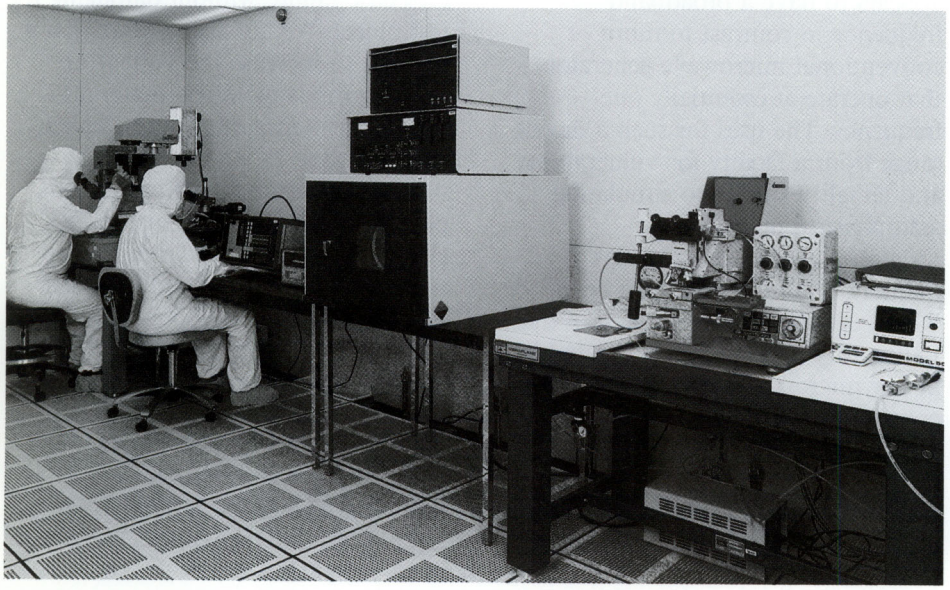

Figure 6. New class-10 clean room, located in the Microfabrication Facility, is used for critical photolithography operations. The operator at the extreme left is working with a direct-step-in-wafer mask aligner, used to print patterns on photoresist-covered wafers. This projection instrument can print lines as narrow as 0.8 μm. At the right of the photograph is a second mask aligner that prints by direct contact. This instrument has a short-wavelength ultraviolet lamp for printing lines as narrow as 0.5 μm. Between the two mask aligners is a plasma etcher used for stripping photoresist from processed wafers.

Future Directions

Our DME research is advancing in several different fields—microelectronics, injection lasers, and electro-optic functions—and we expect soon to see further developments in these individual areas. In the longer range, however, some of these disciplines will merge and focus much of their attention on the newer semiconductor, gallium arsenide.

Key Words: gallium arsendie; high-voltage switches; integrated circuit fabrication; integrated optics; optoelectronics; radiation detectors; semiconductor thin films.

Notes and References

1. The silicon is oriented to the 110 plane, as defined by the Miller indices of crystalline structure.

High-Power Microwaves and Pulsed Power

A broad-based program of research is being conducted at LLNL for improving our ability to generate high-power microwaves and high-power electron beams, extending electrical switching into new high-power domains, improving the electrical performance of dielectric materials, and studying electromagnetic coupling phenomena as they relate to weapons vulnerability.

For further information contact
W. Wayne Hofer (415) 422-1636,
Scott C. Burkhart (415) 423-2061,
Donald J. Meeker (415) 422-5434,
Marco S. Di Capua (415) 422-9698,
or Ray J. King (415) 423-2369.

Our efforts to develop the technology of high-power microwaves and pulsed power will benefit many areas of Laboratory research: weapons design, laser-driven inertial-confinement fusion, laser separation of isotopes, and free-electron lasers. Our five major projects in this area involve high-power microwaves, high-power electron beams, high-power switching, dielectric materials, and electromagnetic coupling phenomena. We have developed a variety of unique research facilities, including a well-equipped pulsed-power laboratory, a microwave engineering laboratory, a broadband-microwave standard-field range (the EMPEROR facility), and a high-power-microwave range for mapping radiation patterns (the anechoic chamber facility).

High-power microwaves have been used extensively for auxiliary heating of plasmas in magnetic fusion experiments and for studying electromagnetic coupling phenomena as they relate to the effects of high-level microwaves on weapon systems. Future applications may include microwave weapons. We have developed a virtual-cathode oscillator (a "vircator") as a source of high-power microwaves. The vircator may have an important role in high-power-microwave coupling studies and in microwave weapons.

We are also conducting research on a new method of generating high-power microwaves, namely the interaction of an electron beam with a background plasma. We are especially interested in this method of microwave production since it appears to have a broadband frequency in contrast to more conventional microwave generators that operate at essentially one frequency. The uses for such a device range from a facility for vulnerability and lethality studies to simulating astrophysical phenomena.

High-power electron beams (namely, relativistic electron beams or REBs) are required by several of the Laboratory programs to generate high-power microwaves and to generate energetic x rays as well as to study the physics of various electron/material interactions. We conduct our research on a 2-MV, 0.4-TW electron-beam accelerator that we redesigned and installed.

High-power switching is at the core of nearly all pulsed-power technologies. Our current efforts are twofold: developing an advanced high-charge (>500 C), high-current (~1 MA) switch-test capability, and developing laser-triggered solid-state switching with a high repetition rate (~5 kHz) and high average power (~10 kW) in silicon and gallium arsenide. We are also researching the subnanosecond, high-power switching capability of gallium arsenide.

The voltage hold-off capability of dielectric materials ultimately limits the maximum voltage and power in most pulsed-power applications. In collaboration with the Massachusetts Institute of Technology and Texas Tech University, we are increasing our ability to detect potential dielectric failure without damaging the test object. We are also working on a method to increase the voltage at which various dielectric materials flash over their surface when under vacuum.

High-power-microwave weapons pose a serious threat to susceptible electronic components in military systems. We designed and built the EMPEROR and anechoic-chamber facilities to study electromagnetic coupling phenomena associated with high-power microwaves. Our work addresses the issue of "backdoor coupling," the penetration of microwaves into the interior of an aircraft, for instance, through crevices in its metal skin.

Two of our research projects, the generation of high-power microwaves and electromagnetic coupling phenomena, are discussed in more

detail below, as are the EMPEROR research facility and the anechoic chamber.

Generation of Microwaves With a Virtual-Cathode Oscillator

We are generating high-power microwaves with a vircator driven by a relativistic-electron-beam generator. Rapid technology advances in high-voltage, high-current REBs have made it possible to investigate this and related microwave sources.

The vircator, a fairly new device, was first proposed by D. Sullivan in 1979.[1] It has been the subject of serious research at the Laboratory for the past five years. Using our vircator, we recently generated a record burst of microwave power: >4 GW for 25 ns at ~7 GHz. This compares with the output of an earlier microwave source, the relativistic magnetron, which produced 4.5 GW at the significantly lower frequency of ~3 GHz.

Design and Operation

The vircator differs from other microwave-generating tubes in two major respects:

- It has neither a resonant structure (as does the magnetron) nor a long wave/beam interaction region (as do traveling-wave tubes or free-electron lasers).
- It operates well above the space-charge-limiting current.

The latter is the basic operating principle of the vircator. The limiting current occurs in an electron-beam device when the beam of traveling electrons becomes so dense that new electrons entering the beam are stopped by the collective space charge. This effect limits the maximum beam current of most beam-driven microwave sources. However, the unique operating feature of the vircator is that it only begins to operate after the limiting current has been exceeded. The collective space charge behaves as a virtual cathode, reflecting the electrons back toward the real cathode. In doing so, the vircator generates reflected bursts of electron current in excess of the incident, or forward, cathode current. This reflecting or reflexing of electrons generates microwaves. The vircator is shown schematically in Figure 1.

Diagnostics

We have also developed specialized diagnostics that measure the power, frequency, and modal content of microwaves. In diagnosing microwaves, the most critical link is to couple a sample of the high-power microwaves into a standard waveguide and coaxial cable where it can be measured. To make this link, we designed and built electric-field probes (E-probes) and various transverse magnetic (TM) mode-selective couplers, particularly for measuring TM_{01} and TM_{02} modes.

The E-probe has a broadband response and is used to sample the radial electric field at the waveguide wall, which can consist of many modes. The coupling factor has been determined by computer modeling and by laboratory measurements.

The power in a single waveguide mode can be measured with TM-mode-selective couplers. These couplers are designed on a computer with codes written for this project. Unlike the E-probe, they are difficult and expensive to fabricate. In order to calibrate them, we also have had to develop several types of mode generators.

The vircator is, by definition, a high-power, short-pulse device, with extremely fast pulse-rise times and with microwave output rarely exceeding 100-ns duration. Much of the fine structure of the output occurs in the nanosecond time frame. The application of extremely short-pulse microwave techniques became necessary to properly calibrate the diagnostics. Using a mixer driven by a microwave source and gated by a fast pulser, we were able to generate microwave bursts as short as 1 ns. These short bursts were used for measuring reflections due to discontinuities in the diagnostics, microwave-detector response time, and delay times of filters. Conversion from one TM mode to another in the waveguide could also be detected.

Computer Simulations

We used CONDOR, a two-dimensional, relativistic, particle-in-a-cell code that runs on the Cray computers, to simulate vircator operation. CONDOR advances electrons through the problem space, applying the electromagnetic forces that exist on the particles at each time step. The code operates in a two-dimensional physical space with a three-dimensional momentum space. Figure 1b is a plot of electron positions in the problem space for a 1.25-cm cathode-anode gap and a 1.8-MV drive voltage. We have also simulated the electric-field strength at the waveguide wall.

Experiments

With the apparatus diagrammed in Figure 1a, we have performed a series of experiments. So far, only the E-probes and TM_{01} couplers have been used to measure the microwave

output. Figure 2 compares measurements of microwave power by the TM_{01}-mode selective coupler and by the E-probe for a 2-cm cathode-anode gap and a 1.8-MV cathode voltage. The two measurements of power level agree up to 4 GW at 6.5 GHz, after which the power measured by the TM_{01} coupler decreases. Above 6.2 GHz, the increased power level measured by the E-probe is most likely sustained by higher modes (notably the TM_{02} mode), which the TM_{01}-mode coupler cannot measure.

A cathode-anode gap of 1.25 cm was tried for comparison with computer simulations. The initial frequency measurements showed a strong oscillation at 9.5 GHz, which is very close to the computer prediction of 9 GHz. However, the output power was much lower than predicted, an outcome attributable mainly to a lower-than-expected cathode voltage provided by the REB generator.

Future Work

We plan to improve the diagnostics to better resolve the power, frequency, and modal content of the microwaves. We will use a calorimeter to measure the total microwave energy for comparison to the integral of the power measured by the E-probes and TM couplers. We will then try

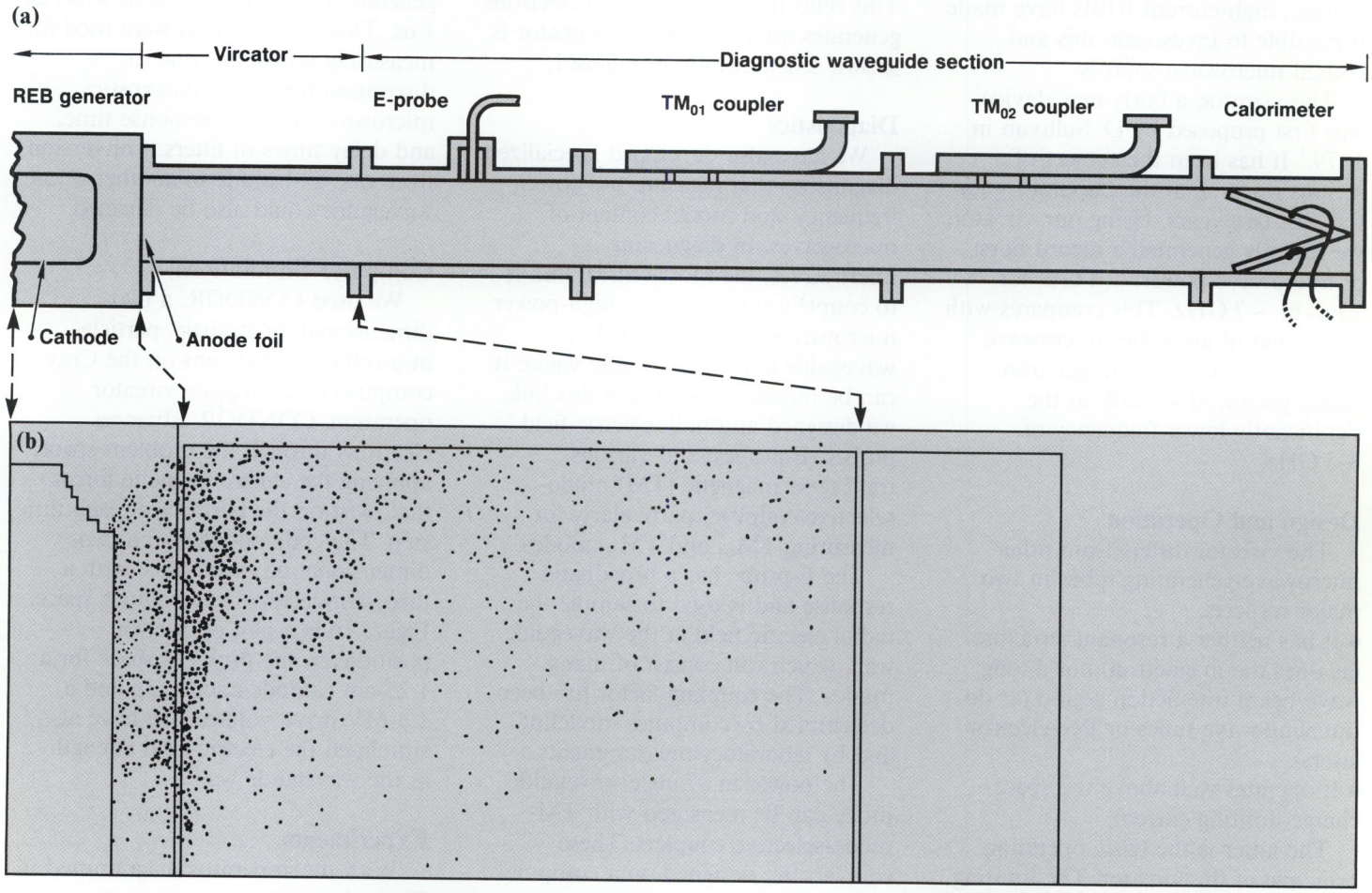

Figure 1. (a) Cross section of vircator and diagnostics waveguide section. The vircator is driven by an REB generator. Emitted electrons traverse the anode foil, forming a potential minimum in the waveguide. The extreme repulsive force of the collective space charge behaves as a virtual cathode by reflecting the electrons, which form into bunches and pass back through the anode foil toward the real cathode. The reflected electrons generate bursts of current in excess of the incident, or forward, cathode current. The frequency of the bunch reflex oscillations has been observed in computer simulations at the same frequency as the generated microwaves. (b) Plot of electron positions within the computer simulation space for a 1.25-cm cathode-anode gap and a 1.8-MV drive voltage.

different cathode and anode designs to improve the vircator's efficiency and spectral purity.

Generation of Microwaves from Electron-Beam/Plasma Interaction

High-frequency (1 to 100 GHz), broadband, high-power (hundreds of megawatts) microwaves can be generated when an REB is injected into a low-density plasma. We are beginning the third year of a three-year research project to investigate this process with the objective of scaling and optimizing the microwave output to very high power and efficiency. This method of microwave generation is especially interesting because it appears to have a broadband frequency, whereas other microwave generators operate at one frequency. Devices of this type could be used, for example, to generate radiation fields for lethality/vulnerability studies or to simulate astrophysical phenomena.

Our work on the project was prompted by initial observations of a group under Gregory Benford at the University of California (UC) Irvine.[2] Benford's group injected a 1-MeV, 90-kA electron beam into a plasma and observed microwave power emitted at frequencies from a few gigahertz (the plasma frequency)[3] to frequencies in excess of 100 GHz, the limit of their instruments.

The current project, a joint effort of LLNL and UC Davis is organized along the following lines:

- Theory: LLNL plasma theorists are working with researchers at the Department of Applied Science at UC Davis to develop the dynamics of beam/plasma interaction.
- Experiment: LLNL researchers in the area of high-power microwaves and pulsed power perform the experiments, using the Laboratory's 2-MeV accelerator and a plasma source developed at UC Davis.
- Simulation: LLNL engineers perform two-dimensional particle-in-cell code simulations, and UC Davis researchers map the optimal parameter space with their one-dimensional code.

The objectives of our present work are to understand how the interaction of a high-power REB with a plasma produces microwaves, and to discover how the level of microwave output correlates with beam and plasma parameters.

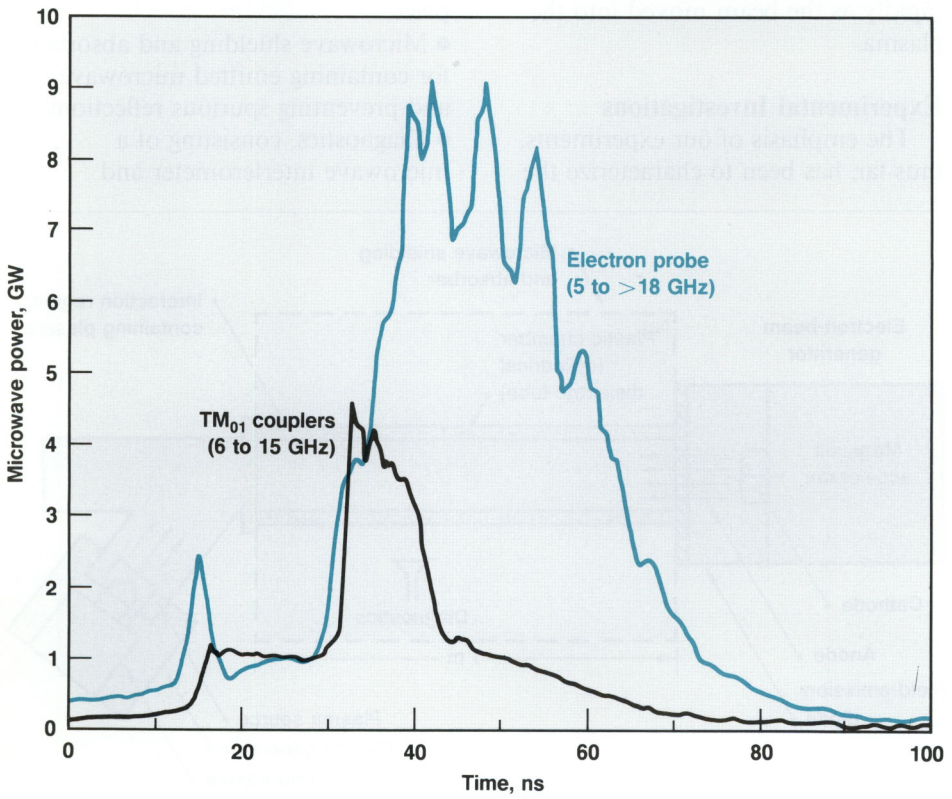

Figure 2. Comparison of microwave power produced by a TM_{01}-mode-selective coupler and the E-probe for a 2-cm cathode-anode gap and a 1.8-MV cathode voltage. The two power levels agree up to 4 GW at 6.5 GHz, after which the power measured by the TM_{01} coupler decreases. Above 6.2 GHz, the increased power level measured by the E-probe is most likely sustained by higher modes (notably the TM_{02} mode), which the TM_{01}-mode coupler cannot measure.

Theoretical Studies

We have developed a linear analytical model of the microwave gain that occurs when an electron beam is injected into a plasma with parameters typical of planned experimental values. The basis of this model is that the electron beam drives a large-amplitude plasma wave that acts as a longitudinal "wiggler," periodically accelerating the beam electrons so that they radiate microwaves.

Specifically, microwave emission appears to follow from a two-stage

process: first, the relative motion of beam electrons and plasma background electrons creates density-distribution waves (periodic bunching) of the electrons; the waves of very large amplitude ($\leq 10^6$ V/cm) eventually saturate. Then, according to one model of microwave production, these density waves cause the electrons in the primary beam periodically to accelerate and decelerate, and thus to radiate microwaves. Since the density bunching is periodic, the electron bunches radiate collectively and in phase, which results in intense microwave emission (electrostatic Bremsstrahlung).

For parameters of the planned experiments, our theory says that the gain will be very large and, therefore, that the system will operate in the super-radiant mode; i.e., the microwave output will be significant for even one pass of the signal through the plasma. The limitation of the theory is that the predicted microwave output is so large that a linear approach is no longer valid, and, therefore, fully self-consistent calculations will be required.

Our theory, which is very crude at present, predicts that frequencies higher than the plasma frequency are attainable with a high electron-beam energy and are shifted by the square of the electron relativistic factor (γ^2), where

$$\gamma = 1 + (E_{beam}/m_0 c^2)$$

and where E_{beam} = the kinetic energy of beam electrons, m_0 = the rest mass energy of the electron, and c = the speed of light.

The output efficiency in the experiment at UC Irvine was not high. Estimates, summing over all frequencies, indicate that only 0.1% of the incoming beam energy was converted to microwaves. We believe we can improve the efficiency in two ways:

- We first set the ratio of beam density, n_b, to plasma density, n_p, close to one. The radiation intensity of microwaves appears to be a strong function of this ratio as it approaches one.
- Second, we use an electron beam with narrower divergence. The Irvine experiment used a beam with a 30-deg full-angle divergence, which caused the beam density to drop rapidly as the beam moved into the plasma.

Experimental Investigations

The emphasis of our experiments, thus far, has been to characterize the beam and plasma and to measure microwave emission. Our principal diagnostics consist of a microwave interferometer and a multichannel microwave spectrometer.

A schematic of the beam/plasma interaction apparatus we use in our experiments is shown in Figure 3. Its major components are:

- An electron-beam generator (2 MeV, 60 kA), consisting of a megavolt accelerator and field-emission diode, as well as a thin aluminized-plastic anode.
- A cylindrical, plastic, dielectric tube that encloses the plasma and in which the beam/plasma interaction takes place.
- Microwave shielding and absorber for containing emitted microwaves and preventing spurious reflections.
- Diagnostics, consisting of a microwave interferometer and

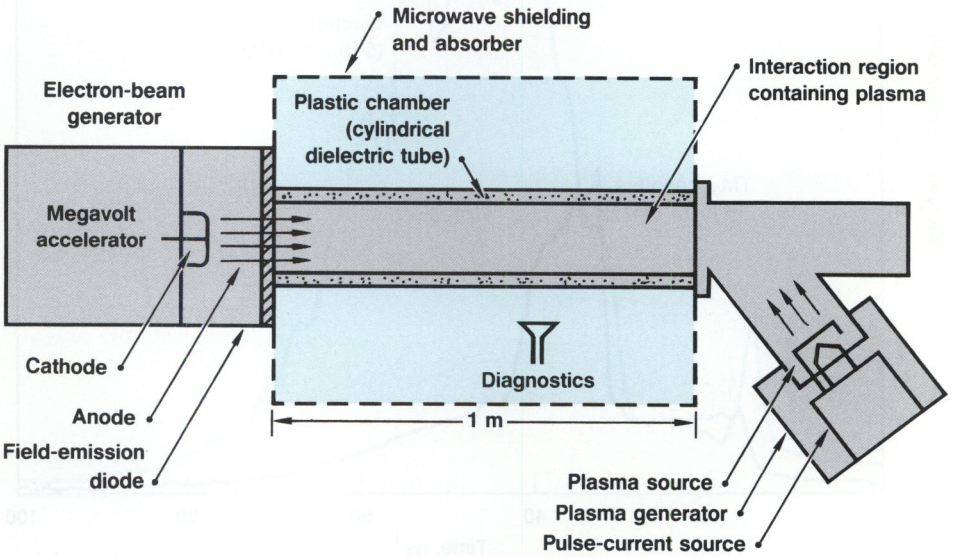

Figure 3. Schematic drawing of the apparatus used for our beam/plasma interaction experiments. The electron-beam generator is at the left. The plasma source is a thermionic lanthanum-hexaboride generator that preforms the background plasma in an 80-mPa argon ambient fill in the dielectric container. Principal diagnostics consist of a microwave interferometer and a multichannel microwave spectrometer. By adjusting beam current and plasma density, we have been able to achieve a beam/plasma density ratio close to unity, which should allow us to optimize the microwave-generating efficiency. We have been able to achieve microwave emission in the frequency range of approximately 2 to 50 GHz.

spectrometer for measuring plasma density and microwave emission, respectively.

- A plasma generator, consisting of a plasma source and a pulse-current (or drive-current) source (50 to 200 A). The plasma source is a thermionic lanthanum-hexaboride generator that preforms the plasma in the plastic chamber.

We characterize the plasma density without the presence of the electron beam by using a 32-GHz microwave interferometer operated in a bridge configuration to detect the phase shift introduced by the plasma electrons. By monitoring the phase difference as a function of time, we can plot the plasma-electron density while the plasma source is on and observe the decay of the electrons after the source is gated off.

A low-divergence beam is a major feature that makes our experiment novel. We take great pains to keep the beam, as it traverses the plasma, parallel to the axis of the plastic chamber. This lack of divergence from the axis forces the beam and plasma to have the longest interaction and, we hope, the highest emission rate.

To measure the beam's divergence, we drilled 1-mm holes, spaced 1-cm apart, through a thick anode, and then measured the injection angle of those electrons that were able to pass through the holes. The holes sample the beam along the radius of the chamber and can be imaged on a fluor and recorded on a streak camera. This measurement indicated that the beam does not pinch and that it is injected relatively straight until very late in the pulse, at which time it blows apart.

We tested beam propagation further by placing current-measuring loops around the plastic chamber (but inside the return-current rods) at different positions along the plasma tube (see Figure 4a). In these tests, we used our "standard" aluminized-polycarbonate-foil anode, and the full beam could enter the tube. Figure 4b shows the four current traces recorded, each representing the net current flowing at that point in the tube and corrected in time for its position. The large current trace ($h = 0$) is that of the accelerator monitor. The plots indicate a delay in net current buildup and a factor-of-two reduction in current magnitude, even 3 cm from the point of injection. As Figure 4b shows, the current does not deteriorate much from the 3-cm point, even 1 m down the tube.

We also measured microwave output power from 2 to 50 GHz in ten discrete frequency bins (see Figure 5). The output from each

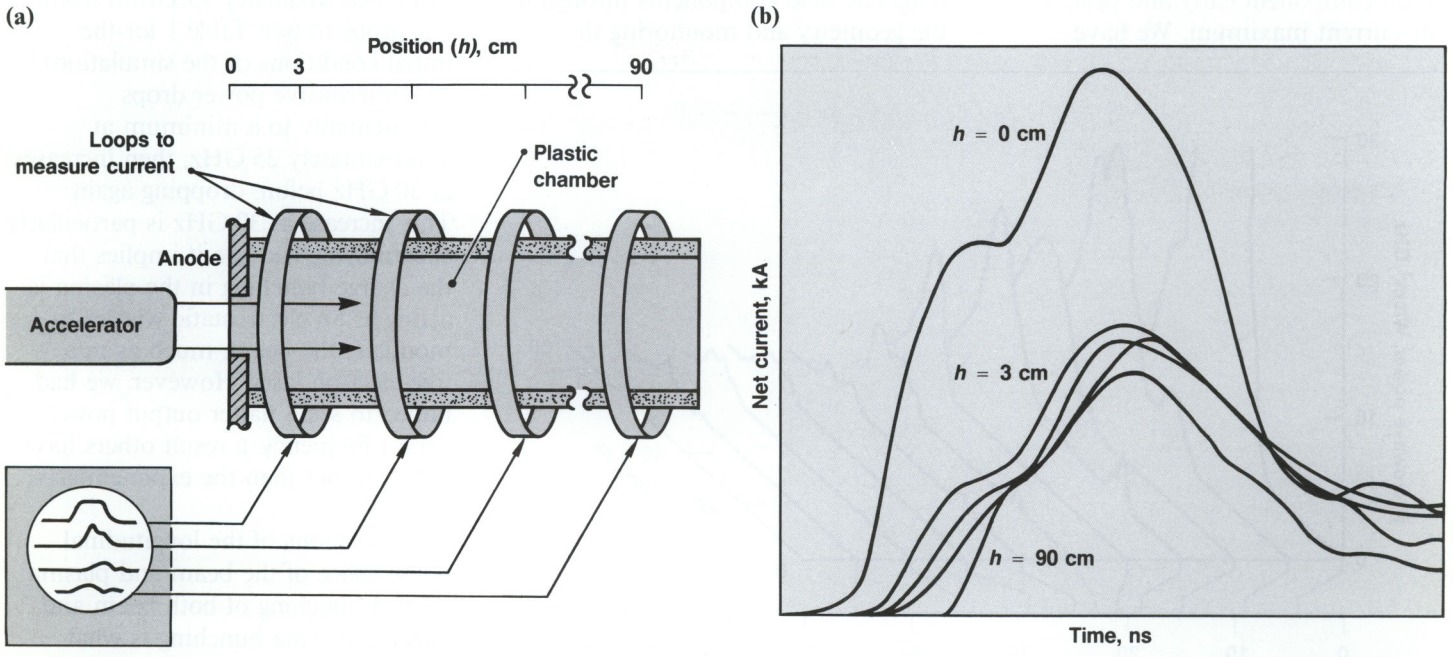

Figure 4. Measurement of beam propagation through plasma. (a) Current-measuring loops placed around the plastic chamber at different positions along the axis. (b) The recorded traces and the injected current ($h = 0$). The plots show a factor-of-two reduction in current and a slight delay in onset of the propagating beam.

channel is plotted as a function of time (diagonal scale). The plot shows that the output power decreases as a function of frequency, in distinct contrast to published results of a constant power with wavelength.

Understanding the beam/plasma interaction requires that we monitor the microwave emission as beam and plasma parameters are varied. Most data were taken with ratios of beam density to plasma density approaching unity, the regime of extreme turbulence.

Figure 6 shows a characteristic plot depicting diode current and microwave emission in two bins, 2 to 6 GHz and 6 to 12 GHz. The key observation is that the low-frequency component, containing the plasma frequency of 3 GHz, occurs early in the pulse and disappears as the beam current rises to its peak value. The second bin is representative of all higher frequencies, which exhibit a small component early and peak at the current maximum. We have hypothesized several explanations for this phenomenon and will test them experimentally by using a more powerful microwave source to make interferometer measurements during electron-beam injection.

Computer Simulations

We performed the computer simulations with the CONDOR code, which contains the complete Maxwell's field equations, as well as many species of charged particles with fully self-consistent equations of motion. The code operates in an axisymmetric mode with r,z geometry to approximate our experimental apparatus. The plasma is simulated with electrons and ions at the desired density, and the beam electrons are injected at the appropriate density and energy. Interaction is monitored by selectively monitoring the electric and magnetic field components throughout the geometry and monitoring the radio-frequency output at the problem boundaries. Fourier transforms of the emitted power give the microwave output as a function of frequency. The parameters for our calculations duplicate those of the experiment as closely as we can make them.

The key results for our simulations are as follows:

- The microwave output power drops exponentially with frequency, with a slight rise in power at γ^2 times the plasma frequency.
- The transverse and longitudinal dimensions of both the beam and plasma show electron bunching, which indicates collective effects.
- The electron beam shows some electrons returning to the emission surface just beyond the point of injection.

As in the experiment, our simulations indicate that there are frequencies emitted at many times the plasma frequency. Figure 7 depicts the simulated frequency spectrum from our problem (see Table 1 for the initial conditions of the simulation). The microwave power drops exponentially to a minimum at approximately 25 GHz, then increases at 30 GHz before dropping again. This increase at 30 GHz is particularly encouraging, because it implies that the charge bunching in the plasma is acting as an electrostatic wiggler to modulate the beam, much as in a free-electron laser. However, we had hoped to see a flatter output power versus frequency, a result others have noted, rather than the exponential decrease.

Simulations of the longitudinal phase space of the beam and plasma show a bunching of both beam and plasma. Plasma bunching is what causes the electrostatic potential needed to modulate the electron beam.

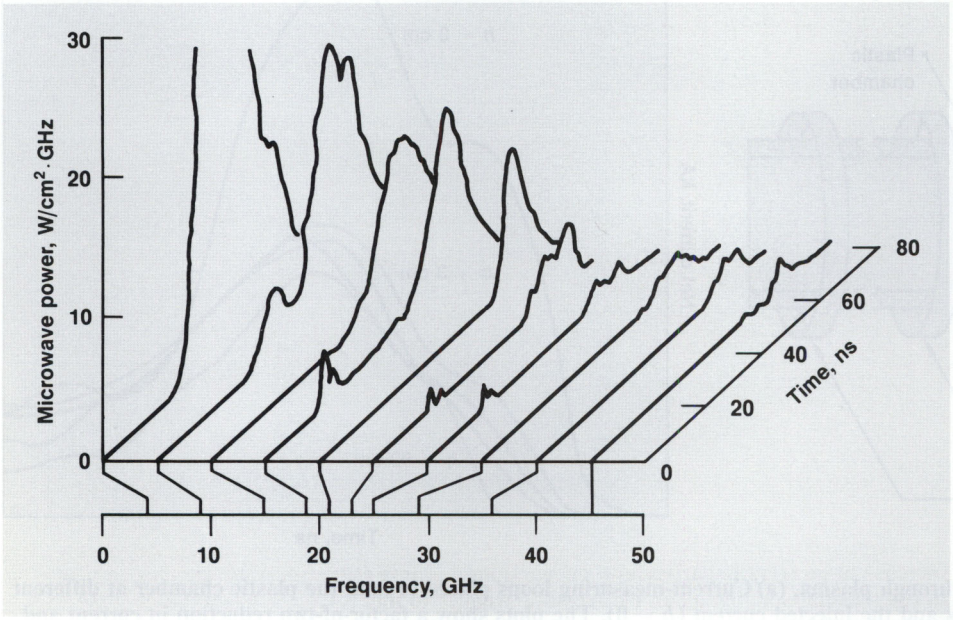

Figure 5. Microwave output power measured in 10 discrete frequency bins, ranging from 2 to 50 GHz. Note the nonlinear decrease in power as frequency is increased.

Future Work

The microwave output measured to date is considerably below that observed by the UC, Irvine, group and lower than our calculations had predicted. We will try to increase the output by several techniques. Our first approach will be to raise both beam and plasma density to increase the beam/plasma interaction. Also, we will increase the level of ionization of the neutral particles to eliminate any possibility of beam ionization creating higher plasma densities. The higher densities will also raise the value of the plasma frequency, enabling us to observe any plasma shift during the various phases of the beam-current pulse.

Although our beam appears to propagate through the plasma without much loss, damage observed on the chamber walls indicates that electrons are being ejected from the central interaction region. By adding a magnetic field, we can contain more of these electrons and perhaps increase the microwave output. This is particularly important if the beam and plasma densities are increased.

Another method of enhancing microwave emission is by introducing spatial variations into the plasma before the beam is injected. This can be done by using ion acoustic waves in the plasma chamber to separate charges in the plasma. The variation in charge density should modulate the beam and increase the microwave output. Spatial variations can also be formed by using slow-wave structures or by injecting plasma in localized regions with plasma jets.

A final approach is to use an annular beam instead of a uniform emitter. Placing most of the current in an annulus may increase the interaction; electron density will be raised in the smaller volume without

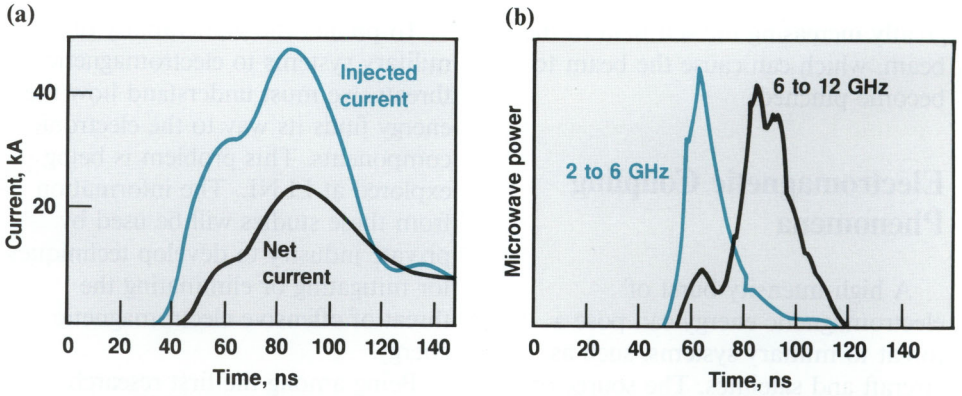

Figure 6. Microwave power relative to injected current. (a) The injected and net currents measured in the device. (b) The lowest frequency microwave bin (2 to 6 GHz) and the 6-to-12-GHz bin, which is characteristic of all the higher bins. The low-frequency output is maximal at the shoulder of the current curve, while the higher frequencies reach a maximum at the peak of the current pulse. This separation in time may indicate that two different mechanisms are operating.

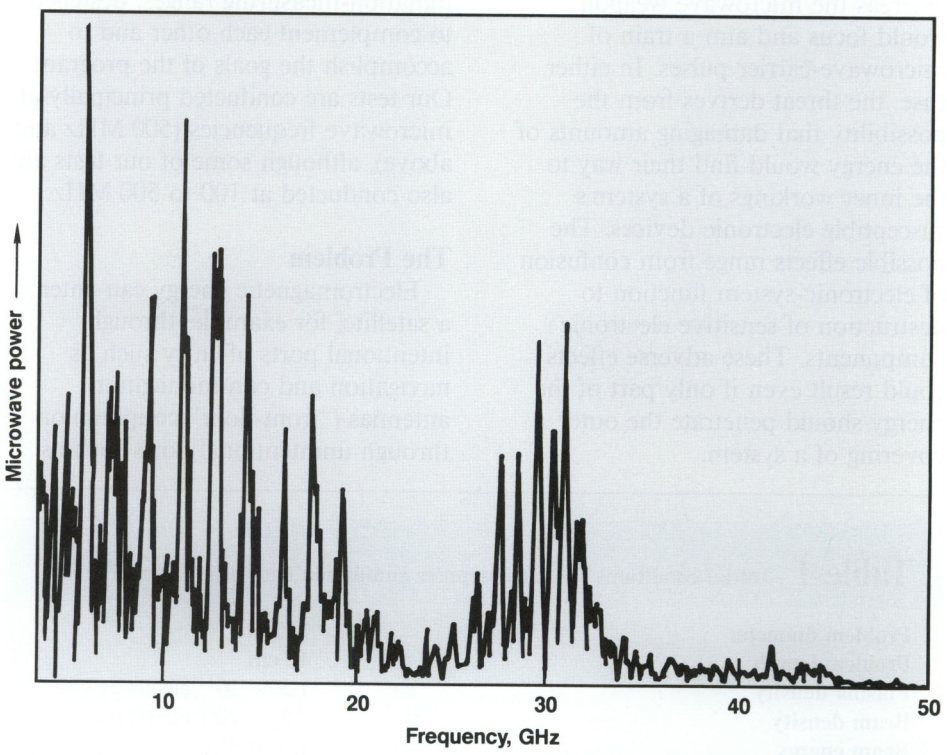

Figure 7. Microwave power as a function of frequency. Our simulations provide the frequency spectrum of the microwave emission. The microwave power drops nonlinearly to a minimum at approximately 25 GHz, then increases at 30 GHz before dropping again. This increase at 35 GHz is particularly encouraging because it implies that the charge bunching in the plasma is acting as an electrostatic wiggler to modulate the beam, much as in the free-electron laser.

greatly increasing the self field of the beam, which can cause the beam to become pinched.

Electromagnetic Coupling Phenomena

A high-intensity burst of electromagnetic energy can pose a threat to military systems, such as aircraft and satellites. The source of the high-intensity, high-frequency pulse can be either a nuclear detonation or a microwave-generating weapon. The nuclear detonation would broadcast a single, omni-directional burst of electro-magnetic energy (a monopulse), whereas the microwave weapon would focus and aim a train of microwave-carrier pulses. In either case, the threat derives from the possibility that damaging amounts of the energy would find their way to the inner workings of a system's susceptible electronic devices. The possible effects range from confusion of electronic-system function to destruction of sensitive electronic components. These adverse effects could result even if only part of the energy should penetrate the outer covering of a system.

To predict the vulnerability of military systems to electromagnetic threats, we must understand how the energy finds its way to the electronic components. This problem is being explored at LLNL. The information from these studies will be used by private industry to develop techniques for mitigating or eliminating the threat of offensive electromagnetic energy.

Being among the first research institutions to attack this problem, we have had to devise new study methods and facilities. We are developing numerical modeling codes and experiments, which will mutually validate our results. We have constructed a pair of enclosed radiation-measuring ranges, designed to complement each other and to accomplish the goals of the program. Our tests are conducted principally at microwave frequencies (500 MHz and above), although some of our tests are also conducted at 100 to 500 MHz.

The Problem

Electromagnetic energy can enter a satellite, for example, through intentional ports of entry such as navigation and communication antennas ("front-door" coupling) or through unintentional ports such as cracks and seams ("back-door" coupling). The energy entering through back-door ports couples to internal wires and cables leading to susceptible electronic components. The issues surrounding back-door coupling are subtle and complex; the difficulty in studying this process is compounded by the presence of an often unquantifiable maze of interconnected cavities, cables, wires, electronics boxes, and other items.

Our electromagnetic-coupling regimes of interest span a wide range of frequencies (and pulse characteristics):

- Nuclear electromagnetic pulses (EMPs), to several hundred megahertz (high-intensity, high-frequency monopulse field).
- Nuclear high-altitude electromagnetic pulses (HEMPs), to approximately 1 GHz (high-intensity, very-high-frequency monopulse field).
- Coherent-microwave pulses, from 0.5 to >40 GHz (extremely high-frequency carrier-pulse field).

The HEMP and microwave regimes act somewhat differently than do the lower frequency EMPs because the HEMP and microwave wavelengths are usually comparable to the size of the ports. Consequently, the ports and the interior configuration of a vulnerable system are no longer below the cutoff frequency and can, therefore, permit significant penetration of the high-frequency energy. In fact, these coupling paths can be highly resonant at certain high frequencies, which concentrates the energy and makes it more difficult to shield against electromagnetic threats. As a confusing and confounding matter of fact, at the higher frequencies, the coupling can also be diminished

Table 1 Initial conditions for the computer simulation shown in Figure 7.

Problem diameter	15 cm
Problem length	40 cm
Plasma density	1.5×10^{11} electrons/cm^3
Beam density	7.5×10^{10} electrons/cm^3
Beam energy	1.0 MeV

because the dimensions of the coupled cavities and internal wires and cables can become tens or even hundreds of wavelengths long.

The Approach

We use a basic building-block approach in tackling these issues. We build a progression of simple, generic test objects of increasing complexity, testing each configuration as we proceed. The tests are made in our electromagnetic radiation laboratories: the EMPEROR and anechoic chamber facilities. The test object is immersed in an electromagnetic field, and the energy level is measured at various interior points for various frequencies and directions of the impinging field.

The procedure starts with simple, generic test objects—such as a plane, cylinder, or box—having simple slot and seam ports. Increasing the complexity, we add first one and then several wires behind the port, followed by metal "fill and clutter" (i.e., objects of random size, shape, and distribution). The next step is to study a test object whose interior is compartmentalized into multiple interconnected cavities. Branched bundles of cables, interior fill, and multiple ports are then added within and between the cavities.

We also test scale models of entire aircraft. The use of scale models can often reveal electromagnetic coupling phenomena that would be difficult or impossible to extract from generic models alone.

In most of our tests, we are able to use coherent continuous-wave electromagnetic fields instead of monopulse energy because our radio-frequency instrumentation systems are very advanced. The instrumentation is highly sensitive, accurate, and flexible, and it has a wide dynamic range and a powerful capability for acquiring and processing data. We prefer testing with coherent continuous waves, of course, because they are easier and cheaper to generate than fast, high-energy monopulses.

With our advanced instrumentation system, we are able to synthesize the conditions and effects of a monopulse field with the data available from the continuous-wave field. Since both the amplitude and phase of the coupled continuous-wave signals are measured over extremely broad bandwidths, the transient response for any electromagnetic pulse can be obtained with high fidelity through inverse Fourier transforms.

We are also using numerical codes to study the phenomena. The codes and experiments serve to validate each other. Like the experiments, the codes are being developed in a basic building-block fashion. Our goal is to develop a three-dimensional, electromagnetic, finite-difference code that can be used to model very large generic and, we hope, complex real systems.

As a result of these studies, we are beginning to understand the basic phenomena of back-door coupling. We are finding that knowledge of only a few topological features is generally sufficient to identify the parameters of the total coupling response. For example, we have found that the dimensions of the port and the length of the wires or cables are very important parameters.

Experimental Facilities

Our experimental studies take place in the EMPEROR and anechoic chamber facilities. Although they have different, complementary operating characteristics, their basic functions are the same. Each facility creates a well-characterized field of electromagnetic energy. All surfaces within the chambers, except the test objects themselves, are designed to be nonreflective and thus to simulate the conditions of unobstructed open space. Both the EMPEROR and anechoic chamber facilities are equipped with state-of-the-art instrumentation systems for automated calibration and data acquisition, processing, and display.

The distinctive features of the two electromagnetic facilities are the following:

- EMPEROR. It has two distinctive features: a wide frequency range (0.1 to 18 GHz) and a well-characterized, highly predictable field. These features allow the EMPEROR facility to be used for calibrating the sensors that measure electromagnetic amplitude and phase.
- Anechoic chamber. Flexibility is its distinguishing feature. It is used for testing large, well-hardened test objects (i.e., those relatively impervious to electromagnetic fields). It operates in the frequency range of 1 to 18 GHz and is equipped with a positioner for mapping radiation patterns.

The EMPEROR facility has a 3-m-high inverted-monocone antenna suspended from the ceiling above an 8.5 × 8.5-m ground plane. Shrouds of microwave-absorbing pyramids are used to mitigate diffraction from the top perimeter of the cone and to minimize reflections from the ceiling and walls. Small test objects (<1.5 m) are usually placed on the ground plane and exposed to a spherically

expanding electromagnetic wave radiated from the monocone apex.

Through analysis and experiment, we found that the characteristics of the radiated field in the test volume are independent of frequency over the entire 0.1- to 18-GHz range; the characteristics are also sufficiently uniform that EMPEROR can serve as a standard in both amplitude and phase. This is important since, above approximately 4 GHz, sensing probes cannot be calibrated in their usual way (by theoretical derivations from their physical dimensions). When a sensing probe is placed in the EMPEROR field, the inverse of its response simply becomes its complex calibration factor.

The anechoic chamber is a recent addition. Early in 1987, a suite of 200-W traveling-wave-tube amplifiers was added; it provides a thousandfold (30 dB) increase in radiated power. Plans ultimately call for a 2-GW vircator microwave-pulse source that will increase the power capability another ten millionfold (70 dB). The latter will permit studies of nonlinear coupling effects, such as electrical breakdown of ports at atmospheric pressures.

Scale-Model Testing

We test scale models of actual vehicles with the hope of gaining knowledge of those electromagnetic coupling effects that might otherwise go undetected in our generic-object testing program. Although the models are visual replicas of real systems rather than exact electromagnetic replicas, many specific electromagnetic coupling effects can be observed.

Figure 8 shows received patterns for coupling of a 2-GHz field into two wires of different lengths (15 and 30 cm) located inside a scale model of the F-14 aircraft, which has many ports. At a scale of 10:1, this response typifies that of a real F-14 at 200 MHz. Note the mean difference in signal level for the 30-cm-long wire compared with the 15-cm-long wire. This decline is typical of electrically long wires, as simple linear theory for wire antennas predicts.

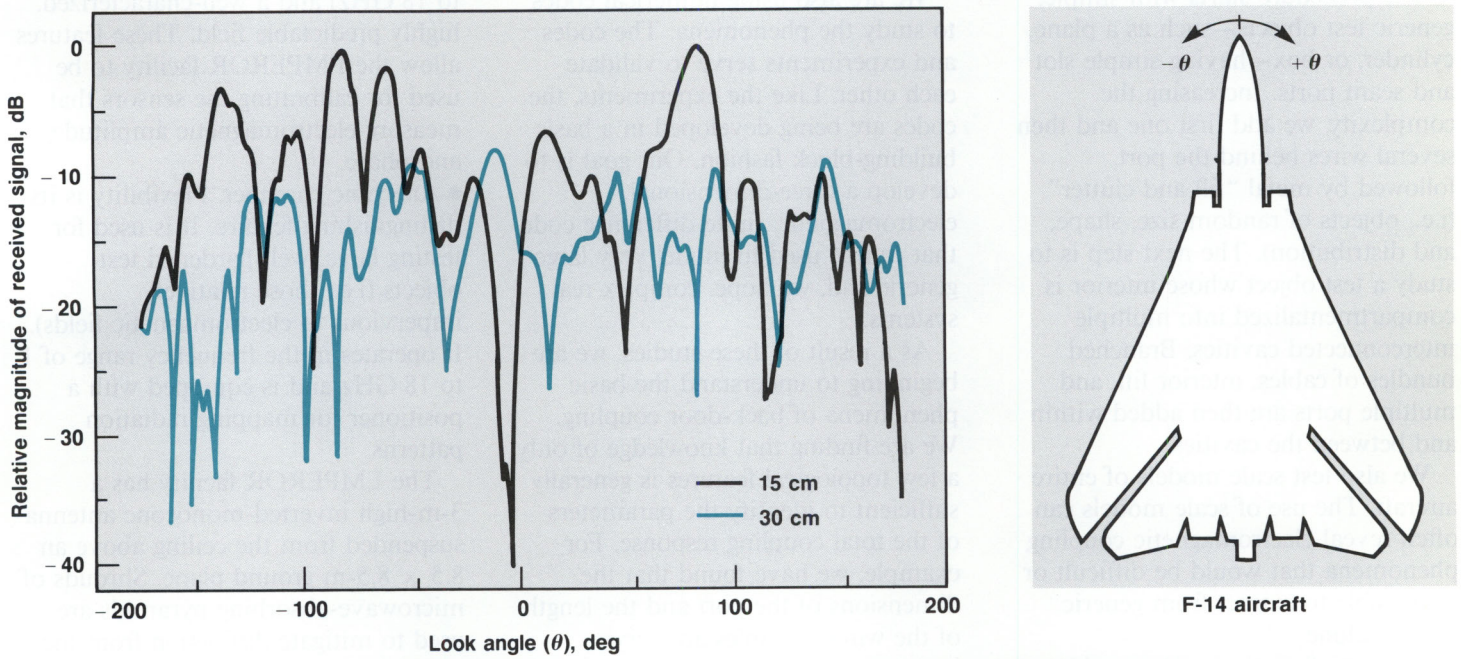

Figure 8. Received patterns for coupling of a 2-GHz field into two wires of different lengths inside a 10:1 scale model of the F-14 aircraft. At the given scale factor and frequency, the response typifies that of a full-scale F-14 at 200 MHz. The mean signal level for the 30-cm-long wire is shown here to be less than for the 15-cm-long wire. This inverse relationship of received-signal-strength to coupling-wire-length is typical of electrically long wires and is explained by simple linear-wire antenna theory.

Summary

Several Laboratory programs will benefit from the efforts we are now making to develop the technologies of high-power microwaves and pulsed power. We are improving our capability to generate and diagnose high-power microwaves and electron beams, to switch pulsed power at much higher power domains than before, and to improve the performance of high-voltage dielectrics. With our EMPEROR and anechoic chamber facilities and our vircator microwave source, we are also investigating the effects of electromagnetic pulses on vulnerable electronics systems.

Key Words: anechoic chamber; beam/plasma interactions; electromagnetic coupling—back door, front door; electromagnetic pulses; EMPEROR; high-altitude electromagnetic pulses; microwaves; pulse power; virtual-cathode oscillator (vircator).

Notes and References

1. D. Sullivan, "Application of the Virtual Cathode in Relativistic Electron Beams," *Proceedings of the Third International Conference on High Power Electron and Ion Beam Research and Technology, Novosibirsk, Soviet Union, July 3-6, 1979*, vol. 2, p. 769.
2. K. G. Kato, G. Benford, and D. Tzach, "Detailed Spectra of High-Power Broadband Microwave Radiation from Interactions of Relativistic Electron Beams with Weakly Magnetized Plasmas," *Phys. Flds.* **26** (12), 3636–3649 (1983).
3. A basic characteristic of the plasma electrons is the plasma frequency, which arises from the long-range forces between plasma electrons and causes the plasma to act as a system of coupled oscillators.

Remote Sensing, Imaging, and Signal Engineering

Our new methods for extracting useful information from noisy or distorted signals have a wide variety of energy and defense applications.

For further information contact Gregory A. Clark (415) 423-4268 or Rowland R. Johnson (415) 423-3064.

We are engaged in work on a wide variety of projects in signal processing, image processing, remote sensing, artificial intelligence (knowledge engineering or expert systems), and systems research. Programs that have already benefited from this research include those concerned with nuclear event diagnostics, nondestructive testing, synthetic aperture radar, coded aperture imaging, line-of-sight alignment problems, and imagery analysis.

We are also using array signal processing and knowledge-based signal processing to improve the performance of seismic treaty-verification systems and nondestructive testing systems. Array signal processing is a way of exploiting multiple sensors to extract more information from acoustic or electromagnetic signals. Knowledge-based signal processing uses artificial intelligence to sift vast quantities of data rapidly and automatically for the one or two features that may be significant.

Treaty Verification

The most reliable means currently available to verify compliance with treaties regulating underground nuclear testing is seismic monitoring. Existing teleseismic monitoring methods (those using only stations at great distances, i.e., outside the Soviet Union) would be inadequate for verifying a Comprehensive Test Ban Treaty (CTBT); it is possible to muffle a small nuclear detonation so that its seismic signals are undetectable at teleseismic distances. If a CTBT were ratified, there would have to be a network of seismic monitoring stations near and within the Soviet Union sensitive enough to detect intentionally muffled signals in spite of background noise.

Such a regional network would detect perhaps 40 000 earthquakes and chemical explosions per year, each of which would have to be scrutinized to determine if it were a clandestine nuclear test. There are nowhere near enough trained seismologists to do the job, so reliable CTBT verification will require an automated system for interpreting and classifying seismic events.

We have developed such an automated system that mimics the way experienced seismologists work. It takes time and skill to deduce, often from very tenuous clues, where a seismic event happened and what may have caused it. We are codifying how seismologists represent seismic events and reason about them so that the expert system can rapidly sift out the earthquakes and chemical explosions, and refer only the borderline cases (the possible treaty violations) to the expert seismologists.

We derived the expertise of the system through observation and through interviews with a seismologist using the Norwegian Seismic Array (NORSAR). NORSAR consists of an array of seismometers spread over about six square kilometres. It takes sophisticated signal processing to bring out the full advantages of the array, using both general seismological expertise and NORSAR-specific expertise (see the box on p. 47).

Figure 1 shows the process that a seismologist (or an expert system) uses in analyzing a seismic event. Initially, the system (or seismologist) applies a core set of signal processing routines to the seismogram and formulates initial ideas about what it shows. These ideas form the basis for additional signal processing to produce more information either to confirm or to reject the first ideas. This cycle continues until the hypotheses have been extended into a consistent interpretation of the event.

Earthquakes and Seismometers

When most people think of a seismometer, they see a pen tracing a straight line on a graph and then, during an earth movement, swinging violently from side to side. This actually happens during a strong earthquake, but such occasions are fortunately rare. The most common earthquakes by far are insignificant tremors that only sensitive instruments can detect.

When we make instruments sensitive enough to pick up the rumblings of a distant earthquake, they also pick up all sorts of extraneous information, or noise. They begin to register surf booming on the shore, trucks moving down the road, and even nearby footsteps. The seismologist's problem is to find the real earthquake (or nuclear test) among all this noise.

One way to find the real data is to identify the noise sources and filter them out. Surf or footsteps are not just noise; they have distinctive sounds and characteristic patterns. By studying these characteristics, we can design electronic filters that discard much of this unwanted information and make it easier to spot significant events.

Another way is to make the seismometer directional, since an earthquake happens in a particular place, and noise comes from all directions. If we know where to expect the earth tremor to start, as in a known nuclear testing area, we can then aim the seismometer and ignore the noise coming from other directions.

The usual way to make a directional measurement is to use several seismometers spread out over an area of a few square kilometres. Signals take time to travel through the earth, so they will arrive at the different seismometers at different times (depending on the direction of travel). By allowing for the different time delays that correspond to the selected direction, we can enhance signals coming from that direction and suppress those from other directions.

In general, however, and especially when we are trying to detect a clandestine test, the seismic event could be anywhere within a very large area, and the signals could be coming from various directions. Therefore, we must scan the many possible directions. Since we cannot move the array, we search multiple directions by recording the signals from each detector and then recombining them with different sets of delays (corresponding to the different directions) to search for the direction that yields a significant event.

In addition to facts about seismic events that enable it to make preliminary interpretations, the system needs rules of inference (IF condition THEN action) that specify how to proceed to extend the interpretation. The condition sets out the premises that justify a particular action; the action specifies any necessary computations to yield a new inference. The system then tests this new inference against everything established up to that point to determine whether to accept or reject it.

Beam forming, for example, which can be used to compute the velocity and direction of various kinds of seismic waves, produces its best results when we know the type of wave. (Any seismic event produces several kinds of waves, or phases, which travel at different velocities.) Thus, to paraphrase one such rule, if we know a phase to be P_j, then we can compute its direction and velocity.

To carry the example one step further, suppose we apply beam forming to a particular case and compute a velocity of 5.5 km/s. This invalidates the assumption that the phase is P_n, because we know that all P_n phases go faster than 6 km/s. Our expert system incorporates assumption-based logic to spot such contradictions and mark all inferences derived from false assumptions as false.

We use three classes of signal processing routines: phase detection, measurements, and signal transformation. Measurement involves determining the variance, dominant frequency, or number of zero crossings of a phase. Signal transformations operate on one or more signals (e.g., filtering to reject unwanted frequencies or adjusting time delays) to produce a signal with enhanced characteristics. It is hard to quantify just how a seismologist detects phases; computer methods tend to see too many phases or not enough.

Figure 2 shows some of the steps in analyzing a typical seismogram. The initial phase detection finds a feature near the end of the seismogram that could be either a P_n phase or an L_g phase. Working on the P_n interpretation, the system computes the frequency components of the phase (the fast Fourier transform, or FFT)

and determines it to be consistent, but the inferred velocity is too low (less than 6 km/s). This contradiction invalidates the original partial interpretation and stops work on it.

Work continues on the L_g partial interpretation. Its computed FFT turns out to be consistent, so the system uses the FFT results, assuming that it is an L_g phase, to estimate the distance to the source and from this to infer more or less where to look on the seismogram for the P_n phase. Assuming that the feature found there is the P_n phase, the system uses the interval between the beginning times of the P_n and L_g phases to form an exact estimate of the distance. Finally, it checks whether the directions of the two phases agree and, if they do, reports its analysis of the event.

It is clear that no such automated system can take on the full responsibility for treaty verification; its analyses must be subject to review. To this end, not only does our system describe the inferences it makes and the reasons for them, it also lets the seismologist tentatively overrule one or more decisions to see whether more believable measurements are produced. The seismologist can also choose to ignore an apparent contradiction found by the system and continue work on a terminated partial interpretation.

Our next step will be to extend the system to include other seismic monitoring stations, each with a new rule set tailored to its own sensors and local geology. This will enable the expert system to support the kind of collaborative analysis seismologists now do when more than one station observes the same event.

Nondestructive Evaluation

One way to detect and characterize hidden flaws in welds, castings, and laminated materials without ruining them is to send ultrasound pulses through them and measure the resulting echoes. This sounds simple, but it is often hard to interpret the measured signals because they are distorted by wave propagation effects, process and instrument noise, and the transducer (the device that converts an electrical pulse into an acoustic pulse, and then converts the echo back into an electrical signal). We are developing ways to counteract or compensate for these distortions to make it easier to interpret the signals, and thereby make ultrasonic inspection more useful.

The signals we are most interested in are those scattered from cracks, voids, inclusions, and imperfect bonds between layers of materials. Layered materials are especially important in nondestructive evaluation because we encounter them so often (for more information on nondestructive evaluation, see the article beginning on p. 11). Butt welds, pinch welds, electronic solid-state devices, diffusion bonds, and light-weight graphite-epoxy composite materials can all be viewed as layered structures.

In a typical layer problem, we need to measure layer thicknesses and detect places where layers failed to bond. To do this we mount an ultrasonic transducer on an acoustic microscope and send broadband ultrasound pulses through the material. For each position of the transducer, measuring the pulse echoes produces a time waveform (an A scan of the part) containing information about scattering and material properties.[1-3] If we move the transducer along a line, we collect a family of A scans that we can combine into a two-dimensional image (a B scan). In layer problems, our main goal is to resolve the signals that indicate layer boundaries.

Decoding such signals is a fundamental inverse problem known

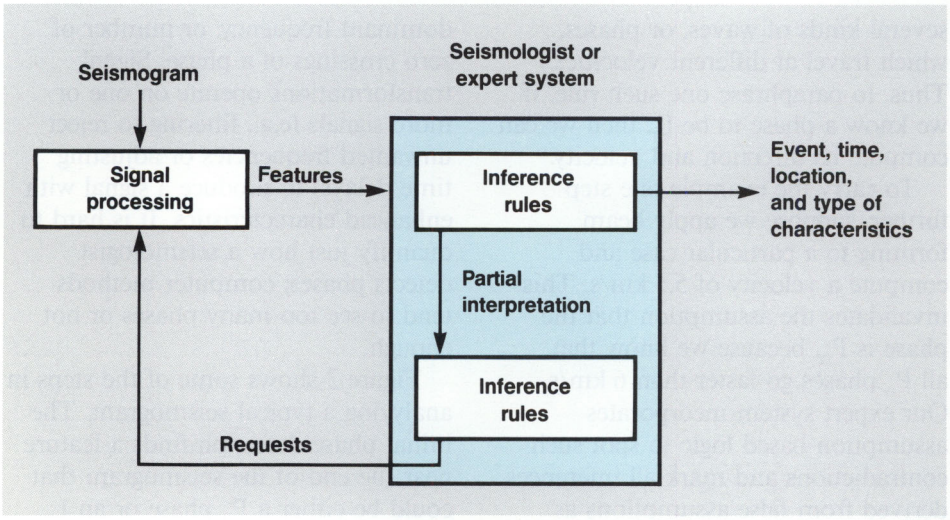

Figure 1. The general strategy used, by seismologists and expert systems alike, to interpret seismograms. Both apply signal processing routines to the raw seismograms to pick out seismic features that may or may not be significant. Inference rules suggest a partial interpretation of the feature, which is tested according to more inference rules by more signal processing, and so on until a consistent interpretation emerges.

as system identification, deconvolution, or signal restoration.[1-7] Ultimately, we wish to estimate the thickness of each layer and the value of the reflection coefficient at each interface. We have achieved significant success in using nonparametric system identification methods[1-3] to estimate the impulse responses of layered materials and from this the reflection coefficients and layer thicknesses. We are now concentrating on an advanced technique called model-based parameter estimation.[2,7]

If we excite a specimen made of layers of various materials with a sound field normal to its surface, we will detect a series of echoes whose strengths and delays with respect to the original impulse depend on the reflection coefficients of the different boundaries and the thicknesses of the different layers (Figure 3). We can create from wave theory a set of recursive equations that represent this model in state-space form. The model-based parameter estimation technique folds this wave-propagation model into the processing algorithm

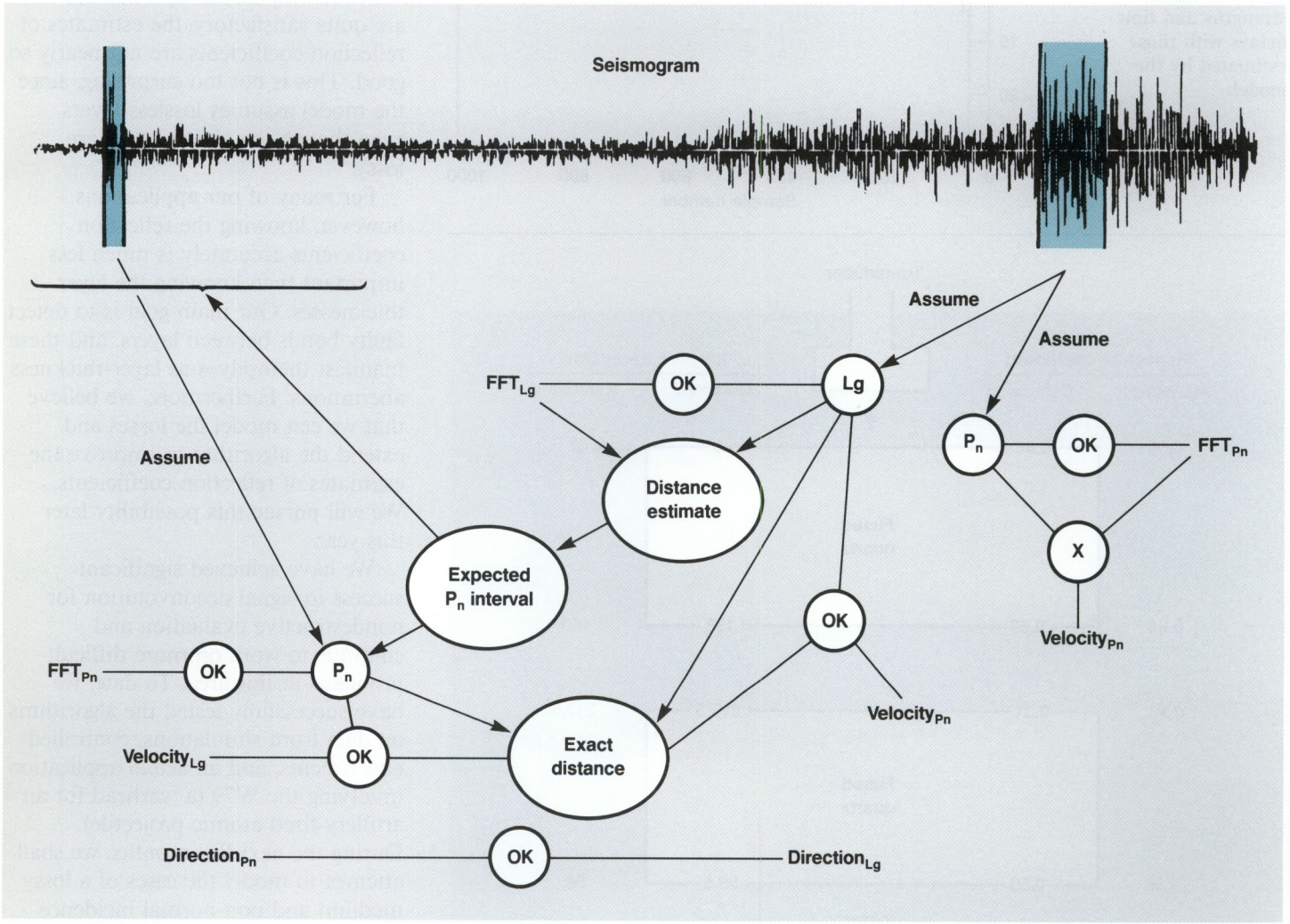

Figure 2. Analysis of a typical seismogram by our expert system. The system tests a feature that may be either a P_n or an L_g phase by calculating the fast Fourier transform and the velocity, and determines that the feature cannot be P_n. A distance estimate based on the L_g assumption enables the system to find another feature that turns out to be the P_n phase, which in turn helps the system refine its distance estimate and produce a consistent interpretation.

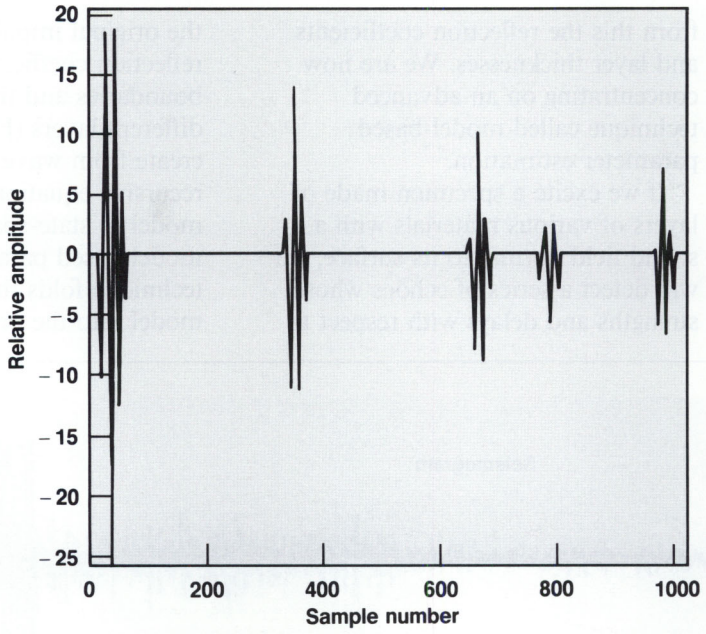

Figure 3. An echo waveform received in a controlled experiment in which we excited a specimen consisting of alternate layers of fused quartz and water with a single ultrasonic pulse. Since we know the composition and thicknesses of the layers, we can compare the signal strengths and time delays with those estimated by the model.

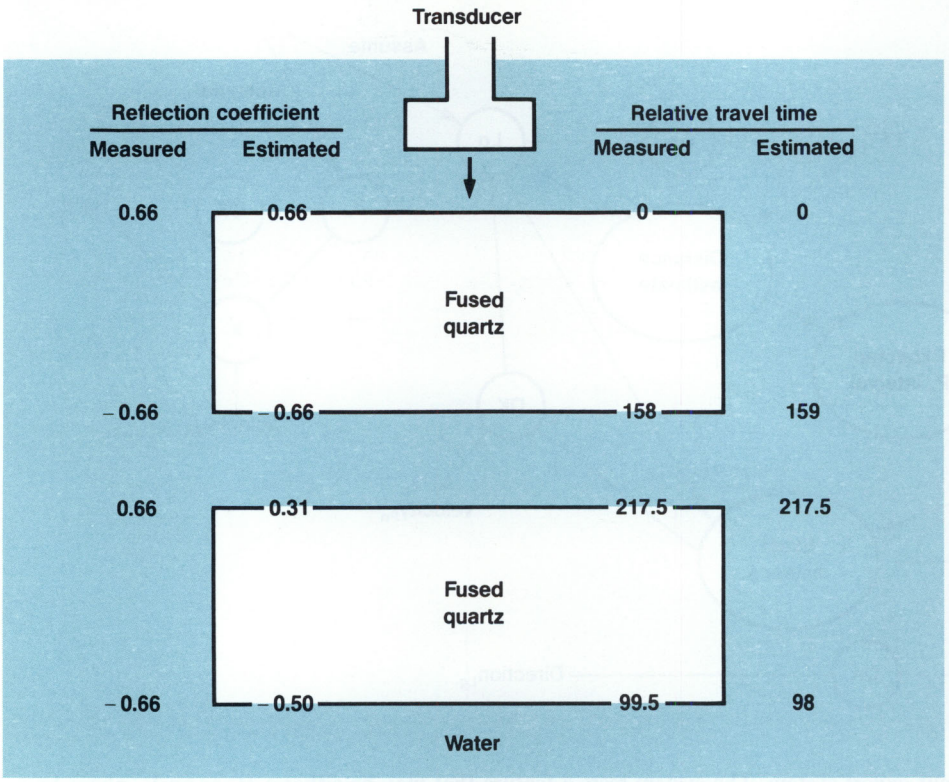

Figure 4. Diagram of our experimental setup for testing estimates of the reflection coefficient and signal travel time. Here, two layers of fused quartz, immersed in water, provide four material discontinuities or interfaces from which a signal sent by a transducer is reflected. The measured and estimated reflection coefficients for each interface are shown. We also show the measured and estimated relative times it takes for the signal to travel through each layer, i.e., from a given interface to the one immediately below it. Note that the times are not cumulative and refer in each case to only one layer.

and recursively estimates the reflection coefficients and layer thicknesses one at a time until a deteriorating signal-to-noise ratio forbids any further recursions.[1,2]

Figure 4 shows the results of applying this method to alternating layers of fused quartz and water. Although the estimates of the time it would take the signal to travel through each layer (the time being dependent upon the layer's thickness) are quite satisfactory, the estimates of reflection coefficients are not nearly so good. This is not too surprising, since the model assumes lossless layers even though the actual layers are lossy.

For many of our applications, however, knowing the reflection coefficients accurately is much less important than knowing the layer thicknesses. Our main goal is to detect faulty bonds between layers, and these manifest themselves as layer-thickness aberrations. Furthermore, we believe that we can model the losses and extend the algorithm to improve the estimates of reflection coefficients. We will pursue this possibility later this year.

We have achieved significant success in signal deconvolution for nondestructive evaluation and continue to work on more difficult problems in this area. To date, we have successfully tested the algorithms on data from simulations, controlled experiments, and an actual application involving the W79 (a warhead for an artillery-fired atomic projectile). During the next few months, we shall attempt to model the cases of a lossy medium and non-normal incidence and fold these models into the parameter-estimation algorithms. We also plan to experiment with more difficult materials used in other Laboratory programs.

Line-of-Sight Alignment

Our large lasers, accelerator chambers, and advanced diagnostic imaging systems work properly only when all their parts are accurately aligned. The conventional way to do this is to sight through the equipment with a surveying transit and adjust the supports until the centers of cross-hair reticles at the two ends appear to coincide (Figure 5). Although this technique works fairly well with human observers, we find that more sophisticated reticles based on two-dimensional signals with large space-bandwidth products work better with the digital image processing used for alignment control and analysis.

One possible coded reticle is the circularly symmetric Fresnel pattern (Figure 6a), which behaves like a thin lens focusing incident plane waves to a distant point. In the Stanford Linear Accelerator, for example, a collimated laser beam illuminates a Fresnel lens at one end of the chamber, producing a bright spot in the focal plane at the opposite end that indicates the center position of the system.

The Fresnel lens is a special case of a more general alignment system consisting of two coded apertures that are optically superimposed like cross-hair reticles (Figure 6b). Instead of the camera or focal plane array required with cross hairs, this system uses a simple correlation operation performed by an inexpensive integrating lens and a detector. The output signal intensity is maximal when the two reticles are aligned, a two-dimensional analog to radar-pulse encoding and matched filtering.

The only way to increase the resolution of a set of cross hairs is to

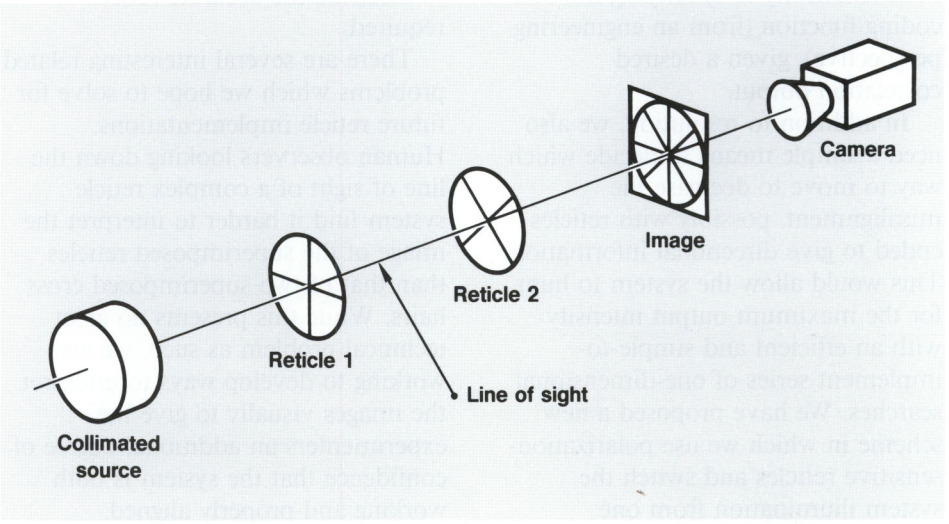

Figure 5. A conventional alignment setup with cross hairs. The collimated light source (often a laser) projects images of the two reticles on an image plane where they are observed with either a camera or a telescope. The only way to increase the resolution of this system is to make the cross hairs of finer filaments, which makes them harder to see.

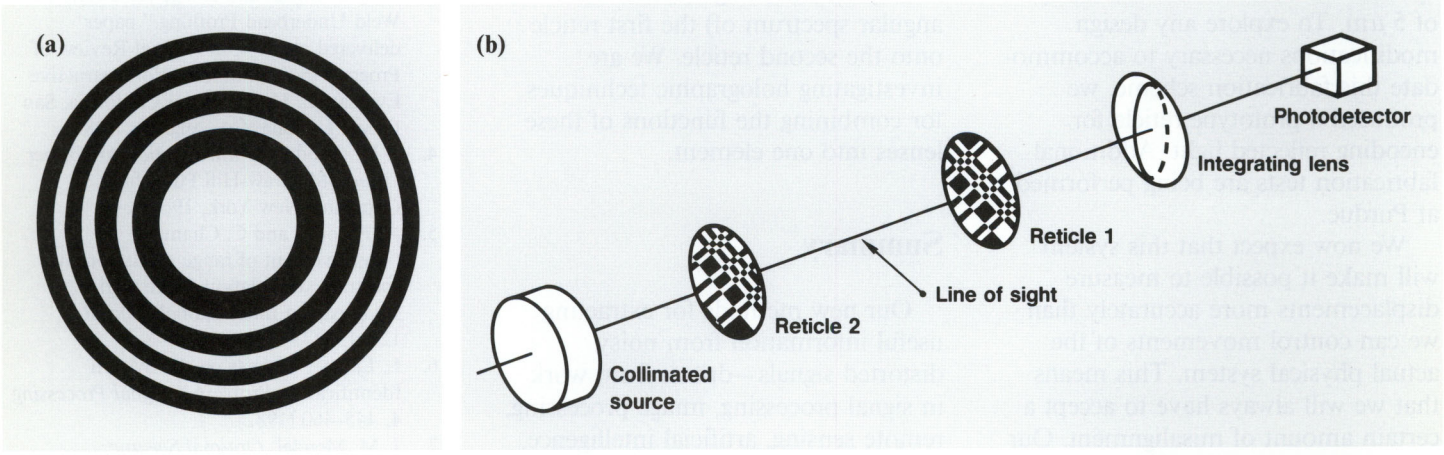

Figure 6. Two reticle systems used to align a collimated light beam. (a) A Fresnel zone-plate reticle that acts as a thin lens, focusing collimated laser light to a fine point that indicates the center of the system. This enables an unattended centering system to maintain alignment automatically. (b) An alignment setup with a pair of coded reticles whose net transmission is maximal when they are aligned. Such reticles can be designed to simplify the process of searching for optimal alignment so that it can be conducted by automatic machinery.

make the hairs finer, which makes them harder to see. In technical parlance, we have "sacrificed signal-to-noise-ratio performance." We have investigated various direct and iterative design techniques for producing reticles whose signal-to-noise performance is independent of their resolution. This corresponds mathematically to specifying the best coding function (from an engineering perspective), given a desired correlation output.

In addition to resolution, we also need a simple means to decide which way to move to decrease the misalignment, possibly with reticles coded to give directional information. This would allow the system to hunt for the maximum output intensity with an efficient and simple-to-implement series of one-dimensional searches. We have proposed a new scheme in which we use polarization-sensitive reticles and switch the system illumination from one polarization to another.

In collaboration with Neal Gallagher of Purdue University, we have begun fabrication of 1-cm-square test reticles using an electron-beam system with a resolution capability of 5 μm. To explore any design modifications necessary to accommodate this fabrication scheme, we produced a prototype reticle for encoding reflected light. Additional fabrication tests are being performed at Purdue.

We now expect that this system will make it possible to measure displacements more accurately than we can control movements of the actual physical system. This means that we will always have to accept a certain amount of misalignment. Our next step will be to investigate methods for assessing the final quality of alignment.

In summary, we have developed coded reticles with large space-bandwidth products that produce sharp correlation outputs, and polarization-sensitive reticles that decompose the problem into two simpler one-dimensional problems. We are exploring the use of electron-beam hardware that makes it possible to fabricate the accurate reticles required.

There are several interesting related problems which we hope to solve for future reticle implementations. Human observers looking down the line of sight of a complex reticle system find it harder to interpret the image of the superimposed reticles than that of two superimposed cross hairs. While this presents no great technical problem as such, we are working to develop ways to interpret the images visually to give the experimenters an additional degree of confidence that the system is both working and properly aligned.

We are also designing reticles to sense and correct relative rotation errors in the alignment produced by warping in the chamber. Just as with the cross-hair system, this calls for a lens system to image (collect the angular spectrum of) the first reticle onto the second reticle. We are investigating holographic techniques for combining the functions of these lenses into one element.

Summary

Our new methods for extracting useful information from noisy, distorted signals—drawn from work in signal processing, image processing, remote sensing, artificial intelligence, and systems research—have a wide variety of energy and defense applications. This research has already benefited Laboratory programs concerned with nuclear event diagnostics, nondestructive testing, synthetic aperture radar, coded aperture imaging, and line-of-sight alignment problems. We are also using array signal processing and knowledge-based signal processing to improve the performance of systems for the interpretation of seismic signals in treaty verification. Our work on coded apertures has significantly increased our fundamental understanding of the basic physics and engineering requirements of alignment systems.

Key Words: alignment systems; artificial intelligence; coded reticles; layered structures; nondestructive evaluation; nondestructive inspection; treaty verification.

Notes and References

1. G. A. Clark, D. M. Tilly, and B. D. Cook, "Ultrasonic Signal/Image Restoration for Quantitative NDE," *NDE International*, **19** (3), 160–176 (1986).
2. G. A. Clark and F. L. Barnes, "Model-Based Parameter Estimation for Layer Problems QNDE," paper delivered at the 13th Annual Review of Progress in Quantitative Nondestructive Evaluation, University of California, San Diego, La Jolla, CA, Aug. 3-8, 1986.
3. G. A. Clark, F. L. Barnes, and G. Thomas, "Digital Signal and Image Restoration for Weld Underbead Profiling," paper delivered at the 13th Annual Review of Progress in Quantitative Nondestructive Evaluation, University of California, San Diego, La Jolla, CA, Aug. 3-8, 1986.
4. J. W. Goodman, *Introduction to Fourier Optics* (McGraw-Hill Publishing Company, New York, 1968).
5. A. Papoulis and C. Chamzas, "Improvement of range resolution by spectral extrapolation," *Ultrasonic Imaging, An International Journal* **1**, 121–135 (1979).
6. L. Ljung, "Aspects on the System Identification Problem," *Signal Processing* **4**, 445–460 (1982).
7. J. M. Mendel, *Optimal Seismic Deconvolution, an Estimation-Based Approach* (Academic Press, New York, 1983).

Abstracts

Materials Engineering

The Laboratory's expanding technical requirements for a variety of engineering materials make it essential to understand, in a quantitative way, the physical and mechanical behavior of such materials. Laboratory engineers are engaged in an interdisciplinary effort (involving such diverse fields as solid mechanics, thermal sciences, materials testing, measurements engineering, and material science) to better predict and optimize material behavior. Examples of the materials we are now investigating include composite laminates, ultrafine-grained Hadfield steels, and commonly used elastomers.

Contact: Donald R. Lesuer (415) 422-9633, Alfred Goldberg (415) 422-7165, or William W. Feng (415) 422-8701.

Quantitative Nondestructive Evaluation

The capability for inspecting and quantifying the internal features of opaque materials and assemblies without damaging or disassembling them is of great value. The Laboratory continues to improve methods for applying ultrasonic and radiographic technology to the nondestructive evaluation of a variety of materials. We are developing computer algorithms that will help us interpret ultrasonic scans of layered materials and others that will enable the computer to reconstruct three-dimensional x-ray tomographic images more quickly. We are also improving image resolution with a microfocus x-ray tube for use in computed tomographs. Our future work will include pursuing various methods of improving image quality and reducing processing time. We will also continue to try to develop nondestructive evaluation methods for discriminating among chemical elements in a test object.

Contact: Ronald D. Streit (415) 422-7045, Gregory A. Clark (415) 423-4268, or James M. Brase (415) 422-6992.

Modal Analysis: Understanding the Dynamic Characteristics of Structures

At the Laboratory, large pieces of experimental equipment, such as the Nova laser, are supported by structures that must withstand the considerable stresses imposed by physics experiments and, at times, earthquakes. To ensure the stability and integrity of these structures, engineers perform modal analyses to determine their resonant frequencies and other modal parameters. The results of these analyses can indicate any modifications that need to be made in the structure.

Contact: H. Joseph Weaver (415) 422-0310.

Microtechnology for Research Diagnostics

The Diagnostic and Microelectronics Engineering group at LLNL conducts research and development in several microfabrication processes (originally developed in the commercial semiconductor industry) to meet program needs for diagnostic equipment with faster response time or tolerance of high voltages. These processes are microphotolithography, semiconductor chemical and plasma etching, thin-film deposition techniques for certain metals and dielectrics, and ion implantation. Components produced with this technology include high-voltage switches, very-high-speed integrated circuits, and miniature radiation detectors. Our most recent achievements have been in fabrication of free-standing membranes and integrated optical devices.

Contact: Joseph W. Balch (415) 422-8643, Dino R. Ciarlo (415) 422-8872, or Glen M. McWright (415) 423-6768.

High-Power Microwaves and Pulsed Power

The Laboratory has five major research projects on the technology of high-power microwaves and pulsed power. These projects are directed at improving our ability to generate high-power microwaves and high-power electron beams, to extend our pulsed-power switching capability into higher-power domains, to understand and improve the electrical performance of high-voltage dielectrics, and to study electromagnetic coupling phenomena as they relate to the vulnerability of weapons systems. Our research facilities include a well-equipped pulsed-power laboratory, a microwave standard-field range (the EMPEROR facility), a microwave-field pattern-mapping range (which includes an anechoic chamber), and a microwave engineering laboratory. This article treats all five research projects and discusses progress in microwave generation and in the study of electromagnetic coupling phenomena.

Contact: W. Wayne Hofer (415) 422-1636, Scott C. Burkhart (415) 423-2061, Donald J. Meeker (415) 422-5434, Marco S. Di Capua (415) 422-9698, or Ray J. King (415) 423-2369.

Remote Sensing, Imaging, and Signal Engineering

Our new methods for extracting useful information from noisy, distorted, or incomplete signals include techniques from the disciplines of signal processing, image processing, remote sensing, artificial intelligence (knowledge engineering), and systems research. Laboratory programs concerned with nuclear event diagnostics, nondestructive testing, synthetic aperture radar, coded aperture imaging, line-of-sight alignment problems, and medical ultrasound tomography are already applying the results of this research. We are also using array signal processing and knowledge-based signal processing to improve the performance of systems for nondestructive testing and treaty verification based on seismic signals.

Contact: Gregory A. Clark (415) 423-4268 or Rowland R. Johnson (415) 423-3064.

Recent Titles

Articles published in recent issues of Energy and Technology Review are grouped below according to their chief sponsors, the Assistant Secretaries of the U.S. Department of Energy. Research funded by other federal agencies is listed under Work for Others.

ENERGY RESEARCH

The Magnetic Fusion Energy Program (November 1986)
Evolution of the Tandem Mirror Approach to Magnetic Fusion (November 1986)
MFTF-B: The Mirror Fusion Test Facility (November 1986)
Overview of Plant and Capital Equipment Tests (November 1986)
PACE Tests: The Magnet System (November 1986)
PACE Tests: The Cryogenic System (November 1986)
PACE Tests: The Neutral-Beam Power-Supply System (November 1986)
PACE Tests: The Electron-Cyclotron Resonance Heating System (November 1986)
PACE Tests: The Plasma Diagnostics System (November 1986)
PACE Tests: The Integrated Control System (November 1986)

DEFENSE PROGRAMS

Office of Military Application

Materials Engineering (March 1987)
Quantitative Nondestructive Evaluation (March 1987)
Modal Analysis: Understanding the Dynamic Characteristics of Structures (March 1987)
Microtechnology for Research Diagnostics (March 1987)
High-Power Microwaves and Pulsed Power (March 1987)
Remote Sensing, Imaging, and Signal Engineering (March 1987)
Modeling Canonical Problems in Electromagnetic Coupling Through Apertures (October 1986)
Finite-Element Codes for Computing Electrostatic Fields (October 1986)
Iterative Techniques for Solving Boltzmann's Equations for p-Type Semiconductors (October 1986)
Improved Numerical-Solution Techniques in Large-Scale Stress Analysis (October 1986)
Finite-Element Modeling of Electromagnetic Phenomena (October 1986)
Modeling Microwave-Pulse Compression in a Resonant Cavity (October 1986)
Lagrangian Finite-Element Analysis of Penetration Mechanics (October 1986)
Crashworthiness Engineering (October 1986)
Computer Modeling of Metal-Forming Processes (October 1986)
Thermal-Mechanical Modeling of Tungsten Arc Welding (October 1986)
Modeling Air Breakdown Induced by Electromagnetic Fields (October 1986)
Semiconductor Modeling (October 1986)

LABORATORY REVIEWS

The Laboratory and Arms Control (January·February 1987)
On the Road to a More Stable Peace (January·February 1987)
Arms Control Activities at LLNL (January·February 1987)
Safeguarding Our Military Space Systems (January·February 1987)
Arms Control and Future Nuclear Weapons Limits (January·February 1987)
Transition to Deterrence Based on Strategic Defense (January·February 1987)
How to Avoid War with the Soviet Union (January·February 1987)
State of the Laboratory (June·July 1986)

WORK FOR OTHERS

Department of Defense

Experiments with the Free-Electron Laser (December 1986)
Induction Linear Accelerator for the Free-Electron Laser (December 1986)
Optical Systems for the Paladin Experiment (December 1986)
Physics of the Free-Electron Laser (December 1986)
The Laboratory's Free-Electron Laser Program: An Interview (December 1986)
Two Applications for the Free-Electron Laser (December 1986)

U.S. Government Printing Office: 1987/3 – 785-062/48423

Technical Information Department
Lawrence Livermore National Laboratory
University of California
Livermore, California 94550